



저작자표시-비영리-변경금지 2.0 대한민국

이용자는 아래의 조건을 따르는 경우에 한하여 자유롭게

- 이 저작물을 복제, 배포, 전송, 전시, 공연 및 방송할 수 있습니다.

다음과 같은 조건을 따라야 합니다:



저작자표시. 귀하는 원저작자를 표시하여야 합니다.



비영리. 귀하는 이 저작물을 영리 목적으로 이용할 수 없습니다.



변경금지. 귀하는 이 저작물을 개작, 변형 또는 가공할 수 없습니다.

- 귀하는, 이 저작물의 재이용이나 배포의 경우, 이 저작물에 적용된 이용허락조건을 명확하게 나타내어야 합니다.
- 저작권자로부터 별도의 허가를 받으면 이러한 조건들은 적용되지 않습니다.

저작권법에 따른 이용자의 권리는 위의 내용에 의하여 영향을 받지 않습니다.

이것은 [이용허락규약\(Legal Code\)](#)을 이해하기 쉽게 요약한 것입니다.

[Disclaimer](#)

Ph.D. DISSERTATION

Search for New Physics Phenomena in  $ll\gamma$   
Final States in the CMS Experiment

CMS 실험을 통한  $ll\gamma$  최종 상태에서의 새로운 물리 현상  
탐색

BY

남경욱

AUGUST 2020

DEPARTMENT OF PHYSICS AND ASTRONOMY  
COLLEGE OF NATURAL SCIENCE  
SEOUL NATIONAL UNIVERSITY

Ph.D. DISSERTATION

Search for New Physics Phenomena in  $ll\gamma$   
Final States in the CMS Experiment

CMS 실험을 통한  $ll\gamma$  최종 상태에서의 새로운 물리 현상  
탐색

BY

남경욱

AUGUST 2020

DEPARTMENT OF PHYSICS AND ASTRONOMY  
COLLEGE OF NATURAL SCIENCE  
SEOUL NATIONAL UNIVERSITY

Search for New Physics Phenomena in  $ll\gamma$  Final  
States in the CMS Experiment

CMS 실험을 통한  $ll\gamma$  최종 상태에서의 새로운 물리  
현상 탐색

지도교수 양 운 기

이 논문을 이학박사 학위논문으로 제출함

2020 년 7 월

서울대학교 대학원

물리천문학부

남 경 욱

남경욱의 이학박사 학위논문을 인준함

2020 년 7 월

위 원 장 \_\_\_\_\_  
부위원장 \_\_\_\_\_  
위 원 \_\_\_\_\_  
위 원 \_\_\_\_\_  
위 원 \_\_\_\_\_

# Abstract

This thesis presents a search for  $Z\gamma$  resonances and a search for excited electrons and muons in  $\ell\ell\gamma$  final states at the LHC. The searches are based on a data sample of proton-proton collisions at a center-of-mass energy of 13 TeV. The data were collected with the CMS detector in 2016 and amounts to an integrated luminosity of  $35.9 \text{ fb}^{-1}$ . The observation is consistent with the standard model background prediction for both searches. Upper limits are set on the product of the production cross section and the branching fraction to  $Z\gamma$  for narrow and broad resonance scenarios with masses between 0.35 and 4.0 TeV. Besides, excited electrons and muons are excluded for masses below 3.9 and 3.8 TeV, respectively, under the assumption that the excited lepton mass equals the compositeness scale. The best observed limit on the compositeness scale is obtained with an excited lepton mass of around 1.0 TeV, excluding values below 25 TeV for both excited electrons and muons.

**Keywords:** SNU, High Energy Physics, thesis

**Student Number:** 2014-21353

# Contents

<b>Abstract</b>	<b>i</b>
<b>Chapter 1 Introduction</b>	<b>1</b>
<b>Chapter 2 Theoretical Background</b>	<b>5</b>
2.1 The Standard Model . . . . .	5
2.1.1 Birth of Quantum Field Theory . . . . .	5
2.1.2 Quantum Electrodynamics . . . . .	6
2.1.3 Weak Interaction . . . . .	9
2.1.4 Electroweak Symmetry Breaking . . . . .	13
2.1.5 Higgs Yukawa Couplings . . . . .	16
2.1.6 Flavor Physics . . . . .	19
2.1.7 Quantum Chromodynamics . . . . .	25
2.2 Physics Beyond the Standard Model . . . . .	26
2.2.1 Extended Higgs Sector . . . . .	27
2.2.2 Composite Higgs Models . . . . .	30
2.2.3 Compositeness and Excited Leptons . . . . .	31
<b>Chapter 3 Experimental Setup</b>	<b>38</b>
3.1 The Large Hadron Collider . . . . .	38

3.2	The Compact Muon Solenoid Experiment . . . . .	41
3.2.1	Coordinate System . . . . .	44
3.2.2	Tracker . . . . .	44
3.2.3	Electromagnetic Calorimeter . . . . .	46
3.2.4	Hadron Calorimeter . . . . .	48
3.2.5	Superconducting Solenoid Magnet . . . . .	49
3.2.6	Muon Detector . . . . .	50
3.2.7	Trigger and Data Acquisition . . . . .	52
3.3	Event Reconstruction . . . . .	53
3.3.1	Particle-Flow Reconstruction . . . . .	54
3.3.2	Muon Reconstruction . . . . .	55
3.3.3	Electron and Photon Reconstruction . . . . .	57
3.3.4	Hadron Reconstruction . . . . .	59
3.3.5	Jet Reconstruction . . . . .	60
3.3.6	Semileptonic $\tau$ Lepton Decay Reconstruction . . . . .	61
3.3.7	Missing Transverse Momentum Reconstruction . . . . .	63
<b>Chapter 4 Data and Simulated Samples</b>		<b>64</b>
4.1	Data . . . . .	64
4.2	Simulated Samples . . . . .	66
4.2.1	Parton Distribution Function . . . . .	66
4.2.2	Hard Process Generation . . . . .	67
4.2.3	Parton Showering and Hadronization . . . . .	68
4.2.4	Pileup Interactions . . . . .	69
4.2.5	Detector Simulation . . . . .	70
4.2.6	Signal Samples . . . . .	72
4.2.7	Background Samples . . . . .	73

<b>Chapter 5</b>	<b>Event Selection</b>	<b>74</b>
5.1	Electron and Photon Selection . . . . .	74
5.1.1	Isolation Criteria . . . . .	74
5.1.2	Shower Shape Criteria . . . . .	75
5.1.3	Electron Selection . . . . .	76
5.1.4	Photon Selection . . . . .	77
5.2	Muon Selection . . . . .	77
5.3	Resonant Signal Selection . . . . .	78
5.4	Nonresonant Signal Selection . . . . .	80
<b>Chapter 6</b>	<b>Background Modeling</b>	<b>81</b>
6.1	Background for the Resonant Signal Search . . . . .	81
6.1.1	Background Distribution in $m_{Z\gamma}$ . . . . .	81
6.1.2	Bias Estimation . . . . .	84
6.2	Background for the Nonresonant Signal Search . . . . .	85
6.2.1	Major Backgrounds . . . . .	85
6.2.2	Misidentified Photon Background Estimation . . . . .	86
<b>Chapter 7</b>	<b>Signal Modeling</b>	<b>92</b>
7.1	Resonant Signal . . . . .	92
7.1.1	Signal Distribution in $m_{Z\gamma}$ . . . . .	92
7.1.2	Signal Selection Efficiency and Detector Acceptance . . . . .	99
7.2	Nonresonant Signal . . . . .	99
7.2.1	Search Window in $m_{\ell\gamma}^{\min}-m_{\ell\gamma}^{\max}$ . . . . .	99
7.2.2	Signal Selection Efficiency and Detector Acceptance . . . . .	102
<b>Chapter 8</b>	<b>Systematic Uncertainties</b>	<b>104</b>
8.1	Systematic Uncertainties for the Resonant Signal Search . . . . .	104
8.2	Systematic Uncertainties for the Nonresonant Signal Search . . . . .	106

<b>Chapter 9 Results</b>	<b>109</b>
9.1 Statistical Interpretation . . . . .	110
9.1.1 Likelihood and Nuisance Parameters . . . . .	110
9.1.2 Maximum Likelihood Fit . . . . .	111
9.1.3 Exclusion Limits . . . . .	112
9.1.4 Significance . . . . .	115
9.2 Results of the Resonant Signal Search . . . . .	118
9.3 Results of the Nonresonant Signal Search . . . . .	120
 <b>Chapter 10 Conclusions</b>	 <b>126</b>
 초록	 <b>143</b>

# List of Figures

Figure 1.1	The Feynman diagram of the production of $Z\gamma$ resonances. . . . .	3
Figure 1.2	The Feynman diagram of the production of excited leptons in $\ell\ell\gamma$ final states. . . . .	4
Figure 2.1	Loop diagrams of $K^0 \rightarrow \mu^- \mu^+$ process. . . . .	22
Figure 2.2	Branching fractions of the various decay modes as a function of $m_{\ell^*}/\Lambda$ [36]. . . . .	37
Figure 3.1	Representation of the CERN accelerator complex. . . . .	39
Figure 3.2	Overview layout of the CMS detector [60]. . . . .	43
Figure 3.3	Longitudinal view of the CMS inner tracking system layout [60]. . . . .	45
Figure 3.4	Longitudinal view of the ECAL layout [61], representing one quarter of the detector. The barrel and endcaps sections and the preshower detector are shown. . . . .	47
Figure 3.5	Longitudinal view of the HCAL [63]. The locations of the HB, HE, HO and HF calorimeters are indicated. . . . .	49

Figure 3.6	A cross section of a quadrant of the CMS muon detector [64]. The orange, green, and blue regions denote respectively the DTs, CSCs, and RPCs subsystems. . . . .	50
Figure 3.7	A sketch of the specific particle interactions in a transverse slice of the CMS detector, from the beam interaction region to the muon detector. The muon and the charged pion are positively charged, and the electron is negatively charged. . . . .	55
Figure 6.1	Observed $m_{Z\gamma}$ invariant mass spectra in the $ee\gamma$ (left) and $\mu\mu\gamma$ (right) channels. The best fits to the background-only hypotheses are represented by the red lines, with their 68% CL uncertainty bands given by the gray shadings. Several narrow and broad signal benchmarks with arbitrary normalization are shown on top of the background prediction with the dashed lines. The lower panels show the difference between the data and the fits, divided by the uncertainty, which includes the statistical uncertainties in the data and the fit. For bins with a small number of entries, the error bars correspond to the Garwood confidence intervals [82]. . . . .	83
Figure 6.2	Median pull distributions before (left) and after (right) introducing the additional uncertainty. . . . .	84

Figure 6.3	The misidentification rate as a function of photon $p_T$ in the barrel (left) and endcap (right) regions. The error bars denote statistical uncertainties of bin-by-bin measurement and the error bands denote $1\sigma$ bands of fitting uncertainties. A polynomial function of photon $p_T$ (red line) is fitted to each histogram and the value is obtained by the value of the fitted function at a given photon $p_T$ . . . . .	87
Figure 6.4	Photon $p_T$ distributions of the data events and background predictions in the signal region. The background prediction in the left plot is purely based on simulation whereas the jet estimate from data is used for the right plot. . . . .	88
Figure 6.5	The $p_T$ distributions of leading electrons (upper) and leading muons (lower), using the jet background estimates from data before (left) and after (right) dilepton $p_T$ reweighting. . . . .	90
Figure 6.6	The $p_T$ distributions of subleading electrons (upper) and subleading muons (lower), using the jet background estimates from data before (left) and after (right) dilepton $p_T$ reweighting. . . . .	91
Figure 7.1	The CB fits to the signal simulation for the $ee\gamma$ (left column) and $\mu\mu\gamma$ (right column) channels for narrow resonances of mass 300 (upper row), 400 (middle row), and 500 GeV (lower row). . . . .	93

Figure 7.2	The CB fits to the signal simulation for the $ee\gamma$ (left column) and $\mu\mu\gamma$ (right column) channels for narrow resonances of mass 750 (upper row), 1000 (middle row), and 1500 GeV (lower row). . . . .	94
Figure 7.3	The CB fits to the signal simulation for the $ee\gamma$ (left column) and $\mu\mu\gamma$ (right column) channels for narrow resonances of mass 2000 (upper row), 3000 (middle row), and 4000 GeV (lower row). . . . .	95
Figure 7.4	The CB fits to the signal simulation for the $ee\gamma$ (left column) and $\mu\mu\gamma$ (right column) channels for broad resonances of mass 300 (upper row), 400 (middle row), and 500 GeV (lower row). . . . .	96
Figure 7.5	The CB fits to the signal simulation for the $ee\gamma$ (left column) and $\mu\mu\gamma$ (right column) channels for broad resonances of mass 750 (upper row), 1000 (middle row), and 1500 GeV (lower row). . . . .	97
Figure 7.6	The CB fits to the signal simulation for the $ee\gamma$ (left column) and $\mu\mu\gamma$ (right column) channels for broad resonances of mass 2000 (upper row), 3000 (middle row), and 4000 GeV (lower row). . . . .	98
Figure 7.7	The product of signal acceptance and efficiency as a function of the generated resonance mass for the $ee\gamma$ (red) and $\mu\mu\gamma$ (blue) channels, for narrow (left) and broad (right) resonances. Each marker denotes the value measured from the simulated signal sample at a given mass point, and the lines represent polynomial fits to the measured values. . . . .	100

Figure 7.8	The distributions of $m_{\ell\gamma}^{\min}$ (left column) and $m_{\ell\gamma}^{\max}$ (right column) in the $ee\gamma$ channel (upper row) and the $\mu\mu\gamma$ channel (lower row). The points with error bars denote the data and the stacked histograms show the predictions for each of the backgrounds. The uncertainty bands of the SM prediction includes only statistical uncertainties. Signal events for $m_{\ell^*} = 1$ TeV at $\Lambda = 10$ TeV are also shown as dotted lines. The last bin of each distribution includes overflow events. . . . .	101
Figure 7.9	The two-dimensional distributions of $m_{\ell\gamma}^{\max}$ versus $m_{\ell\gamma}^{\min}$ of excited electrons with a mass of 500 GeV (left) and of excited muons with a mass of 750 GeV (right), after the event selection, normalized to the expected signal cross section at $\Lambda = 10$ TeV. The red dashed lines denote the boundary of the L-shaped search window. . . . .	102
Figure 7.10	The two-dimensional distributions of $m_{\ell\gamma}^{\max}$ versus $m_{\ell\gamma}^{\min}$ of $DY+\gamma$ background events in the $ee\gamma$ (left) and $\mu\mu\gamma$ (right) channels, after the event selection, normalized to the cross section for $DY+\gamma$ production. . . . .	103
Figure 7.11	The product of signal acceptance and efficiency as a function of the generated excited lepton mass for the $ee\gamma$ (lower) and $\mu\mu\gamma$ (upper) channels. Each marker denotes the value measured from the simulated signal sample at a given mass point, and the lines represent polynomial fits to the measured values. . . . .	103

Figure 9.1	The left plot shows log-normal distributions with $\kappa = 1.10, 1.20, 1.33$ and $1.50$ . The right plots illustrates gamma distributions with the number of events in a control sample $B = 100, 25, 9$ and $4$ [91]. . . . .	112
Figure 9.2	Test statistic distributions for ensembles of pseudo-data generated for signal+background and background-only hypotheses. [91]. . . . .	114
Figure 9.3	(Left) An example of differential distribution of possible limits on $\mu$ for the background-only hypothesis ( $s = 1, b = 1$ , no systematic errors). (Right) Cumulative probability distribution of the plot on the left with 2.5%, 16%, 50%, 84%, and 97.5% quantiles (horizontal lines) defining the median expected limit as well as the $\pm 1\sigma$ (68%) and $\pm 2\sigma$ (95%) bands for the expected value of $\mu$ for the background-only hypothesis [91]. . .	115
Figure 9.4	(Left) The pdf of $q_0$ at $\mu = 0$ for the counting experiment. The solid curve is from the asymptotic formulae and the histograms are from Monte Carlo using different expected number of events $b = 2, 5, 20$ . (Right) The distributions at $\mu = 0$ and $1$ from both the asymptotic formulae and Monte Carlo simulation based on $s = 10, b = 10$ , and a scale factor for the number of background events $\tau = 1$ [94]. . . . .	116
Figure 9.5	An illustration of a hypothetical scan of the test statistic $q_0$ vs $m_H$ for some data. Up-crossings for a given threshold value $u$ are shown with blue points [91]. . . .	117

Figure 9.6	Observed (solid) and expected (dashed) 95% CL upper limits on $\sigma(X \rightarrow Z\gamma) \mathcal{B}(Z \rightarrow \ell\ell\gamma)$ , as a function of signal mass $m_X$ for the $ee\gamma$ (left column) and $\mu\mu\gamma$ (right column) channels, and for narrow (upper row) and broad (lower row) spin-0 resonances. The green and yellow shaded bands correspond to respective 68 and 95% CL ranges in the expected limits for the background-only hypothesis. . . . .	119
Figure 9.7	Observed (solid) and expected (dashed) 95% CL upper limits on $\sigma(X \rightarrow Z\gamma)$ as a function of signal mass $m_X$ , together with the 68% (green) and 95% (yellow) CL ranges of the expected limit for the background-only hypothesis, for the combination of the $ee\gamma$ and $\mu\mu\gamma$ channels for (left) narrow and (right) broad spin-0 resonances. . . . .	120
Figure 9.8	Observed (solid) and expected (dashed) 95% CL upper limits on the product of the production cross section and branching fraction as a function of signal mass $m_{\ell^*}$ , together with the 68% (green, inner) and 95% (yellow, outer) quantiles of the expected limit, for $e^*$ (left) and $\mu^*$ (right). . . . .	123
Figure 9.9	Observed (solid) and expected (dashed) 95% CL lower limits on the compositeness scale as a function of signal mass $m_{\ell^*}$ , together with the 68% (green, inner) and 95% (yellow, outer) quantiles of the expected limit, for $e^*$ (left) and $\mu^*$ (right). . . . .	124

# List of Tables

Table 2.1	Quantum numbers of fermions. . . . .	18
Table 2.2	Quantum numbers of the Higgs doublet. . . . .	18
Table 2.3	Quantum numbers of the strange quark and the scalar singlet. . . . .	20
Table 2.4	Elementary particles of the SM . . . . .	27
Table 3.1	Nominal parameters of the LHC machine in pp collisions.	40
Table 6.1	Results of the Fisher $F$ -test . . . . .	82
Table 8.1	Summary of the systematic uncertainties in the signal yield (upper part of the table) or shape (lower part of the table). A dash indicates that the uncertainty does not apply. . . . .	106
Table 8.2	Summary of the systematic uncertainties (in %) in the signal yield, the prompt photon background prediction, and the jet background prediction. . . . .	107

Table 9.1	The observed yield and the SM prediction in the search window of the given $m_{\ell^*}$ in the $ee\gamma$ channel. The symbols $N_{\text{data}}$ , $N_{\text{prompt}}$ , and $N_{\text{jet}}$ represent the number of events in data, the prompt photon background prediction, and the jet background estimate, respectively, together with statistical and systematical uncertainties. . . . .	121
Table 9.2	The observed yield and the SM prediction in the search window of the given $m_{\ell^*}$ in the $\mu\mu\gamma$ channel. The symbols $N_{\text{data}}$ , $N_{\text{prompt}}$ , and $N_{\text{jet}}$ represent the number of events in data, the prompt photon background prediction, and the jet background estimate, respectively, together with statistical and systematical uncertainties. . . . .	122
Table 9.3	Summary of the observed (expected) lower limits on $m_{\ell^*}$ , assuming $\Lambda = m_{\ell^*}$ , and the best observed (expected) lower limits on $\Lambda$ in the mass range 0.5–1.0 TeV. . . . .	125

# Chapter 1

## Introduction

The standard model (SM) of particle physics provides a very precise description of various phenomena in particle physics observed over the last half century. Despite its huge success, however, there are a number of fundamental questions that still remain unanswered. For example, the SM cannot explain the existence of fermion generations and the mass hierarchy between fermions. It is also unknown why the Higgs mass is unnaturally light and what is the dynamic origin of the Higgs mechanism. For these reasons, the SM is widely believed to be incomplete. So far, physicists have proposed various theories to explain physics beyond the SM (BSM). Many of BSM models predict new physics phenomena that leave unique signatures in  $ll\gamma$  final states. In  $ll\gamma$  final states, a clear signature of a same-flavor lepton pair and a photon allows the precise measurement of final-state particles and thereby highly efficient signal selection. Moreover, only a small contribution of nonresonant SM processes is expected in the  $m_{ll\gamma}$  region above the Z boson and the H boson resonances, on which a majority of BSM theories is currently focusing. If new heavy res-

onances decay to  $ll\gamma$  final states, their masses can be reconstructed in great precision such that the reconstructed resonance peaks are clearly distinguished from nonresonant SM processes in the spectrum of  $m_{ll\gamma}$ . Nonresonant signals can also be discovered in  $ll\gamma$  final states by exploiting a precise description on  $ll\gamma$  kinematics as well as an advantage of a small SM background contribution. This thesis accounts for both resonant and nonresonant physics signatures in  $ll\gamma$  final states.

In the  $ll\gamma$  invariant mass spectrum, resonance peaks other than known SM particles may be signs of new neutral bosons. Such bosons are predicted in many extensions of the SM, such as technicolor [1] and little Higgs [2] models, as well as models with an extended Higgs boson sector [3, 4] or with extra spatial dimensions [5, 6]. It is particularly interesting to explore bosonic decay channels, which can dominate if the couplings of a new resonance to fermions are suppressed. Diboson decays involving photons, i.e.,  $Z\gamma$ , and  $\gamma\gamma$  channels, are also important, as the search in the  $\gamma\gamma$  channel demonstrated by contributing significantly to the discovery of the Higgs boson by the ATLAS and CMS Collaborations in 2012 [7–9]. While a resonance decaying to diphotons cannot be a vector or an axial vector, due to the Landau–Yang theorem [10, 11], having one of the two bosons massive alleviates this constraint. Thus, neutral bosons of spin 0, 1, or 2 can be sought in the  $Z\gamma$  channel, leading to a broad search program.

New fermionic states called excited fermions, on the other hand, can leave nonresonant signatures in  $ll\gamma$  final states. Their existence is predicted by compositeness models [12–21]. Compositeness models suggest that quarks and leptons are themselves made of fundamental constituents that are bound by a new strong interaction with a characteristic energy scale  $\Lambda$  (called the compositeness scale). In proton-proton (pp) collisions, excited fermions could be

produced via contact interactions (CI) and decay either through SM gauge interactions or through CI to SM fermions.

This thesis is devoted to a search for  $Z\gamma$  resonances (resonant signal search) [22] and a search for excited leptons (nonresonant signal search) [23] in  $\ell\ell\gamma$  final states. The resonant signal search is conducted for a resonance with a relatively narrow width appearing as an excess over the smooth  $Z\gamma$  invariant mass ( $m_{Z\gamma}$ ) spectrum constructed from an energetic photon and the  $Z \rightarrow \ell\ell$  decay products as illustrated in Fig. 1.1. The  $Z$  boson decays are reconstructed using an electron or a muon pair. The nonresonant signal search is performed for excited leptons ( $\ell^* = e^*, \mu^*$ ) in  $\ell\ell\gamma$  ( $\ell = e, \mu$ ) final states where the excited lepton decays to a SM lepton and a photon ( $\ell^* \rightarrow \ell\gamma$ ) as illustrated in Fig. 1.2. Unlike the resonant signal search, there is an ambiguity in reconstructing the excited lepton mass because of the two possible pairings of a lepton and the photon. For this search, information of both invariant masses is used to discriminate the excited lepton signal from SM background processes.

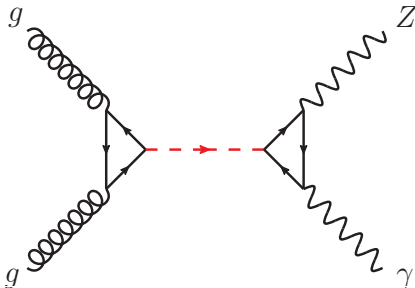


Figure 1.1: The Feynman diagram of the production of  $Z\gamma$  resonances.

Similar searches for  $Z\gamma$  resonances have been recently published by ATLAS [24] at  $\sqrt{s} = 13$  TeV and by CMS at  $\sqrt{s} = 8$  and 13 TeV [25], based on significantly lower  $\sqrt{s}$  or smaller integrated luminosities. Other searches for  $Z\gamma$  resonances have been performed only in the leptonic channel. These include

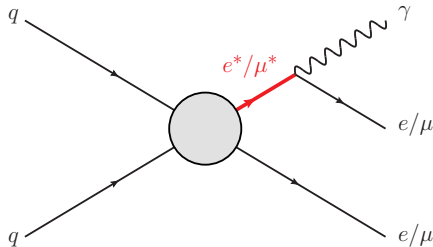


Figure 1.2: The Feynman diagram of the production of excited leptons in  $ll\gamma$  final states.

searches by the L3 Collaboration at the CERN LEP [26] and the D0 Collaboration at the Fermilab Tevatron [27, 28]. They have also been done by ATLAS at  $\sqrt{s} = 7, 8,$  and  $13$  TeV [29–31], and CMS at  $\sqrt{s} = 8$  and  $13$  TeV [32], as well as by ATLAS and CMS using the combined 7 and 8 TeV data [33, 34], and by ATLAS using the 13 TeV data [31] in the context of a search for the  $H \rightarrow Z\gamma$  decay.

Searches for excited leptons have been previously performed by the CMS Collaboration [35–37], but no evidence for their existence was found. Searches at the LEP [38–41], HERA [42], and Tevatron [43–46] colliders, and by the ATLAS Collaboration at  $\sqrt{s} = 7$  TeV [47], 8 TeV [48, 49], and 13 TeV [50] also found no evidence for the existence of excited leptons.

# Chapter 2

## Theoretical Background

### 2.1 The Standard Model

The SM of the particle physics is the theory that explains physics phenomena in terms of elementary particles and fundamental forces in the universe. It has provided incredibly precise descriptions on most of known particle physics phenomena so far. The SM was developed in the 20th century and has been completed by the recent discovery of the Higgs boson, which was considered as the only missing piece of the SM for a long time. The essentials of the SM are summarized in this section.

#### 2.1.1 Birth of Quantum Field Theory

A natural starting point for describing the SM could be its theoretical framework, quantum field theory (QFT). QFT was initiated as an attempt to build up a quantum theory consistent with Einstein's theory of special relativity. One of the very first attempts was made by Dirac. He was trying to formulate a relativistic version of the Schrödinger equation from the relativistic disper-

sion relation  $E^2 = p^2c^2 + m^2c^4$ . Dirac soon realized that it is impossible to make the desired linear equation out of scalar numbers and the only way to achieve it is exploiting matrices instead of numbers. This enlightenment led to the derivation of the Dirac equation

$$i\gamma^\mu \partial_\mu \psi - m\psi = 0, \quad (2.1)$$

with a 4-component column vector  $\psi$  and  $4 \times 4$  matrices  $\gamma^\mu$

$$\gamma^0 = \begin{pmatrix} 0 & I \\ I & 0 \end{pmatrix}, \quad \gamma^1 = \begin{pmatrix} 0 & \sigma_1 \\ -\sigma_1 & 0 \end{pmatrix}, \quad \gamma^2 = \begin{pmatrix} 0 & \sigma_2 \\ -\sigma_2 & 0 \end{pmatrix}, \quad \gamma^3 = \begin{pmatrix} 0 & \sigma_3 \\ -\sigma_3 & 0 \end{pmatrix}. \quad (2.2)$$

In the definition of  $\gamma^\mu$ ,  $\sigma_i$  represent  $2 \times 2$  Pauli matrices

$$\sigma_1 = \begin{pmatrix} 0 & 1 \\ 1 & 0 \end{pmatrix}, \quad \sigma_2 = \begin{pmatrix} 0 & -i \\ i & 0 \end{pmatrix}, \quad \sigma_3 = \begin{pmatrix} 1 & 0 \\ 0 & -1 \end{pmatrix}. \quad (2.3)$$

As the appearance of Pauli matrices indicates, the solution of the original Dirac equation represents the classical electron field. The Dirac equation is now considered as the equation of motion for all free spin- $\frac{1}{2}$  massive fermions. By quantizing the classical electron field together with the classical massless photon field, Dirac successfully derived the relativistic quantum theory of the electromagnetic interaction, which is considered as the first complete QFT. This theory is now called quantum electrodynamics (QED).

### 2.1.2 Quantum Electrodynamics

The Dirac equation can be applied to all the (visible) matters in the universe, but unfortunately, only within the limit of no interactions. The SM explain interactions of elementary particles by means of fundamental forces except gravity; the electromagnetic interaction, the weak interaction, and the strong

interaction. We can start with the electromagnetic interaction theory following Dirac's derivation.

The Dirac Lagrangian can serve as a good starting point of our derivation:

$$\mathcal{L} = \bar{\psi}(i\gamma^\mu\partial_\mu - m)\psi, \quad (2.4)$$

with  $\bar{\psi} = \psi^\dagger\gamma^0$ . We can easily see that the Lagrangian is invariant under global phase transformations on  $\psi$ , i.e., global  $U(1)$  transformations

$$\psi' = e^{ia\theta}\psi. \quad (2.5)$$

The following question is, will the Lagrangian be still invariant under local  $U(1)$  transformations?

$$\psi' = e^{ia\theta(x)}\psi. \quad (2.6)$$

Unfortunately, the derivative term in Eq. 2.4 breaks the local symmetry. An extra term that is added to the original Lagrangian after transformation is

$$i\partial_\mu\theta[ia\bar{\psi}\gamma^\mu\psi]. \quad (2.7)$$

The most straightforward approach to recover the local  $U(1)$  gauge symmetry is adding more terms that their own extra terms after transformation would cancel out the extra term above. This is the place where a gauge boson intervenes in the theory. The Lagrangian of a gauge boson field  $B_\nu$  can be described as

$$\mathcal{L} = -\frac{1}{4}B^{\mu\nu}B_{\mu\nu} + \frac{1}{2}m^2B^\mu B_\mu - j^\mu B_\mu, \quad (2.8)$$

where  $B_{\mu\nu} = \partial_\mu B_\nu - \partial_\nu B_\mu$  is the field strength tensor and  $j^\mu$  is the corresponding conserved current. Under local  $U(1)$  gauge transformations, the gauge boson field is transformed as

$$B'_\mu = B_\mu - \frac{1}{g_1}\partial_\mu\chi(x), \quad (2.9)$$

with an arbitrary scalar function  $\chi(x)$ . We can easily see that the field strength tensor is invariant under the transformations, but the mass term of the gauge field breaks the symmetry again. Therefore, the gauge boson is assumed to be massless,

$$\mathcal{L} = -\frac{1}{4}B^{\mu\nu}B_{\mu\nu} - j^\mu B_\mu. \quad (2.10)$$

The Lagrangian is still not invariant under the transformation but has an extra term

$$\frac{1}{g_1}j^\mu\partial_\mu\chi(x). \quad (2.11)$$

We can expect that this term cancels out the extra term from the Dirac Lagrangian, Eq. 2.7, and recover the symmetry. The generator of the local  $U(1)$  gauge symmetry is obviously set to be the same for both Lagrangians,  $\chi(x) = \theta(x)$ , and the conserved current has the form of

$$j^\mu = ag_1\bar{\psi}\gamma^\mu\psi. \quad (2.12)$$

Finally, we can obtain the Lagrangian invariant under local  $U(1)$  gauge transformations from the combination of the Dirac Lagrangian and the Lagrangian of the gauge field

$$\mathcal{L} = \bar{\psi}(i\gamma^\mu\partial_\mu - m)\psi - \frac{1}{4}B^{\mu\nu}B_{\mu\nu} - ag_1\bar{\psi}\gamma^\mu\psi B_\mu. \quad (2.13)$$

This Lagrangian consists of the kinetic terms of the fermion and the gauge boson fields, the mass term of the fermion field, and coupling terms between the fermion and the gauge boson fields. The concept of a covariant derivative,  $D_\mu = \partial_\mu + iag_1B_\mu$ , is particularly useful here, allowing us to rewrite the Lagrangian as below.

$$\mathcal{L} = \bar{\psi}(i\gamma^\mu D_\mu - m)\psi - \frac{1}{4}B^{\mu\nu}B_{\mu\nu}. \quad (2.14)$$

Using the idea of gauge invariance, we have just formulated QED, which fully describes the interaction of fermions by means of exchange of photons, massless  $U(1)$  gauge bosons.

Since its development, QED has been famous for its extremely precise predictions on various electromagnetic observables. One of the most precise QED predictions is made on the anomalous magnetic momentum of the electron. The QED prediction value is calculated as

$$a_e(\text{theory}) = 1159652182.032(720) \times 10^{-12}, \quad (2.15)$$

which shows a remarkable agreement up to 9 significant figures with the latest experimental result [51]

$$a_e(\text{exp}) = 1159652180.73(28) \times 10^{-12}, \quad (2.16)$$

where  $a_e = (g - 2)/2$  and magnetic moment  $\mu = g \frac{e}{2m} S$ . Various precision tests carried out by comparing experimental results and QED predictions have proven that QED is the most precise theory in physics.

### 2.1.3 Weak Interaction

Notwithstanding the huge success of QED, there were various phenomena such as  $\beta$ -decays that cannot be explained by QED, shedding light on the existence of a new fundamental force with the corresponding gauge bosons. It led to the development of the weak interaction theory.

In a theoretical point of view, the simplest way to introduce new gauge bosons is the expansion of the previously discussed  $U(1)$  gauge theory to a  $SU(2)$  gauge theory. First of all, we need to introduce a fermion  $SU(2)$  doublet

$$q = \begin{pmatrix} u \\ d \end{pmatrix}, \quad (2.17)$$

with

$$q^\dagger = \begin{pmatrix} u^\dagger & d^\dagger \end{pmatrix}, \quad \bar{q} = q^\dagger \gamma^0 = \begin{pmatrix} \bar{u} & \bar{d} \end{pmatrix}. \quad (2.18)$$

Using doublets, the Dirac Lagrangian can be rewritten as

$$\mathcal{L} = \bar{q}(i\gamma^\mu \partial_\mu - m_q)q, \quad (2.19)$$

with

$$m_q = \begin{pmatrix} m_u & 0 \\ 0 & m_d \end{pmatrix}. \quad (2.20)$$

The symbol  $m_u$  represents the mass of a fermion  $u$  and  $m_d$  is the mass of a fermion  $d$ . A fermion doublet is transformed under  $SU(2)$  gauge transformations as

$$q' = e^{i\vec{\tau} \cdot \vec{\theta}} q, \quad (2.21)$$

with the generators of  $SU(2)$   $\tau_i$ .  $\tau_i$  satisfy the following commutation relations:

$$[\tau_i, \tau_j] = i\epsilon_{ijk}\tau_k. \quad (2.22)$$

An infinitesimal transformation  $\theta_i$  can be either a constant or a function of space-time coordinates, depending on whether the transformation is global or local.  $\tau_i$  can be chosen as Pauli matrices with a factor of  $\frac{1}{2}$

$$\tau_i = \frac{1}{2}\sigma_i, \quad (2.23)$$

and Eq. 2.21 can be rewritten as

$$q' = e^{i\frac{1}{2}\vec{\sigma} \cdot \vec{\theta}} q. \quad (2.24)$$

We can check out the global  $SU(2)$  symmetry of the Lagrangian Eq. 2.19 first. It is clearly broken due to non-zero off-diagonal terms in  $\sigma_1$  and  $\sigma_2$ . To achieve the global  $SU(2)$  gauge invariance of the Lagrangian, the masses of two fermions,  $u$  and  $d$ , should be the same non-zero or the same zero ( $m_u = m_d \neq 0$  or  $m_u = m_d = 0$ ).

It is necessary to discuss the chiral symmetry in order to figure out the masses of the fermions. The discussion could start with the Lorentz symmetry which is imposed on any valid quantum field theories. The proper, orthochronous Lorentz group  $SO(3, 1)$  has  $J_i$  and  $K_i$ , the generators of rotations and Lorentz boosts, respectively. They satisfy the following algebra:

$$[J_i, J_j] = i\epsilon_{ijk}J_k, \quad [J_i, K_j] = i\epsilon_{ijk}K_k, \quad [K_i, K_j] = -i\epsilon_{ijk}J_k. \quad (2.25)$$

Their combinations  $L_i$  and  $R_i$  are defined as

$$L_i = \frac{J_i + iK_i}{2}, \quad R_i = \frac{J_i - iK_i}{2}. \quad (2.26)$$

$L_i$  and  $R_i$  also satisfy the following relations:

$$[L_i, L_j] = i\epsilon_{ijk}L_k, \quad [R_i, R_j] = i\epsilon_{ijk}R_k, \quad [L_i, R_j] = 0, \quad (2.27)$$

so that they form two separate  $SU(2)$  algebras. For spinors, there are two representations that satisfy

$$\left[\frac{\sigma_i}{2}, \frac{\sigma_j}{2}\right] = i\epsilon_{ijk}\frac{\sigma_k}{2}. \quad (2.28)$$

One is  $L_i = \frac{\sigma_i}{2}$  and  $R_i = 0$ , called the left-handed spinor representation, and the other is  $L_i = 0$  and  $R_i = \frac{\sigma_i}{2}$ , called the right-handed spinor representation. 2-component spinors that satisfy these representations are called Weyl spinors. A 4-component Dirac spinor in the Dirac Lagrangian can be formed of two Weyl spinors (in the Weyl basis of  $\gamma$  matrices)

$$\psi = \begin{pmatrix} \psi_L \\ \psi_R \end{pmatrix}. \quad (2.29)$$

The Weyl spinors  $\psi_L$  and  $\psi_R$  are called the left- and right-handed spinors, respectively. In the Weyl basis, the projection operators are defined as

$$P_L = \frac{1}{2}(1 - \gamma^5), \quad P_R = \frac{1}{2}(1 + \gamma^5). \quad (2.30)$$

They act on Dirac spinors as follows:

$$P_L\psi = \psi_L (= \begin{pmatrix} \psi_L \\ 0 \end{pmatrix}), \quad P_R\psi = \psi_R (= \begin{pmatrix} 0 \\ \psi_R \end{pmatrix}). \quad (2.31)$$

A global  $U(1)$  symmetry can also work separately on two representations

$$\psi' = e^{iaP_L}\psi, \quad \psi' = e^{iaP_R}\psi. \quad (2.32)$$

Two types of global symmetries are involved with Eq. 2.32. One is the  $U(1)$  gauge symmetry in Eq. 2.5, denoted by  $U(1)_V$ . The other one is called an axial  $U(1)$  symmetry,  $U(1)_A$ , which corresponds to a transformation  $\psi' = e^{ia\gamma^5}\psi$ .  $U(1)_A$  requires fermions to be massless in the Dirac Lagrangian, and so do two transformations in Eq. 2.32. The symmetry corresponding to the first transformation is denoted by  $U(1)_L$  and the second one is called  $U(1)_R$ . The chiral  $U(1)$  symmetry is  $U(1)_L \times U(1)_R$ . The requirement of the chiral  $U(1)$  symmetry leads to massless fermions:

$$\mathcal{L} = \bar{q}(i\gamma^\mu\partial_\mu)q \quad (2.33)$$

We are now ready to examine local  $SU(2)$  gauge transformations. The massless doublet Lagrangian Eq. 2.33 is not invariant under local  $SU(2)$  transformations due to the derivative term, just like the case of local  $U(1)$  transformations. In the same way that we dealt with the local  $U(1)$  case, we need to add gauge field terms to cancel out the extra term from the derivative of fermion fields. There are 3 gauge boson fields,  $W^i$  with  $i = 1, 2, 3$ , each corresponding to one of 3 generators of  $SU(2)$ . Local  $SU(2)$  transformations operate on the gauge bosons as follows:

$$W_\mu^i = W_\mu^i - \frac{1}{g_2}\partial_\mu\theta_i - \epsilon^{ijk}\theta_j W_\mu^k. \quad (2.34)$$

A remarkable difference between  $U(1)$  and  $SU(2)$  gauge bosons lies in the last term in Eq. 2.34. It stems from the fact that  $U(1)$  is an abelian group whereas

$SU(2)$  is a non-abelian group. The Lagrangian of the  $SU(2)$  gauge bosons is written as

$$\mathcal{L} = -\frac{1}{4}\vec{W}^{\mu\nu} \cdot \vec{W}_{\mu\nu} - \vec{j}^\mu \cdot \vec{W}_\mu, \quad (2.35)$$

where  $\vec{W}_{\mu\nu} = \partial_\mu \vec{W}_\nu - \partial_\nu \vec{W}_\mu - g_2 \vec{W}_\mu \times \vec{W}_\nu$  is the field strength tensor. The covariant derivative of local  $U(1)$  hints the form of the covariant derivative of local  $SU(2)$

$$D_\mu = \partial_\mu + ig_2 \vec{\tau} \cdot \vec{W}^{\mu}, \quad (2.36)$$

which transforms as

$$D'_\mu q' = (\partial_\mu + ig_2 \vec{\tau} \cdot \vec{W}'_\mu) e^{i\vec{\tau} \cdot \vec{\theta}} q = e^{i\vec{\tau} \cdot \vec{\theta}} D_\mu q. \quad (2.37)$$

In the same way that we did for the local  $U(1)$  case, we can finally construct the Lagrangian invariant under local  $SU(2)$

$$\mathcal{L} = \bar{q}(i\gamma^\mu D_\mu)q - \frac{1}{4}\vec{W}^{\mu\nu} \cdot \vec{W}_{\mu\nu} \quad (2.38)$$

#### 2.1.4 Electroweak Symmetry Breaking

So far we have successfully formulated local  $U(1)$  and  $SU(2)$  gauge theories. However, it leads to a conflict with the real world observations. Unlike Eq. 2.38, we have already discovered a number of massive fermions and gauge bosons in the universe and even measured most of their masses in a great precision. Instead of a brutal force approach used above, therefore, a more elegant mechanism is introduced in the SM to explain both the particle masses and gauge invariance consistently. This mechanism is now known as spontaneous symmetry breaking, also called the Higgs mechanism in the context of the electroweak theory.

The idea of spontaneous symmetry breaking starts with the introduction of a scalar doublet that couples to both  $U(1)$  and  $SU(2)$  gauge bosons, forming

$SU(2) \times U(1)$ .

$$\Phi = \begin{pmatrix} \varphi_+ \\ \varphi_0 \end{pmatrix} = \frac{1}{\sqrt{2}} \begin{pmatrix} \varphi_1 + i\varphi_2 \\ \varphi_3 + i\varphi_4 \end{pmatrix}. \quad (2.39)$$

The Lagrangian of the scalar doublet with  $SU(2) \times U(1)$  is written as

$$\mathcal{L} = (D^\mu \Phi)^\dagger D_\mu \Phi - \frac{1}{2} \lambda^2 (\Phi^2 - \frac{1}{2} v^2)^2 - \frac{1}{4} \vec{W}^{\mu\nu} \cdot \vec{W}_{\mu\nu} - \frac{1}{4} B^{\mu\nu} B_{\mu\nu}, \quad (2.40)$$

with the covariant derivative

$$D_\mu = \partial_\mu + i \frac{g_2}{2} \vec{\sigma} \cdot \vec{W}^\mu + i \frac{g_1}{2} Y B_\mu. \quad (2.41)$$

The critical point of the mechanism is the second term in the Lagrangian, the potential of  $\Phi$ . The potential have its minima, the vacuum states of  $\Phi$ , at  $|\Phi| = v$ .  $v$  is called the vacuum expectation value (VEV). Among all the possible vacuums at  $\Sigma_i \varphi_i^2 = v^2$ , we can fix a specific vacuum

$$\langle \Phi \rangle = \Phi_0 = \frac{1}{\sqrt{2}} \begin{pmatrix} 0 \\ v \end{pmatrix}, \quad (2.42)$$

The scalar field can be expanded in terms of a physical scalar field  $h(x)$  that is defined as a perturbation from the chosen vacuum

$$\Phi = \eta + \langle \Phi \rangle = \frac{1}{\sqrt{2}} \begin{pmatrix} 0 \\ v + h(x) \end{pmatrix}. \quad (2.43)$$

The physical field  $h(x)$ , named the Higgs boson, is well known as the final missing piece of the SM until the recent discovery in 2012. The whole Lagrangian then can be rewritten in an expansion of the physical Higgs field term, eventually breaking the symmetry of  $SU(2) \times U(1)$ . Considering the form of a gauge boson mass term, the mass terms of the gauge bosons are derived from the expansion of the kinetic term in Eq. 2.40 as follows:

$$\frac{1}{8} \left| \begin{pmatrix} g_2 W_\mu^3 + g_1 B_\mu & g_2 \sqrt{2} W_\mu^- \\ g_2 \sqrt{2} W_\mu^+ & -g_2 W_\mu^3 + g_1 B_\mu \end{pmatrix} \begin{pmatrix} 0 \\ v \end{pmatrix} \right|^2 \quad (2.44)$$

$$= \left(\frac{g_2 v}{2}\right)^2 W_\mu^+ W_\mu^- + \frac{1}{8} v^2 \begin{pmatrix} W_\mu^3 & B_\mu \end{pmatrix} \begin{pmatrix} g_2^2 & -g_1 g_2 \\ -g_1 g_2 & g_1^2 \end{pmatrix} \begin{pmatrix} W_\mu^3 \\ B_\mu \end{pmatrix} \quad (2.45)$$

$$= \left(\frac{g_2 v}{2}\right)^2 W_\mu^+ W_\mu^- + \frac{1}{8} v^2 (g_1^2 + g_2^2) \begin{pmatrix} A_\mu & Z_\mu \end{pmatrix} \begin{pmatrix} 0 & 0 \\ 0 & 1 \end{pmatrix} \begin{pmatrix} A_\mu \\ Z_\mu \end{pmatrix} \quad (2.46)$$

$$= \left(\frac{g_2 v}{2}\right)^2 W_\mu^+ W_\mu^- + \frac{1}{2} \left(\frac{v}{2} \sqrt{g_1^2 + g_2^2}\right)^2 Z_\mu^2, \quad (2.47)$$

with  $W_\mu^\pm = \frac{(W_\mu^1 \mp i W_\mu^2)}{\sqrt{2}}$ . The matrix in Eq. 2.45 is diagonalized by defining physical fields as

$$A_\mu = \frac{g_2 B_\mu + g_1 W_\mu^3}{\sqrt{g_1^2 + g_2^2}}, \quad Z_\mu = \frac{-g_1 B_\mu + g_2 W_\mu^3}{\sqrt{g_1^2 + g_2^2}}. \quad (2.48)$$

As a result, four physical gauge bosons are born from spontaneous symmetry breaking. The two charged gauge bosons,  $W_\mu^\pm$  bosons of the same mass  $\frac{g_2 v}{2}$ , are named  $W^+$  and  $W^-$  bosons. They are responsible for the charged currents of *beta*-decays. There are also the two neutral gauge bosons  $A_\mu$  and  $Z_\mu$ , which are originated from two orthogonal combinations of  $B_\mu$  and  $W_\mu^3$  fields.  $A_\mu$  is massless, and therefore represents the physical photon field.  $Z_\mu$  of mass  $\frac{v}{2} \sqrt{g_1^2 + g_2^2}$  is a massive neutral gauge boson involved with the weak interaction, called the Z boson. Finally, we have the Glashow–Weinberg–Salam’s electroweak theory. The weak mixing angle is defined as

$$\sin\theta_W = \frac{g_1}{\sqrt{g_1^2 + g_2^2}}, \quad \cos\theta_W = \frac{g_2}{\sqrt{g_1^2 + g_2^2}}. \quad (2.49)$$

At the time the electroweak theory was first formulated, there were no experimental evidences on the existence of the Z boson. Therefore, the discovery of the Z boson together with the  $W^\mp$  bosons in 1983 is now considered as another triumph of the SM and particle physics.

### 2.1.5 Higgs Yukawa Couplings

The next step is to address the mass of fermions. Before getting to the point, it is particularly useful to identify fermions as the eigenstates of  $SU(2) \times U(1)$ . This information is not only necessary to understand the quantum numbers of fermions from the real world observations but also will be used to ensure the gauge invariance in the latter stages of the discussion.

We can first consider the eigenvalues of  $SU(2)$  called weak isospins, the analogy of spins in the rotational symmetry. There are singlet and doublet states in  $SU(2)$  and only doublets could couple to the off-diagonal weak gauge bosons,  $W^\pm$ . Which fermion is an  $SU(2)$  singlet and which one is a doublet can be determined by the experimental results. First of all, the parity violation of  $\beta$ -decays was discovered by the Wu's experiment [52]. The following Goldhaber experiment [53] determined the helicity of the neutrino, which turned out to be all left-handed. In addition, observations on the suppression of the electronic decay mode of  $\pi^\pm$  compared to the muonic decay mode [54, 55] suggests the left-handed weak charged interaction. Therefore, we can conclude that only the left-handed chirality of fermions contributes to  $SU(2)$  doublets and the right-handed fermions must be singlets.

The eigenvalue of the total weak isospin,  $I_W$ , for doublets is obviously  $\frac{1}{2}$  and the eigenvalues of the third isospin component  $I_W^3$  are  $\pm\frac{1}{2}$ .

$$\ell_L = \begin{pmatrix} \nu_L \\ e_L \end{pmatrix}, \quad q_L = \begin{pmatrix} u_L \\ d_L \end{pmatrix} \quad (2.50)$$

$$I_W = \frac{1}{2}, \quad I_W^3 = \pm\frac{1}{2}. \quad (2.51)$$

On the other hand, the right-handed fermions are in a trivial representation.

$$e_R, \quad u_R, \quad d_R \quad (2.52)$$

$$I_W = I_W^3 = 0. \quad (2.53)$$

Unlike the other right-handed fermions, the right-handed neutrinos have never been observed experimentally. Neutrinos in the SM, therefore, are assumed to be massless and consequently there are no Yukawa couplings to neutrinos, which intrinsically include the right-handed terms. As a result, we can now reduce  $SU(2) \times U(1)$  to  $SU(2)_L \times U(1)$ .

It is time to discuss the remaining component of  $SU(2) \times U(1)$ ,  $U(1)$ . After the symmetry breaking of  $SU(2) \times U(1)$ , there is a remaining local  $U(1)$  gauge symmetry involved with the physical photon field. We denote it by  $U(1)_{em}$  to distinguish from the original symmetry in  $SU(2) \times U(1)$ . The quantum number of  $U(1)_{em}$ ,  $Q$ , is the one that we can observe from the real world, the electric charge of particles. The quantum number of the original  $U(1)$ ,  $\frac{Y}{2}$ , is called the weak hypercharge instead. We can derive the relation between the conserved charges of  $SU(2)$ ,  $U(1)$  and  $U(1)_{em}$  from the covariant derivative in Eq. 2.41 and the physical photon field as below.

$$Q = I_W^3 + \frac{Y}{2} \quad (2.54)$$

We now have all the quantum numbers of fermions with respect to the original  $SU(2) \times U(1)$  and  $U(1)_{em}$ , summarized in Table 2.1. The quantum numbers of the Higgs doublet can be obtained in the same way, summarized in Table 2.2.

For fermions, Yukawa interactions with the Higgs field play an important role in their mass generation. Leptons and down-type quarks have Yukawa couplings to the Higgs field as follows:

$$\begin{aligned} \mathcal{L}_{Yukawa,\ell} &= -y_\ell \bar{\ell}_L \Phi e_R - y_\ell \bar{e}_R \Phi^\dagger \ell_L \\ \mathcal{L}_{Yukawa,d} &= -y_d \bar{q}_L \Phi d_R - y_d \bar{d}_R \Phi^\dagger q_L, \end{aligned} \quad (2.55)$$

Table 2.1: Quantum numbers of fermions.

Particle	Hypercharge ( $Y$ )	Weak isospin( $I_W$ )	Electric Charge ( $Q$ )
$q_L$	$\frac{1}{3}$	$\frac{1}{2}$	$+\frac{2}{3} (u_L) / -\frac{1}{3} (d_L)$
$u_R$	$\frac{4}{3}$	0	$+\frac{2}{3}$
$d_R$	$-\frac{2}{3}$	0	$-\frac{1}{3}$
$\ell_L$	-1	$\frac{1}{2}$	0 ( $\nu_L$ ) / -1 ( $e_L$ )
$e_R$	-2	0	-1

Table 2.2: Quantum numbers of the Higgs doublet.

Particle	Hypercharge ( $Y$ )	Weak isospin( $I_W$ )	Electric Charge ( $Q$ )
$\Phi$	1	$\frac{1}{2}$	$\varphi_+ = +1, \quad \varphi_0 = 0$

where  $y_\ell$  and  $y_d$  are called as the Yukawa coupling of each fermion and free parameters of the SM. We can easily check the  $SU(2)_L \times U(1)$  gauge invariance of the Yukawa coupling terms of leptons in Eq. 2.55:

$$\begin{aligned}
 \bar{\ell}'_L \Phi' e'_R &= \bar{\ell}_L e^{-i(\frac{1}{2}Y_{\ell,L} + \vec{\tau} \cdot \vec{\theta})} e^{i(\frac{1}{2}Y_\Phi \theta + \vec{\tau} \cdot \vec{\theta})} \Phi e^{i\frac{1}{2}Y_{e,R}\theta} e_R \\
 &= e^{i\frac{1}{2}(-Y_{\ell,L} + Y_\Phi + Y_{e,R})} \bar{\ell}_L \Phi e_R = \bar{\ell}_L \Phi e_R.
 \end{aligned}
 \tag{2.56}$$

The last equivalence comes from  $(-Y_{\ell,L} + Y_\Phi + Y_{e,R}) = (1 + 1 - 2) = 0$ . In the same way, the gauge invariance also holds for the couplings of down-type quarks, given  $(-Y_{q,L} + Y_\Phi + Y_{d,R}) = (-\frac{1}{3} + 1 - \frac{2}{3}) = 0$ . After spontaneous symmetry breaking, i.e., expanding the Higgs terms with the physical Higgs field perturbatively, the Yukawa coupling terms turn out to be

$$\begin{aligned}
 \mathcal{L}_{Yukawa,\ell} &= -\frac{y_\ell}{\sqrt{2}}(h + v)(\bar{e}_L e_R + \bar{e}_R e_L) \\
 \mathcal{L}_{Yukawa,d} &= -\frac{y_d}{\sqrt{2}}(h + v)(\bar{d}_L d_R + \bar{d}_R d_L).
 \end{aligned}
 \tag{2.57}$$

Back to Dirac spinors,

$$\begin{aligned}\mathcal{L}_{Yukawa,\ell} &= -\frac{y_\ell v}{\sqrt{2}}\bar{e}e - \frac{y_\ell}{\sqrt{2}}h\bar{e}e \\ \mathcal{L}_{Yukawa,d} &= -\frac{y_d v}{\sqrt{2}}\bar{d}d - \frac{y_d}{\sqrt{2}}h\bar{d}d.\end{aligned}\tag{2.58}$$

The second terms in Eq. 2.58 represent the couplings between fermions and the Higgs field. The first terms give birth to the mass of fermions,  $m_\ell = \frac{y_\ell v}{\sqrt{2}}$  and  $m_d = \frac{y_d v}{\sqrt{2}}$ .

u-type quarks, on the other hand, have their masses in a slightly different way. For u-type quarks,  $(-Y_{q,L} + Y_\Phi + Y_{u,R}) = (-\frac{1}{3} + 1 + \frac{4}{3}) \neq 0$  so that a scalar doublet of hypercharge  $-1$  instead of  $1$  is required to form the gauge invariant Yukawa coupling terms. We can define such a doublet from the Higgs doublet:

$$\Phi_c = i\sigma_2 \Phi^*.\tag{2.59}$$

It transforms under  $SU(2)_L \times U(1)$  in the same way that the original Higgs  $\Phi$  does but has the opposite hypercharge,  $-1$ , leading to the desired relation  $(-Y_{q,L} + Y_{\Phi_c} + Y_{u,R}) = (-\frac{1}{3} - 1 + \frac{4}{3}) = 0$ . We can now see that the Yukawa coupling term with  $\Phi_c$  is invariant under  $SU(2)_L \times U(1)$ :

$$\begin{aligned}\bar{q}'_L \Phi'_c u'_R &= \bar{q}_L e^{-i(\frac{1}{2}Y_{q,L}\theta + \vec{\tau} \cdot \vec{\theta})} e^{i(-\frac{1}{2}Y_{\Phi}\theta + \vec{\tau} \cdot \vec{\theta})} \Phi_c e^{i\frac{1}{2}Y_{u,R}\theta} u_R \\ &= e^{i\frac{1}{2}(-Y_{q,L} - Y_{\Phi} + Y_{u,R})\theta} \bar{q}_L \Phi_c u_R = \bar{q}_L \Phi_c u_R.\end{aligned}\tag{2.60}$$

After spontaneous symmetry breaking,

$$\mathcal{L}_{Yukawa,u} = -\frac{y_u v}{\sqrt{2}}\bar{u}u - \frac{y_u}{\sqrt{2}}h\bar{u}u.\tag{2.61}$$

As a result, u-type quarks finally have  $m_u = \frac{y_u v}{\sqrt{2}}$ .

### 2.1.6 Flavor Physics

The flavors of fermions soon became of great interest after the introduction of the Yukawa coupling terms. In the early stages of the quark model, only 3

types of quarks (u, d, and s) were considered to account for observed mesons and baryons. Notwithstanding the success of the electroweak theory [56, 57], the non-detection of  $K^0 \rightarrow \mu^- \mu^+$  was a serious issue in the model. Among 3 types of quarks, the strange quark was once considered as a singlet for both chiralities. The Yukawa coupling terms of quarks were

$$\mathcal{L}_{Yukawa} = -y_u \bar{q}_L \Phi_c u_R - y_{11} \bar{q}_L \Phi d_R - y_{12} \bar{q}_L \Phi s_R - y_{21} \bar{s}_L \varphi d_R - y_{22} \bar{s}_L \varphi s_R, \quad (2.62)$$

where the quantum numbers of the strange quark and a newly introduced scalar singlet  $\varphi = \frac{1}{\sqrt{2}}(h(x) + v)$  are on Table 2.3. Note that the Yukawa

Table 2.3: Quantum numbers of the strange quark and the scalar singlet.

Particle	Hypercharge ( $Y$ )	Weak isospin ( $I_W$ )	Electric Charge ( $Q = I_W^3 + \frac{Y}{2}$ )
$s_{L,R}$	$-\frac{2}{3}$	0	$-\frac{1}{3}$
$\varphi$	0	0	0

coupling terms between different flavors are also introduced. They are allowed because of gauge invariance under  $SU(2) \times U(1)$ . After spontaneous symmetry breaking, the mass terms of quarks are derived as

$$\begin{aligned} \mathcal{L}_{mass} &= -\frac{y_u v}{\sqrt{2}} \bar{u}_L u_R - \frac{y_{11} v}{\sqrt{2}} \bar{d}_L d_R - \frac{y_{12} v}{\sqrt{2}} \bar{d}_L s_R - \frac{y_{21} v}{\sqrt{2}} \bar{s}_L d_R - \frac{y_{22} v}{\sqrt{2}} \bar{s}_L s_R \\ &= -\frac{y_u v}{\sqrt{2}} \bar{u}_L u_R - \frac{v}{\sqrt{2}} \begin{pmatrix} \bar{d}_L & \bar{s}_L \end{pmatrix} \begin{pmatrix} y_{11} & y_{12} \\ y_{21} & y_{22} \end{pmatrix} \begin{pmatrix} d_R \\ s_R \end{pmatrix}. \end{aligned} \quad (2.63)$$

It is clear that the flavor eigenstate of the u quark is identical to its mass eigenstate. The flavor eigenstates of d and s quarks, however, are different from their mass eigenstates. We need to diagonalize the mass matrix  $M_d$

$$M_d = \begin{pmatrix} y_{11} & y_{12} \\ y_{21} & y_{22} \end{pmatrix}, \quad (2.64)$$

The diagonalization can be done as

$$D_d = U_d M_d V_d^\dagger = \begin{pmatrix} m_1 & 0 \\ 0 & m_2 \end{pmatrix}. \quad (2.65)$$

with an arbitrary real unitary matrix  $U_d$ .  $U_d$  can be considered as a rotation between the flavor and the mass eigenstates of quarks. Then we can denote the relation between the flavor and the mass eigenstates by

$$\begin{pmatrix} d \\ s \end{pmatrix} = \begin{pmatrix} \cos\theta_C & \sin\theta_C \\ -\sin\theta_C & \cos\theta_C \end{pmatrix} \begin{pmatrix} d^0 \\ s^0 \end{pmatrix}, \quad (2.66)$$

with the mass eigenstates  $d^0$  and  $s^0$  and the mixing angle  $\theta_C$ , called the Cabibbo angle. We could check the impact of the mixing on electroweak charged and neutral currents

$$\begin{aligned} J_{charged}^\mu & : \quad \bar{u}_L \gamma^\mu d_L \\ J_{neutral}^\mu & : \quad \bar{u} \gamma^\mu u, \quad \bar{d} \gamma^\mu d. \end{aligned} \quad (2.67)$$

In the case of charged currents,

$$\bar{u}_L \gamma^\mu d_L = \cos\theta_C \bar{u}_L \gamma^\mu d_L^0 + \sin\theta_C \bar{u}_L \gamma^\mu s_L^0. \quad (2.68)$$

In the case of neutral currents,

$$\bar{u} \gamma^\mu u + \bar{d} \gamma^\mu d = \begin{pmatrix} \bar{u} & \bar{d}^0 & \bar{s}^0 \end{pmatrix} \begin{pmatrix} 1 & 0 & 0 \\ 0 & \cos\theta_C & \sin\theta_C \\ 0 & -\sin\theta_C & \cos\theta_C \end{pmatrix} \begin{pmatrix} u \\ d^0 \\ s^0 \end{pmatrix}, \quad (2.69)$$

which shows that the mixing has a similar amount of impact on the neutral currents. It clearly contradicts to the non-detection of the flavor changing neutral current (FCNC) decay channel of  $K^0$ ,  $K^0 \rightarrow \mu^- \mu^+$ .

The GIM mechanism [58] was proposed to solve this issue by introducing a new quark type named the charm (c) quark. The c quark couples to the s quark

through both weak charged and neutral currents. Due to the introduction of the  $c$  quark, the mixing effect is clearly canceled out for neutral currents:

$$\begin{aligned}
\bar{u}\gamma^\mu u + \bar{c}\gamma^\mu c \bar{d}\gamma^\mu d &= \bar{u}\gamma^\mu u + (\cos\theta_C \bar{d}^0 + \sin\theta_C \bar{s}^0)\gamma^\mu(\cos\theta_C d^0 + \sin\theta_C s^0) \\
&\quad + (-\sin\theta_C \bar{d}^0 + \cos\theta_C \bar{s}^0)\gamma^\mu(-\sin\theta_C d^0 + \cos\theta_C s^0) \\
&= \bar{u}\gamma^\mu u + \bar{c}\gamma^\mu c + \bar{d}^0\gamma^\mu d^0 + \bar{s}^0\gamma^\mu s^0,
\end{aligned} \tag{2.70}$$

i.e. the mixing has no impact on weak neutral currents. This is the clear reason for the non-detection of  $K^0 \rightarrow \mu^- \mu^+$ . It is also consistent with the modern observation

$$\frac{\text{K}_L^0 \rightarrow \mu^- \mu^+}{\text{K}_L^0 \rightarrow \pi^\pm \mu^\mp \bar{\nu}_\mu} = 0.25 \times 10^{-9}. \tag{2.71}$$

A small but non-zero contribution is produced not from the tree-level process discussed here but from  $W^\pm$  loop processes, shown in Fig. 2.1.

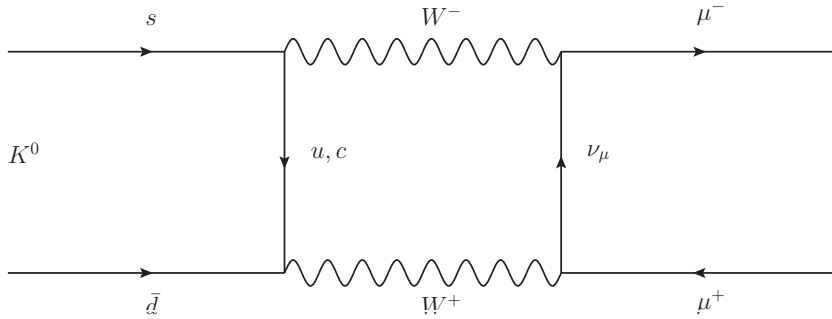


Figure 2.1: Loop diagrams of  $K^0 \rightarrow \mu^- \mu^+$  process.

The success of the GIM mechanism, however, was soon followed by an even larger problem; the detection of  $K_L^0 \rightarrow 2\pi$ , which is the first discovery of CP violation. Given the quantum numbers of  $K^0$   $J^{PC} = 0^{--}$ ,  $\hat{P}$  and  $\hat{C}$  operate on  $K^0$  as follows:

$$\hat{P}|K^0\rangle = -|K^0\rangle, \quad \hat{P}|\bar{K}^0\rangle = -|\bar{K}^0\rangle. \tag{2.72}$$

$$\hat{C}|K^0\rangle = -|\bar{K}^0\rangle, \quad \hat{C}|\bar{K}^0\rangle = -|K^0\rangle. \quad (2.73)$$

$$\hat{C}\hat{P}|K^0\rangle = |\bar{K}^0\rangle, \quad \hat{C}\hat{P}|\bar{K}^0\rangle = |K^0\rangle. \quad (2.74)$$

It clearly shows that  $|K^0\rangle$  and  $|\bar{K}^0\rangle$  are not CP eigenstates. The eigenstates of CP should be their superpositions

$$|K_S^0\rangle = \frac{|K^0\rangle + |\bar{K}^0\rangle}{\sqrt{2}}, \quad |K_L^0\rangle = \frac{|K^0\rangle - |\bar{K}^0\rangle}{\sqrt{2}}. \quad (2.75)$$

They transform under CP as follows:

$$\hat{C}\hat{P}|K_S^0\rangle = \frac{|K^0\rangle + |\bar{K}^0\rangle}{\sqrt{2}} = |K_S^0\rangle, \quad \hat{C}\hat{P}|K_L^0\rangle = \frac{-|K^0\rangle + |\bar{K}^0\rangle}{\sqrt{2}} = -|K_L^0\rangle, \quad (2.76)$$

showing that  $|K_S^0\rangle$  is CP even and  $|K_L^0\rangle$  is CP odd. However, if we check CP transformations on pions that have  $J^{PC} = 0^{-+}$ ,

$$\hat{C}|2\pi\rangle = |2\pi\rangle, \quad \hat{C}|3\pi\rangle = |3\pi\rangle. \quad (2.77)$$

$$\hat{P}|2\pi\rangle = |2\pi\rangle, \quad \hat{P}|3\pi\rangle = -|3\pi\rangle. \quad (2.78)$$

$$\hat{C}\hat{P}|2\pi\rangle = |2\pi\rangle, \quad \hat{C}\hat{P}|3\pi\rangle = -|3\pi\rangle. \quad (2.79)$$

It proves that  $K_L^0 \rightarrow 2\pi$  is forbidden if CP is conserved. Therefore, the discovery of this process is considered as the proof of the violation of CP symmetry, which was long believed to be an exact symmetry of physics laws.

To account for CP violation, Kobayashi and Maskawa proposed a new generation of quarks, top (t) and bottom (b). The key point of their idea lies in imaginary phases that are allowed in the mixing matrix if the dimension of the matrix is equal to or larger than 3. Their prediction on new quarks has been proven by the discovery of the first bottomium states in 1977 and the discovery of the top quark in 1995. With 6 quarks of 3 generations, we have

the mass terms of quarks as follows:

$$\begin{aligned} \mathcal{L}_{mass} = & -\frac{v}{\sqrt{2}} \begin{pmatrix} \bar{u}_L & \bar{c}_L & \bar{t}_L \end{pmatrix} \begin{pmatrix} h_{11} & h_{12} & h_{13} \\ h_{21} & h_{22} & h_{23} \\ h_{31} & h_{32} & h_{33} \end{pmatrix} \begin{pmatrix} u_R \\ c_R \\ t_R \end{pmatrix} \\ & -\frac{v}{\sqrt{2}} \begin{pmatrix} \bar{d}_L & \bar{s}_L & \bar{b}_L \end{pmatrix} \begin{pmatrix} g_{11} & g_{12} & g_{13} \\ g_{21} & g_{22} & g_{23} \\ g_{31} & g_{32} & g_{33} \end{pmatrix} \begin{pmatrix} d_R \\ s_R \\ b_R \end{pmatrix}, \end{aligned} \quad (2.80)$$

with the mass matrices

$$M_u = \frac{v}{\sqrt{2}} \begin{pmatrix} h_{11} & h_{12} & h_{13} \\ h_{21} & h_{22} & h_{23} \\ h_{31} & h_{32} & h_{33} \end{pmatrix}, \quad M_d = \frac{v}{\sqrt{2}} \begin{pmatrix} g_{11} & g_{12} & g_{13} \\ g_{21} & g_{22} & g_{23} \\ g_{31} & g_{32} & g_{33} \end{pmatrix}. \quad (2.81)$$

They can also be diagonalized:

$$D_u = U_u M_u V_u^\dagger = \begin{pmatrix} m_u & 0 & 0 \\ 0 & m_c & 0 \\ 0 & 0 & m_t \end{pmatrix}, \quad D_d = U_d M_d V_d^\dagger = \begin{pmatrix} m_d & 0 & 0 \\ 0 & m_s & 0 \\ 0 & 0 & m_b \end{pmatrix}. \quad (2.82)$$

Thus, the mass eigenstates are given by

$$\begin{aligned} q_{u,L}^0 &= U_u q_{d,L}, & q_{u,R}^0 &= V_u q_{d,R}, & q_{d,L}^0 &= U_d q_{d,L}, & q_{d,R}^0 &= V_d q_{d,R} \\ \bar{q}_{u,L}^0 &= \bar{q}_{d,L} U_u^\dagger, & \bar{q}_{u,R}^0 &= \bar{q}_{d,R} V_u^\dagger, & \bar{q}_{d,L}^0 &= \bar{q}_{d,L} U_d^\dagger, & \bar{q}_{d,R}^0 &= \bar{q}_{d,R} V_d^\dagger. \end{aligned} \quad (2.83)$$

We can easily see that the neutral currents are diagonalized also for the case of 6 quarks. The charge currents, on the other hand, still have the mixing between different flavors:

$$\bar{q}_{uL} \gamma^\mu q_{dL} = \bar{q}_{uL}^0 U_u \gamma^\mu U_d^\dagger q_{dL}^0 = \bar{q}_{uL}^0 \gamma^\mu (U_u U_d^\dagger) q_{dL}^0. \quad (2.84)$$

All the flavor mixing information in the quark sector is contained in  $U_u U_d^\dagger$ . This unitary matrix is called the Cabbibo-Kobayashi-Maskawa (CKM) matrix,  $U_{CKM} = U_u U_d^\dagger$ .

### 2.1.7 Quantum Chromodynamics

Finally it is time to discuss the dynamics of quarks and gluons, named the quantum chromodynamics (QCD). The fundamental symmetry of QCD belongs to the special unitary group of degree 3,  $SU(3)$ . The fundamental representation of  $SU(3)$  is a triplet, i.e., QCD have 3 conserved charges. The charges are named the color charges, each denoted by red (R), green (G), and blue (B). In addition,  $SU(3)$  has  $3^2 - 1 = 8$  generators, each corresponding to a gluon state. Therefore, the quarks are color triplets whereas the gluon is a color octet. We can construct the gauge-invariant QCD Lagrangian in the same way as for the electroweak Lagrangian:

$$\mathcal{L} = \sum_q \bar{\psi}_{q,a} (i\gamma^\mu \partial_\mu \delta_{ab} - g_s \gamma^\mu t_{ab}^c A_\mu^c - m_q \delta_{ab}) \psi_{q,b} - \frac{1}{4} F_{\mu\nu}^A F^{A\mu\nu}, \quad (2.85)$$

where

- $\psi_{q,a}$  is the quark of flavor  $q$  and color charge “ $a$ ”. “ $a$ ” runs from 1 to  $N_C = 3$ , where  $N_C$  is the number of colors.
- $A_\mu^c$  is the gauge field of QCD, gluon.  $c$  runs from 1 to  $N_C^2 - 1 = 8$ .
- $t_{ab}^c$  are the 8 generators of  $SU(3)$ .
- $g_s$  denotes the coupling strength of QCD.  $\alpha_s = \frac{g_s^2}{4\pi}$ .
- $F_{\mu\nu}^A = \partial_\mu A_\nu^A - \partial_\nu A_\mu^A - g_s f_{ABC} A_\mu^B A_\nu^C$ .
- $f_{ABC}$  is the structure constant of the  $SU(3)$  group defined from  $[t^A, t^B] = i f_{ABC} t^C$ .

Now we are ready to derive the most distinctive property of QCD from its coupling constant. From the renormalization procedure, we can derive the

running coupling constant of QCD

$$\alpha_S(Q^2) = \frac{\alpha_S(\mu^2)}{1 + \frac{\alpha_S(\mu^2)}{12\pi}(33 - 2n_f)\log(Q^2/\mu^2)} \quad (2.86)$$

where  $n_f$  is the number of quark flavors. Since  $n_f = 6$  in the real world, the sign of the QCD coupling constant is the opposite of the QED coupling constant. This makes a huge difference in their behaviors. We can remove  $\mu$  by define a scale  $\Lambda$  by

$$\Lambda^2 = \mu^2 \exp\left(\frac{-12\pi}{(33 - 2n_f)\alpha_S(\mu^2)}\right) \quad (2.87)$$

and insert it into Eq. 2.86:

$$\alpha_S(Q^2) = \frac{12\pi}{33 - 2n_f} \log(Q^2/\Lambda^2) \quad (2.88)$$

For  $Q^2 \gg \Lambda^2$ , the coupling becomes small and a perturbative picture with asymptotically free quarks and weakly interacting gluons makes sense. This property is called asymptotic freedom. For  $Q^2 \sim O(\Lambda^2)$ , on the other hand, quarks and gluons interact so strongly that quarks must be confined in color singlet bound states, hadrons. The perturbative QCD does not work at all at this much low energy scale. Thus,  $\Lambda$ , called the QCD scale, can be considered as a critical transition point between the world of asymptotic freedom and the world of confinement.

Finally, we have a complete theory of the SM based on the local  $SU(3) \times SU(2)_L \times U(1)_Y$  gauge symmetry. All the elementary particles discussed in this section are summarized in Table 2.4.

## 2.2 Physics Beyond the Standard Model

Various BSM theories predict new physics signatures that can be prevalent in  $\ell\ell\gamma$  final states. In this section, several such models are introduced. New scalar

Table 2.4: Elementary particles of the SM

Fermions			Bosons	
1st	2nd	3rd	Gauge	Scalar
$q_L = \begin{pmatrix} u_L \\ d_L \end{pmatrix}$	$q_L = \begin{pmatrix} c_L \\ s_L \end{pmatrix}$	$q_L = \begin{pmatrix} t_L \\ b_L \end{pmatrix}$	g	H
$u_R, d_R$	$c_R, s_R$	$t_R, b_R$	$\gamma$	
$\ell_L = \begin{pmatrix} \nu_{eL} \\ e_L \end{pmatrix}$	$\ell_L = \begin{pmatrix} \nu_{\mu L} \\ \mu_L \end{pmatrix}$	$\ell_L = \begin{pmatrix} \nu_{\tau L} \\ \tau_L \end{pmatrix}$	Z	
$e_R$	$\mu_R$	$\tau_R$	$W^-, W^+$	

resonances predicted by composite Higgs models and models with an extended Higgs sector are possible sources of  $Z\gamma$  resonances. Compositeness models, an attempt to explain the generations of fermions and their mass hierarchy, give birth to the excited states of fermions.

### 2.2.1 Extended Higgs Sector

Although the discovery of the Higgs boson is largely considered as the completion of the SM, the Higgs itself brings the SM into question. The SM cannot explain the lightness of the Higgs boson mass, which is unnatural leading to the hierarchy problem, and also does not predict the unification of gauge couplings. Physicists have proposed various extensions of the SM to solve those problems. An extension of the Higgs sector in particular is popularly adopted to include additional Higgs doublets or even other representations such as singlets and triplets. In this section, one of the simplest extensions of the Higgs sector is addressed; the two-Higgs-doublet models (2HDMs).

In general, 2HDMs have a very rich vacuum structure. The scalar potential in its most general form can contain 14 parameters and have various

types of minima including CP-conserving, CP-violating, and charge-violating ones. However, several assumptions for simplicity are usually made on phenomenological studies of 2HDMs. CP conservation in the Higgs sector is widely assumed, so as to distinguish between scalars and pseudoscalars, and CP symmetry is not spontaneously broken. All quartic terms that is odd in either of the doublets are eliminated from the scalar potential by discrete symmetries, with the usual exception of the terms that breaks the symmetries softly. Under these assumptions, the most general form of the scalar potential for two doublets  $\Phi_1$  and  $\Phi_2$  with hypercharge +1 is given by

$$\begin{aligned}
V = & m_{11}^2 \Phi_1^\dagger \Phi_1 + m_{22}^2 \Phi_2^\dagger \Phi_2 - m_{12}^2 (\Phi_1^\dagger \Phi_2 + \Phi_2^\dagger \Phi_1) + \frac{\Lambda_1}{2} (\Phi_1^\dagger \Phi_1)^2 + \frac{\Lambda_2}{2} (\Phi_2^\dagger \Phi_2)^2 \\
& + \Lambda_3 \Phi_1^\dagger \Phi_1 \Phi_2^\dagger \Phi_2 + \Lambda_4 \Phi_1^\dagger \Phi_2 \Phi_2^\dagger \Phi_1 + \frac{\Lambda_5}{2} [(\Phi_1^\dagger \Phi_1)^2 + (\Phi_2^\dagger \Phi_2)^2],
\end{aligned} \tag{2.89}$$

where all the parameters are real. The minimum of this potential can be chosen at

$$\langle \Phi_1 \rangle_0 = \begin{pmatrix} 0 \\ \frac{v_1}{\sqrt{2}} \end{pmatrix}, \quad \langle \Phi_2 \rangle_0 = \begin{pmatrix} 0 \\ \frac{v_2}{\sqrt{2}} \end{pmatrix}. \tag{2.90}$$

Given two complex scalar  $SU(2)$  doublets, there are eight fields

$$\Phi_a = \begin{pmatrix} \phi_a^+ \\ (v_a + \rho_a + i\eta_a)/\sqrt{2} \end{pmatrix}. \tag{2.91}$$

Three of those get absorbed to generate the masses of the weak gauge bosons  $W^\mp$  and  $Z$ , and the rest give rise to physical scalar fields (Higgs): opposite-sign charged scalars, two neutral scalars, and one pseudoscalar. The charged scalars have the following mass terms:

$$\mathcal{L}_{\phi^\pm \text{ mass}} = [(m_{12}^2) - (\Lambda_4 + \Lambda_5)v_1v_2] \begin{pmatrix} \phi_1^- & \phi_2^- \end{pmatrix} \begin{pmatrix} \frac{v_2}{v_1} & -1 \\ -1 & \frac{v_1}{v_2} \end{pmatrix} \begin{pmatrix} \phi_1^+ \\ \phi_2^+ \end{pmatrix}. \tag{2.92}$$

One of the two eigenvalues is found to be zero, which corresponds to the charged Goldstone boson  $G^\pm$  that are consumed by the  $W^\pm$ . The other one

yields the mass of the charged Higgs,  $m_+^2 = [m_{12}^2/v_1v_2 - \Lambda_4 - \Lambda_5](v_1^2 + v_2^2)$ .

The pseudoscalars have the following mass terms:

$$\mathcal{L}_{\eta \text{ mass}} = \frac{m_A^2}{v_1^2 + v_2^2} (\eta_1, \eta_2) \begin{pmatrix} v_2^2 & -v_1v_2 \\ -v_1v_2 & v_1^2 \end{pmatrix} \begin{pmatrix} \eta_1 \\ \eta_2 \end{pmatrix}. \quad (2.93)$$

Those mass terms provide a pseudoscalar Goldstone mode and the mass of the physical pseudoscalar,  $m_A^2 = [m_{12}^2/(v_1v_2) - 2\Lambda_5](v_1^2 + v_2^2)$ . It is worth pointing out that the pseudoscalar becomes massless when  $m_{12}^2 = \Lambda_5 = 0$ , This is because of an additional global  $U(1)$  symmetry which exists in that limit and is spontaneously broken. The mass terms of the scalars are given as follows:

$$\mathcal{L}_{\rho \text{ mass}} = - (\rho_1, \rho_2) \begin{pmatrix} m_{12}^2 \frac{v_2}{v_1} + \Lambda_1 v_1^2 & -m_{12}^2 + \Lambda_{345} v_1 v_2 \\ -m_{12}^2 + \Lambda_{345} v_1 v_2 & m_{12}^2 \frac{v_1}{v_2} + \Lambda_2 v_2^2 \end{pmatrix} \begin{pmatrix} \rho_1 \\ \rho_2 \end{pmatrix}, \quad (2.94)$$

with  $\Lambda_{345} = \Lambda_3 + \Lambda_4 + \Lambda_5$ . The mass-squared matrix of the scalars can be diagonalized and the angle  $\alpha$  is defined to be the rotation angle for that diagonalization.

Similarly,  $\beta$  is defined to be the rotation angle for the diagonalization of the mass-squared matrices of the charged scalars and of the pseudoscalars,

$$\tan \beta \equiv \frac{v_2}{v_1}. \quad (2.95)$$

Given  $\beta$ , the doublets can be rewritten as  $H_1 = \cos \beta \Phi_1 + \sin \beta \Phi_2$  and  $H_2 = -\sin \beta \Phi_1 + \cos \beta \Phi_2$ . Note that the second component of  $H_1$  has a real positive VEV  $v/\sqrt{2}$ , with  $v \equiv (v_1^2 + v_2^2)^{1/2}$ , whereas  $H_2$  has a null VEV. The interactions of the various Higgs field with both the gauge bosons and the fermions are determined by those two angles  $\alpha$  and  $\beta$ . Thus, they are essential in phenomenological studies of 2HDMs.

### 2.2.2 Composite Higgs Models

As already pointed out, the SM fails to explain the lightness of the Higgs boson and the dynamical origin of electroweak symmetry breaking. Another approach to solve these puzzles is to consider the Higgs boson as a bound state of new dynamics that acts strongly at the electroweak scale. In this section, one of such composite Higgs models is described; the little Higgs models.

The little Higgs models identify the Higgs doublet as a pseudo Nambu–Goldstone boson while keeping non-derivative interactions to some extent, especially a large quartic interaction of Higgs. As with pions that function as Nambu–Goldstone bosons in the chiral symmetry breaking  $SU(2)_L \times SU(2)_R / SU(2)$ , massive Nambu–Goldstone bosons can exist if there are interactions that manifestly break the global symmetry. The mass of the Nambu–Goldstone bosons is of the order of  $g\Lambda_{G/H}/(4\pi)$ , where  $g$  denotes the coupling of the symmetry breaking interaction and  $\Lambda_{G/H} = 4\pi f_{G/H}$  represents the dynamical scale of the global symmetry breaking  $G/H$ . For the Higgs boson mass, the global symmetry can be broken by either the Yukawa interactions or the gauge interactions, which work nonlinearly on the Higgs boson. In order to have a 125 GeV Higgs boson mass, however,  $\Lambda_{G/H}$  should be of the order of 1 TeV, requiring too large corrections. The dynamic scale can have a larger, plausible value if the mass is generated at the two-loop level:

$$m_H^2 = \frac{g^2}{16\pi^2} \Lambda_{G/H}^2 \rightarrow m_H^2 = \frac{g_1^2 g_2^2}{(16\pi^2)^2} \Lambda_{G/H}^2. \quad (2.96)$$

This condition is implemented via the concept of collective symmetry breaking:

$$\mathcal{L} = \mathcal{L}_{G/H} + g_1 \mathcal{L}_1 + g_2 \mathcal{L}_2 \quad (2.97)$$

The interactions 1 and 2 preserve different subgroups of the global symmetry so that the Higgs boson acts as an exact Nambu–Goldstone boson in the absence of either  $g_1$  or  $g_2$ . Only diagrams associated with both interactions, which

first appear at the two-loop level, can contribute to the Higgs boson mass. The SM quadratic divergences can be manifestly canceled out by the presence of new Fermi-scale particles including gauge bosons, vector-like quarks and extra massive scalars. They have the SM partners (related by the original global symmetry) with the same spin, contrary to supersymmetry where superpartners have spins which differ by a half-integer. These new particles that have couplings with SM particles, governed by the global symmetry, can be probed at the LHC.

Among diverse variations of the collective symmetry breaking mechanism, the littlest Higgs model is the smallest one that is based on an  $SU(5)/SO(5)$  nonlinear  $\sigma$  model. This model incorporates a weakly gauged subgroup of  $SU(2)_1 \times U(1)_1 \times SU(2)_2 \times U(1)_2$ . There are a single electroweak doublet, which is manifestly lighter than the other Nambu–Goldstone bosons and identified with the Higgs doublet, and an additional scalar triplet at the TeV scale. There are also other popular models based on different coset spaces: minimal moose ( $SU(3)^2/SU(3)$ ), the simplest little Higgs ( $SU(3)^2/SU(2)^2$ ), the bestest little Higgs ( $SO(6)^2/SO(6)$ ).

### 2.2.3 Compositeness and Excited Leptons

The fermion mass hierarchy is one of fundamental questions unanswered by the SM to date. Compositeness models are an attempt to answer this question by proposing a composite nature of the fermions. In compositeness models, the fundamental constituents of fermions, so called preons, are bound by a new strong interaction that is described by the compositeness scale  $\Lambda$ . Each SM fermion is identified with the ground state of its flavor, and these bound states can be excited to higher-mass states. The excited states of leptons, called excited leptons, are considered in this thesis.

An excited lepton is phenomenologically defined as a heavy lepton which shares the same leptonic quantum numbers with the corresponding ground-state lepton. Given constraints from the lepton masses and  $g-2$  measurements, an excited lepton is expected to couple with not both left- and right-handed components of the corresponding lepton. Examples of possible excited lepton classification based on  $SU(2) \times U(1)$  are as follows:

- Sequential type:

$$\begin{pmatrix} \nu^* \\ \ell^* \end{pmatrix}_L, \quad \begin{pmatrix} \nu_R^* \end{pmatrix}, \quad \ell_R^*$$

- Mirror type:

$$\ell_L^*, \quad \begin{pmatrix} \nu_L^* \end{pmatrix}, \quad \begin{pmatrix} \nu^* \\ \ell^* \end{pmatrix}_R$$

- Homodoublet type:

$$\begin{pmatrix} \nu^* \\ \ell^* \end{pmatrix}_L, \quad \begin{pmatrix} \nu^* \\ \ell^* \end{pmatrix}_R$$

Excited leptons can be pair produced via their minimal gauge couplings. For example, the couplings of excited leptons with  $Z$  are given by:

$$\begin{aligned} & \frac{e}{2 \sin \theta_W \cos \theta_W} (-1 + 2 \sin^2 \theta_W) \bar{\ell}^* \gamma^\mu \ell^* Z_\mu \\ & + \frac{e}{2 \sin \theta_W \cos \theta_W} \bar{\nu}^* \gamma^\mu \nu^* Z_\mu \end{aligned} \quad (2.98)$$

Another production possibility is via the contact interactions with ordinary quarks and leptons:

$$\begin{aligned} \mathcal{L}_{CI} = & \frac{g_*^2}{\Lambda^2} [\eta'_{LL} (\bar{\psi}_L \gamma_\mu \psi_L) (\bar{\psi}_L^* \gamma^\mu \psi_L^*) \\ & + (\eta''_{LL} (\bar{\psi}_L \gamma_\mu \psi_L) (\bar{\psi}_L^* \gamma^\mu \psi_L) + \text{h.c.}) + \dots], \end{aligned} \quad (2.99)$$

with  $g_*^2 = 4\pi$ . For simplicity, it is widely assumed that  $\eta'_{LL} = \eta''_{LL} = 1$  and  $\eta'_{LR} = \eta'_{RL} = \eta'_{RR} = \eta''_{LR} = \eta''_{RL} = \eta''_{RR} = 0$ . In addition, a gauge-mediated transition between left-handed leptons and right-handed excited leptons and vice versa are also possible. The corresponding couplings can be parametrized as follows:

$$\begin{aligned}
\mathcal{L} = & \frac{\lambda_\gamma^{(\psi^*)} e}{2m_{\psi^*}} \bar{\psi}^* \sigma^{\mu\nu} \left( \eta_L \frac{1 - \gamma_5}{2} + \eta_R \frac{1 + \gamma_5}{2} \right) \psi F_{\mu\nu} \\
& + \frac{\lambda_Z^{(\psi^*)} e}{2m_{\psi^*}} \bar{\psi}^* \sigma^{\mu\nu} \left( \eta_L \frac{1 - \gamma_5}{2} + \eta_R \frac{1 + \gamma_5}{2} \right) \psi Z_{\mu\nu} \\
& + \frac{\lambda_W^{(\ell^*)} g}{2m_{\ell^*}} \bar{\ell}^* \sigma^{\mu\nu} \frac{1 - \gamma_5}{2} \nu W_{\mu\nu} \\
& + \frac{\lambda_W^{(\nu^*)} g}{2m_{\nu^*}} \bar{\nu}^* \sigma^{\mu\nu} \left( \eta_L \frac{1 - \gamma_5}{2} + \eta_R \frac{1 + \gamma_5}{2} \right) \ell W_{\mu\nu}^\dagger \\
& + \text{h.c.},
\end{aligned} \tag{2.100}$$

where  $g = e/\sin\theta_W$ ,  $\psi = \nu$  or  $\ell$ ,  $F_{\mu\nu} = \partial_\mu A_\nu - \partial_\nu A_\mu$  is the photon field strength,  $Z_{\mu\nu} = \partial_\mu Z_\nu - \partial_\nu Z_\mu$ , etc. The normalization of the coupling is selected by the following:

$$\max(|\eta_L|, |\eta_R|) = 1. \tag{2.101}$$

Chirality conservation also requires:

$$\eta_L \eta_R = 0. \tag{2.102}$$

The couplings in Eq. 2.100 can originate from higher-dimensional interactions of  $SU(2) \times U(1)$ . In particular, the interaction of homodoublet type  $\ell^*$  can be described by the Lagrangian:

$$\mathcal{L}_{\text{gauge}} = \frac{1}{2\Lambda} \bar{L}^* \sigma^{\mu\nu} \left( g f \frac{\tau^a}{2} W_{\mu\nu}^a + g' f' Y B_{\mu\nu} \right) \frac{1 - \gamma_5}{2} L + \text{h.c.}, \tag{2.103}$$

where  $\Lambda$  is the compositeness scale,  $L$  denotes the lepton doublet  $(\nu, \ell)$ , and  $W_{\mu\nu}$  and  $B_{\mu\nu}$  are the field strengths for  $SU(2)$  and  $U(1)_Y$  gauge fields. The

quantities  $g = e/\sin\theta_W$  and  $g' = e/\cos\theta_W$  represent the corresponding electroweak gauge couplings with the Weinberg mixing angle  $\theta_W$ , and  $\tau$  and  $Y$  are the generators of the  $SU(2)$  and  $U(1)_Y$  groups. These couplings satisfy the relation:

$$\lambda_W = -\sqrt{2}\sin\theta_W^2(\lambda_Z \cot\theta_W + \lambda_\gamma), \quad (2.104)$$

with  $\lambda_{W,Z,\gamma}$  being defined in Eq. 2.100 with  $\lambda_{W,Z,\gamma} = \lambda_{W,Z,\gamma}^{(\ell^*)}$  or  $\lambda_{W,Z,\gamma} = \lambda_{W,Z,\gamma}^{(\nu^*)}$ , with the assumption  $(\eta_L, \eta_R) = (1, 0)$ .

The excited lepton production in collider experiments is available either through SM gauge couplings or through CI. The pair production via the gauge boson couplings is dominant for small  $m_{\ell^*}/\Lambda$  ratios. This production mode can provide  $\Lambda$ -independent exclusion limits on  $m_{\ell^*}$ . For large  $m_{\ell^*}/\Lambda$  ratios that are accessible at the LHC, the production mode via the substantially strong coupling  $g_*$  of CI compared to the electroweak gauge couplings turns on and yields non-negligible cross sections for the production of excited leptons, which may be large enough for its discovery. Thus, the production mode through CI is mainly considered in excited lepton searches at the LHC.

Starting from the Lagrangian of CI in Eq. 2.99, the partonic cross section for the production of a single excited lepton in association with a ground-state lepton can be derived as:

$$\sigma(q\bar{q} \rightarrow \ell\ell^*) = \frac{\pi}{6\hat{s}} \left(\frac{\hat{s}}{\Lambda^2}\right)^2 \left(1 + \frac{\nu}{3}\right) \times \left(1 - \frac{m_{\ell^*}^2}{\hat{s}}\right)^2 \left(1 + \frac{m_{\ell^*}^2}{\hat{s}}\right). \quad (2.105)$$

Similarly, the cross section for the pair-production mode is given by:

$$\sigma(q\bar{q} \rightarrow \ell^*\ell^*) = \frac{\pi\tilde{\nu}}{12\hat{s}} \left(\frac{\hat{s}}{\Lambda^2}\right)^2 \left(1 + \frac{\tilde{\nu}^2}{3}\right). \quad (2.106)$$

The cross sections depend on  $m_{\ell^*}$ ,  $\Lambda$ , and the center-of-mass energy of the

parton-parton system  $\sqrt{\hat{s}} = x_1 \cdot x_2 \cdot \sqrt{s}$ . The symbols  $\nu$  and  $\tilde{\nu}$  are defined as:

$$\begin{aligned}\nu &= \frac{\hat{s} - m_{\ell^*}^2}{\hat{s} + m_{\ell^*}^2} \\ \tilde{\nu} &= \sqrt{1 - 4 \frac{m_{\ell^*}^2}{\hat{s}}}\end{aligned}\tag{2.107}$$

In pp collisions, the average parton-parton collision energy is in general significantly lower than the center-of-mass energy of the colliding pp (13 TeV for the LHC Run 2 operation). The cross section for the pair-production mode is, as expressed in Eq. 2.106, additionally suppressed compared to the cross section for single-production mode. Therefore, only the single-production mode is usually considered in excited lepton searches at the LHC.

Excited leptons, higher-mass states of SM leptons, must decay to their ground states with light SM particles. Like its production, the decay of excited leptons can be governed either by SM gauge interactions or by CI. The decay mode via photon emission has the following decay width:

$$\Gamma(\ell^* \rightarrow \ell\gamma) = \frac{1}{4} \alpha f_\gamma^2 \frac{m_{\ell^*}^3}{\Lambda^2}.\tag{2.108}$$

In the case of the weak gauge boson radiation mode, the partial width is given by:

$$\Gamma(\ell^* \rightarrow \ell V) = \frac{1}{8} \frac{g_V^2}{4\pi} f_V^2 \frac{m_{\ell^*}^3}{\Lambda^2} \left(1 - \frac{m_V^2}{m_{\ell^*}^2}\right)^2 \left(2 + \frac{m_V^2}{m_{\ell^*}^2}\right).\tag{2.109}$$

The symbol  $m_V$  denotes the mass of the W or the Z boson, and  $g_V$  is defined as either  $g_W = e/\sin\theta_W$  or  $g_Z = g_W/\cos\theta_W$ . The couplings,  $f_V$ , are given by:

$$\begin{aligned}f_\gamma &= fT_3 + f' \frac{Y}{2} \\ f_Z &= fT_3 \cos\theta_W^2 - f' \frac{Y}{2} \sin\theta_W^2 \\ f_W &= \frac{f}{\sqrt{2}}\end{aligned}\tag{2.110}$$

with the same leptonic quantum numbers,  $T_3 = -1/2$  and  $Y = -1$ . The parameters  $f$  and  $f'$  directly regulate the couplings to the gauge bosons. For

example, the coupling of excited leptons to the photon becomes largest in the case  $f = f' = 1$ , thus maximizing its branching fraction. If  $f = -f' = 1$ , on the contrary, the decay under the photon radiation is forbidden as the corresponding coupling becomes zero. The partial width of the decay via the 4-fermion CI is described as:

$$\Gamma(\ell^* \rightarrow \ell f f) = \frac{m_{\ell^*}}{96\pi} \left(\frac{m_{\ell^*}}{\Lambda}\right)^4 N_C S \quad (2.111)$$

with a color factor for the final state fermions  $f$ , being  $N_C = 1$  or  $3$  for leptons and quarks, respectively.  $S$  is an additional combinatorial factor:

$$\begin{aligned} S &= 1, & \text{if } f \neq \ell \\ S &= 2, & \text{if } f = \ell \end{aligned} \quad (2.112)$$

The branching fraction of each decay mode can be obtained from the formulae above, as a function of the ratio  $m_{\ell^*}/\Lambda$ . The branching fractions for two cases,  $f = f' = 1$  (left) and  $f = -f' = 1$  (right), are shown in Fig. 2.2. For  $f = f' = 1$ , the decay involved with the W boson (pink, dashed-dotted) is the most dominant among the gauge-boson-mediated modes. The decay under the photon radiation (black, short dashed) is subdominant, followed by the Z boson radiation mode (red, long dashed). On the contrary, the photon contribution vanishes if  $f = -f' = 1$ , and the Z-radiated mode gains substantially instead. The decay mode via CI (blue, solid), however, strongly dominates over the other modes at large  $m_{\ell^*}/\Lambda$  values in both cases.

The perturbative constraint  $m_{\ell^*} < \Lambda$  is conventionally imposed on the accessible parameter space in both phenomenological studies and experimental analyses for excited leptons. Another important constraint for quantum theories, the unitarity bound from the optical theorem, has been recently derived for excited lepton studies [59]. The large portion of the parameter space with large  $m_{\ell^*}/\Lambda$ , that once survived from the perturbative constraint, turns out

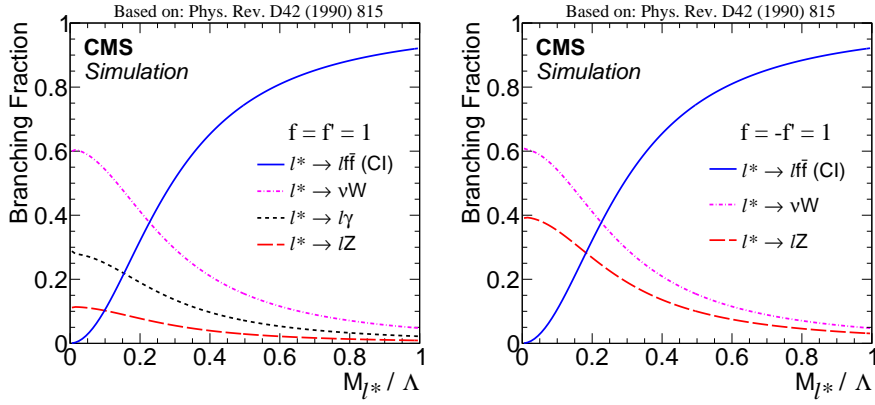


Figure 2.2: Branching fractions of the various decay modes as a function of  $m_{\ell^*}/\Lambda$  [36].

to be excluded by the unitarity bound. As a result, the experimental sensitivity of the CI channel in the large- $m_{\ell^*}/\Lambda$  region is significantly restricted and becomes comparable to the  $ll\gamma$  channel one. Given the unitarity bound, the  $ll\gamma$  channel is expected to be the major driving force behind excluding the parameter space.

## Chapter 3

# Experimental Setup

### 3.1 The Large Hadron Collider

The LHC is the largest and the most powerful hadron collider in the world, designed to collide proton beams at a center-of-mass energy of 14 TeV. The LHC is contained in a long circular tunnel with a circumference of 26.7 km, which was originally built to house the LEP collider. Two parallel proton beam lines are kept in orbits in opposite directions by the magnetic field. The beams are driven by the 1232 dipole magnets generating a magnetic field of 8.3 T with an electric current of about 11 kA. The stability of the beam dynamics is guaranteed by 474 quadrupole magnets that squeeze proton bunches in the beams. There are also special sets of quadrupoles so called inner triplet magnets. The inner triplets are installed at the interaction points in order to focus the beams for collisions. These Nb-Ti superconducting magnets operate at 1.9 K, being cooled down by superfluid He-4.

The LHC is supplied with protons from the injector chain of several smaller

particle accelerators, schematically illustrated in Fig. 3.1. Protons are produced in Linear accelerator 2 by stripping off electrons from hydrogen gas by applying an electric field and are accelerated to 50 MeV. These protons are sequentially accelerated in a series of accelerators; to 1.4 GeV in the Proton Synchrotron Booster, to 25 GeV in the Proton Synchrotron, and to 450 GeV by the Super Proton Synchrotron. At the end, the proton beams are finally injected to the two LHC beam pipes. The beams are accelerated and shaped into proton bunches, using radio-frequency cavities operated at 400 MHz. Once protons reach the nominal energy and the beams are stabilized, protons are brought to collide in the interaction points (IP) along the LHC ring.

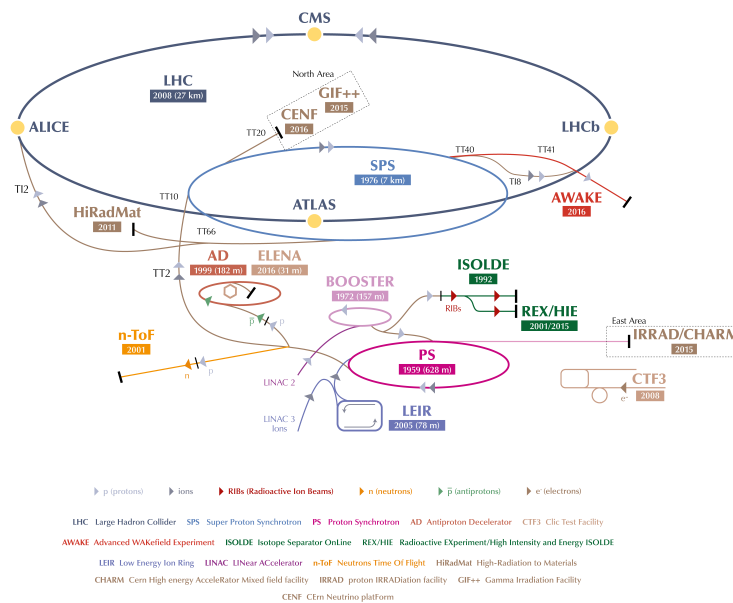


Figure 3.1: Representation of the CERN accelerator complex.

The instantaneous luminosity  $\mathcal{L}$  of the collisions is an important parameter

of the LHC machine, which is determined by the beam properties as:

$$\mathcal{L} = \frac{N_b^2 n_b f_{rev} \gamma_r}{4\pi \epsilon_n \beta^*} F. \quad (3.1)$$

$N_b$  and  $n_b$  are the number of protons per bunch and the number of bunches per beam, respectively. The symbols  $f_{rev}$  and  $\gamma_r$  denote the revolution frequency and the Lorentz factor of protons in the beam, respectively.  $\epsilon_n$  is the transverse emittance of the beam and  $\beta^*$  is the amplitude function value at IP. The factor  $F$  describes the geometric reduction of the instantaneous luminosity. It is a function of the beam crossing angle  $\theta_c$  and the transverse and longitudinal r.m.s. bunch sizes  $\sigma_{xy}$  and  $\sigma_z$  at IP:

$$F = \left(1 + \frac{\theta_c \sigma_z}{2\sigma_{xy}}\right)^{-\frac{1}{2}} \quad (3.2)$$

The nominal values of the parameters are summarized in Table 3.1.

Table 3.1: Nominal parameters of the LHC machine in pp collisions.

$\sqrt{s}$	center-of-mass energy	14 TeV
$\Delta t_b$	bunch spacing	25 ns
$N_b$	particles per bunch	$1.15 \times 10^{11}$
$n_b$	bunches per beam	2808
$f_{rev}$	revolution frequency	11.2 kHz
$\epsilon_n$	transverse beam emittance	$3.75 \mu\text{m}$
$\beta^*$	beta function	0.55 m
$\theta_c$	crossing angle at IP	$285 \mu\text{rad}$
$\sigma_{xy}$	transverse r.m.s. bunch size at IP	$16.7 \mu\text{m}$
$\sigma_z$	longitudinal r.m.s. bunch size	7.55 cm

The total amount of collisions produced is measured in terms of the integrated luminosity  $L = \int \mathcal{L} dt$ . LHC downtimes must be taken into account

upon performing the integration, and correspond to the time needed for maintenance, filling, and ramping of the magnetic field. In 2016, the LHC achieved a record-breaking performance of colliding protons for about 70% of the time dedicated to operations; machine commissioning and winter shutdown are clearly not taken into account. The luminosity constitutes the coefficient of proportionality between the number of events  $N$  produced for a specific process and its cross section  $\sigma$ :

$$N = L \times \sigma \tag{3.3}$$

The four IPs of the LHC are instrumented with particle detectors installed in underground caverns. “A Toroidal LHC ApparatuS” (ATLAS) and the “Compact Muon Solenoid” (CMS) experiments are installed in the diametrically opposite IP1 and IP5 of the LHC, where the highest instantaneous luminosity of collision is produced. They are designed as hermetic, multi-purpose detectors that surround the interaction point and measure the debris of proton and ion collisions. The “LHC beauty” (LHCb), located at IP8 is a forward, one-arm spectrometer devoted to the study of CP-violation in B hadrons. “A Large Ion Collider Experiment” (ALICE) is installed in IP2 and is built to study heavy ion collisions and quark-gluon plasmas.

## 3.2 The Compact Muon Solenoid Experiment

The CMS experiment is performed with a general-purpose particle detector operating at IP5, one of the high-luminosity interaction points of the LHC. It is designed to pursue a broad range of physics programs, from the discovery of the Higgs boson to searches for new physics signatures at the TeV scale. The requirements to meet the goals of the physics programs can be summarized as follows [60]:

- Good muon identification and momentum resolution, good dimuon mass resolution ( $\sim \mathcal{O}(1)\%$  at 100 GeV), and the ability to determine unambiguously the charge of muons;
- Good charged-particle momentum resolution and reconstruction efficiency, efficient triggering and offline tagging of  $\tau$ 's and b-jets;
- Good electromagnetic energy resolution, good diphoton and dielectron mass resolution ( $\sim \mathcal{O}(1)\%$  at 100 GeV), wide geometric coverage,  $\pi^0$  rejection, and efficient photon and lepton isolation at high luminosities;
- Good missing-transverse-energy and dijet-mass resolution.

To meet these requirements, the design of the CMS detector was decided in favor of a high magnetic field and a compact design, where the detector gets its name from. High granularity and readout capability are also required due to the extreme condition of the LHC, with a high bunch-crossing frequency and a large number of additional interactions in the same or neighboring bunch crossings (pileup). All these aspects were considered in the designs of the CMS subdetector systems.

The CMS detector is 28.7 m long, has a diameter of 15.0 m and weighs 14000 t. It is instrumented with multiple, concentric layers of detectors to identify and measure the particles produced in the collision, arranged in a central cylinder, the barrel, and closed by two endcaps. The key elements of the CMS detector, illustrated in Fig. 3.2, can be summarized as follows:

- An inner tracking system, which measures the trajectory of charged particles and reconstructs secondary vertices;
- An electromagnetic calorimeter, which measures and absorbs the energy of electrons and photons;

- A hadronic calorimeter, which measures and absorbs the energy of hadrons;
- A superconducting magnet, which provides a 3.8 T magnetic field parallel to the beam axis to bend the tracks of charged particles;
- A muon system, which measures the energy of muons and reconstructs their tracks.

In addition, a trigger system is installed to collect only events with interesting physics from an extremely high collision rate of 40 MHz at the LHC. More details about the subdetectors are described in the next sections.

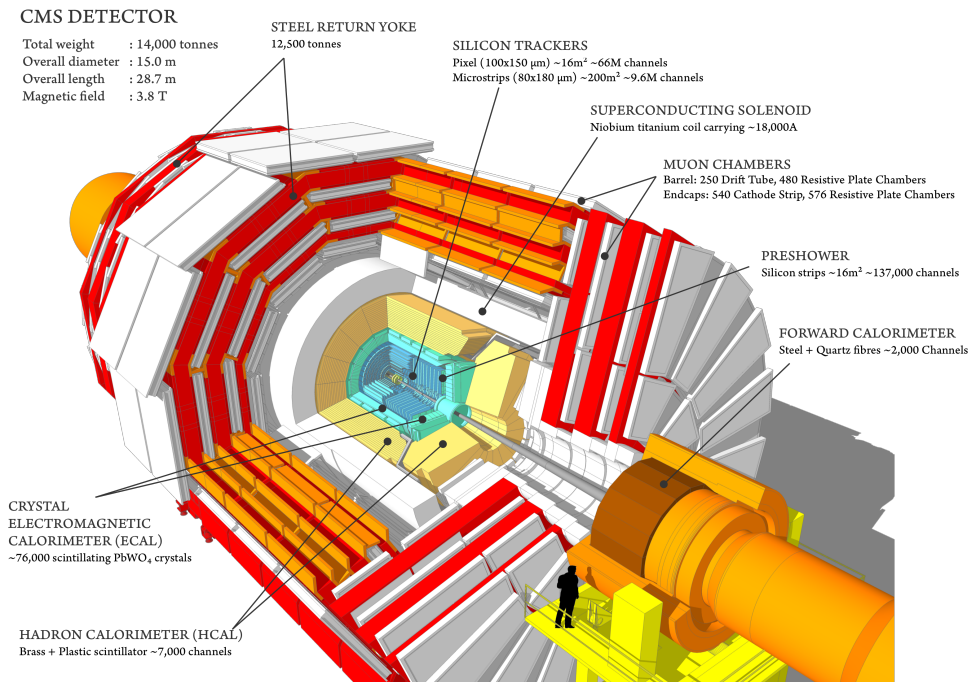


Figure 3.2: Overview layout of the CMS detector [60].

### 3.2.1 Coordinate System

The CMS coordinate system has its origin centered at the nominal interaction point inside the CMS experiment. The  $x$  axis of Cartesian coordinates is defined to point radially inward toward the center of the LHC, while the  $y$  axis is oriented vertically upward. The radial distance in the  $x$ - $y$  plane is denoted by  $r$ . The  $z$  axis is set along a counterclockwise direction around the LHC ring from the top view. The azimuthal angle  $\phi$  is measured counterclockwise from the  $x$  axis. The polar angle measured from the  $z$  axis is denoted by  $\theta$ , and can convert to pseudorapidity  $\eta$  in the following manner:

$$\eta = -\ln(\tan(\theta/2)) \quad (3.4)$$

Although  $\eta$  itself is not a Lorentz-invariant quantity, a difference of two particles in  $\eta$  is invariant. In this way, we can define a Lorentz-invariant angular distance

$$\Delta R = \sqrt{(\Delta\eta)^2 + (\Delta\phi)^2}. \quad (3.5)$$

The transverse momentum  $p_T$  has a useful property that the vector sum of  $p_T$  of all final-state particles from the collision is virtually zero since the incident partons have negligible  $p_T$  compared to the collision energy scale. Therefore, a large value of the vector sum indicates the presence of undetected particles (typically neutrinos) in the final state and their  $p_T$  is given by the negative of the vector sum so called the missing transverse momentum  $p_T^{\text{miss}}$ .

### 3.2.2 Tracker

The CMS tracking system is the innermost subdetector of the CMS detector. It is designed to measure the trajectories of charged particles with great precision, thereby identifying the momenta and charges of the particles as well as the interaction vertices. The region of tracking is set in a volume of 5.8 m of

length and 2.5 m of diameter, directly surrounding the interaction point. To achieve precise spatial measurement under a large flux of charged particles, the tracking system is partitioned in a high level of granularity and equipped with high speed front-end electronics. In addition, a minimum amount of material is used for its construction in order to minimize the impact of particle-material interaction on tracking. The CMS tracking system employs the silicon detector technology to address such technical concerns. A sectional view of the tracker is shown in Fig. 3.3.

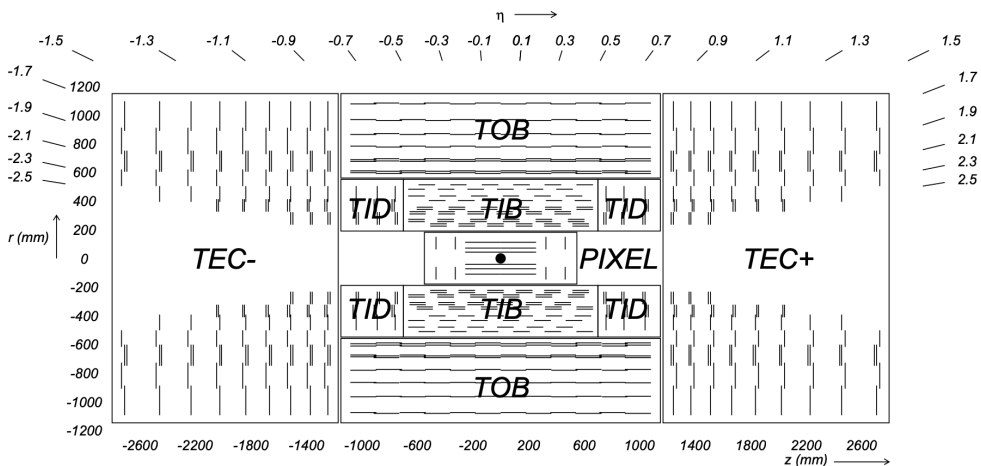


Figure 3.3: Longitudinal view of the CMS inner tracking system layout [60].

The silicon pixel detector is located in the inner region of the tracking system. It originally consisted of three layers in the barrel and two disks in the endcaps in 2016 and has been upgraded to four barrel layers and three endcap disks since 2017. Each pixel covers an area of  $100 \times 150 \mu\text{m}^2$ . The spatial resolution is measured to be about  $10 \mu\text{m}$  in the transverse direction and about  $20\text{--}40 \mu\text{m}$  along the beam direction. Its precision allows the secondary vertex reconstruction and the impact parameter resolution necessary for the

identification of heavy flavor quark decays.

The outer region of the CMS tracking system is instrumented with strip silicon sensors, extending the tracking measurement up to  $|\eta| = 2.5$ . The strip tracker is composed of four subsystems: the Tracker Inner Barrels (TIB), Tracker Inner Disks (TID), the Tracker Outer Barrels (TOB) and the Tracker EndCaps (TEC). The modules in the TIB and the TID provide up to four measurements of a track in the  $r$ - $\phi$  plane, while the TOB provides six more measurements, covering up to  $r = 116$  cm and  $z = \pm 118$  cm. Outside this range, the TEC provides 9 measurements. The spatial resolution is given as a function of  $r$ , ranging from 20 to 50  $\mu\text{m}$  in the radial direction and from 200 to 500  $\mu\text{m}$  in the  $z$ -direction.

### 3.2.3 Electromagnetic Calorimeter

The electromagnetic calorimeter (ECAL) measures the energy of electrons and photons. It consists of around 76000 lead-tungstate ( $\text{PbWO}_4$ ) crystals arranged in the barrel and endcaps, as illustrated in Fig. 3.4. Electrons and photons entering crystals evolve into electromagnetic showers, and the showers ionize the crystal atoms emitting scintillation light that is collected by photodetectors. Lead-tungstate crystals have properties of a high density ( $\rho = 8.28$  g/cm<sup>3</sup>), a short radiation length ( $X_0 = 0.89$  cm) and a small Molière radius ( $R_M = 2.19$  cm). Furthermore, a short scintillation decay time is required so that 80% of the light is emitted within the bunch spacing of 25 ns. The scintillation light is emitted mainly in the range of 420–430 nm.

The ECAL barrel detector extends to  $|\eta| < 1.479$ , with a granularity of 360-fold in  $\phi$  and of 190-fold in  $\eta$ . The endcap detectors cover the range between  $1.479 < |\eta| < 3.0$ . As scintillation and amplification processes are highly sensitive on the temperature, the operating temperature is carefully stabilized

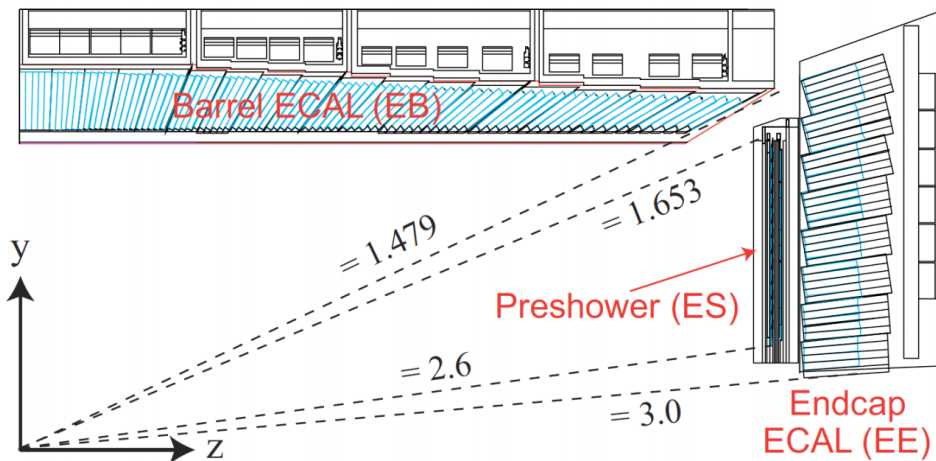


Figure 3.4: Longitudinal view of the ECAL layout [61], representing one quarter of the detector. The barrel and endcaps sections and the preshower detector are shown.

within 0.05 K. The ECAL energy resolution is described as a function of the energy:

$$\left(\frac{\sigma}{E}\right)^2 = \left(\frac{S}{\sqrt{E}}\right)^2 + \left(\frac{N}{E}\right)^2 + C^2, \quad (3.6)$$

where  $S$  is a stochastic term that depends on the number of secondary particles produced,  $N$  represents noise in the electronics and digitization, and the constant term  $C$  accounts for detector inhomogeneities. The parameters are measured using electron test beams:  $S = 2.8\%$ ,  $N = 12\%$ , and  $C = 0.3\%$  [62]. The ECAL has an excellent energy resolution of 1–3% for photons from the decay of the Higgs boson being reconstructed in the barrel and a similar resolution for electrons.

### 3.2.4 Hadron Calorimeter

The hadronic calorimeter (HCAL) is designed to measure the energy of hadrons. Located around the ECAL, the HCAL extends between  $1.77 < r < 2.95$  m up to the magnet coil. Because of the limited space between the ECAL and the magnet, the HCAL needs to be compact and made from materials with short interaction lengths. In addition, to provide a good measurement of the transverse missing energy in the event, it should be as hermetic as possible and extend to large  $|\eta|$  values. The HCAL is a sampling calorimeter, composed of layers of absorbers and scintillators, that measures destructively the energy of hadron jets.

The architecture of the HCAL is illustrated in Fig. 3.5. The hadron barrel calorimeter (HB), located inside the magnet coil, covers  $|\eta| < 1.3$ . It is divided in  $\eta \times \phi$  towers of dimension  $0.087 \times 0.087$ . The HB is made of 16 absorber plates, most of them being built with brass while the others are made of stainless steel. Because the thickness of the HB corresponds only to five to ten interaction lengths depending on  $\eta$ , an outer calorimeter (HO) is added around the magnet to complement the HB, and the total thickness of the combination of the HB and the HO increases to twelve interaction lengths. The hadron endcap calorimeter (HE) covers  $1.3 < |\eta| < 3.0$ , and is composed of brass absorber plates. Its thickness corresponds to approximately ten interaction lengths. Forward hadron calorimeters (HF) cover the high pseudorapidity regions ( $3.0 < |\eta| < 5.2$ ), which undergo high particle fluxes. They are Cherenkov light detectors made of radiation-hard quartz fibers. The ECAL and the HCAL combined can measure the energy of hadrons with a resolution  $\Delta E/E \sim 100\% \sqrt{E} \oplus 5\%$ .

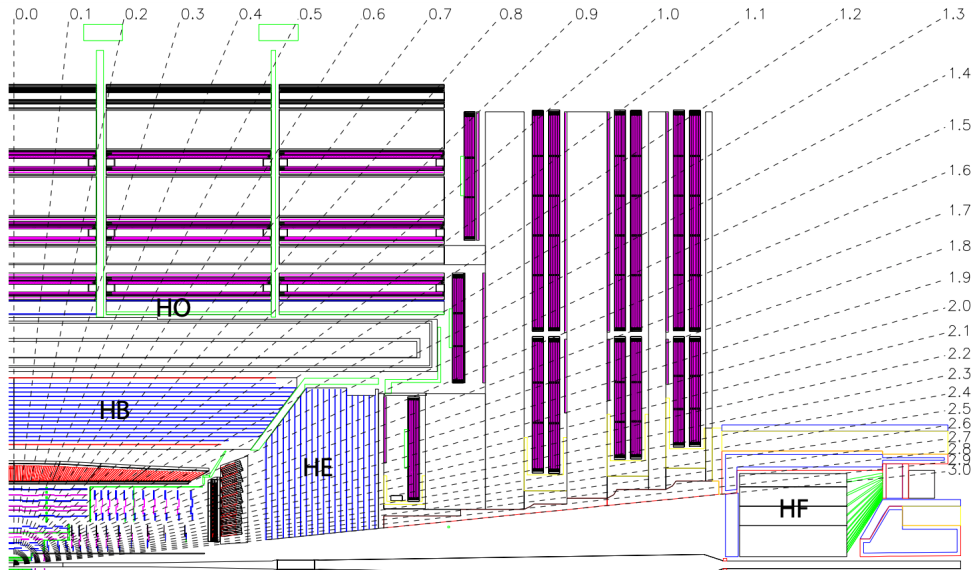


Figure 3.5: Longitudinal view of the HCAL [63]. The locations of the HB, HE, HO and HF calorimeters are indicated.

### 3.2.5 Superconducting Solenoid Magnet

An intense magnetic field of 3.8 T, which is essential for measuring the momentum and charge of charged particles, is generated by the CMS solenoid magnet consisting of superconducting Nb-Ti coils. The magnet with a length of 13 m and an internal diameter of 5.9 m envelops the tracker and calorimeters inside. It consists mainly of three parts: the coil, vacuum tank and yoke. The vacuum tank acts as a cryostat and provide the essential cooling to the solenoid using liquid He. The return yoke is made up of iron and is present outside the magnet coil reaching an outer diameter of 14 m. It is responsible for the return of the magnetic flux with a field of 2 T. The yoke is a 12-sided structure made up of 11 discs, 5 in the barrel and 6 in the endcaps. The muon chambers are housed in between the sections of the return yoke so that a

sufficient field strength is guaranteed in the muon detector system. The total energy stored inside the magnet amounts to around 2.6 GJ.

### 3.2.6 Muon Detector

Muons pass through the inner volume of the CMS solenoid without being stopped until they are finally measured in the muon detector system situated in the outermost part of the CMS detector. The CMS muon detector is equipped with three types of muon detectors based on the expected background rates and uniformity of the magnetic field, as illustrated in Fig. 3.6.

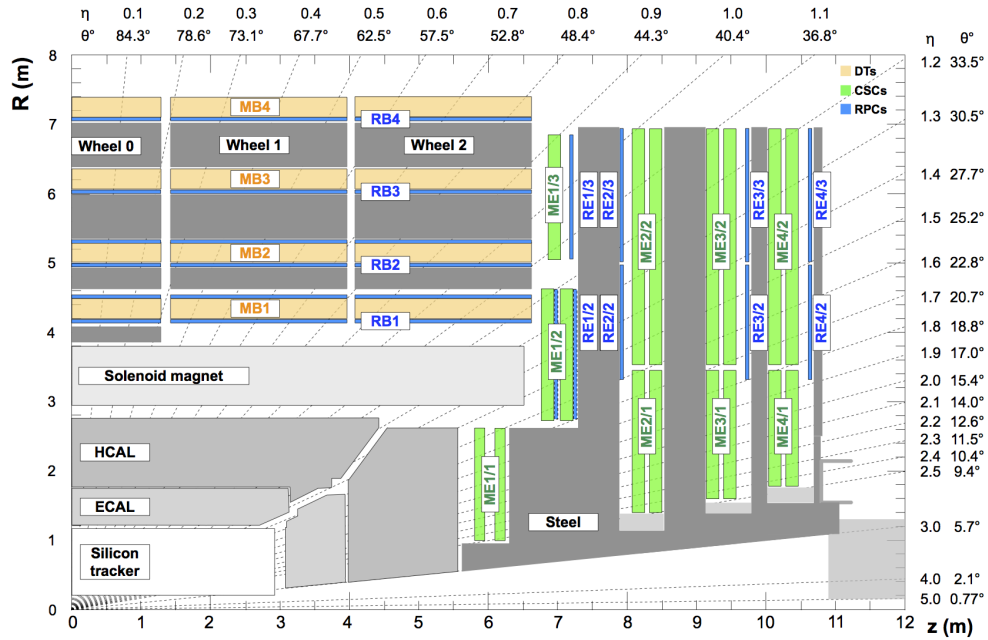


Figure 3.6: A cross section of a quadrant of the CMS muon detector [64]. The orange, green, and blue regions denote respectively the DTs, CSCs, and RPCs subsystems.

The CMS employs 250 drift tubes (DTs) uniformly arranged in the five

barrel sections covering  $|\eta| < 1.2$ . Each section has four DT stations in the form of concentric rings. The DTs are segmented into drift cells containing an anode wire and filled with a mixture of Ar and CO<sub>2</sub> gases. Traversing muons ionize the gas, and their position and angle are measured from the time needed by the electrons to drift toward the anode wires. The spatial resolution of the DTs is measured to be better than 250–300  $\mu\text{m}$  in the  $r$ - $\phi$  plane and about 250–600  $\mu\text{m}$  in the  $r$ - $\eta$  plane [64].

Cathode strip chambers detectors (CSCs) are used to measure muons in the region  $0.9 < |\eta| < 2.4$ . They are designed to operate in a high rate of ionizing particles and at the non-uniform magnetic field present in the forward region. The CSCs contain a mixture of Ar, CO<sub>2</sub>, and CF<sub>4</sub> gases, which is ionized upon the passage of a muon. Each CSC chamber is composed of six staggered layers, each measuring the muon position in two coordinates. The cathode strips are oriented in the  $r$  direction to measure the muon position in the  $r$ - $\phi$  plane, whereas the anode wires roughly measure the muon position in  $r$ . The spatial resolution in the CSC system is about 45–134  $\mu\text{m}$  [64].

Resistive plate chambers (RPCs), primarily designed to provide timing information for the muon trigger, are located in the region  $|\eta| < 1.9$ . The RPCs are double-gap chambers consisting of Bakelite plates filled with a mixture of C<sub>2</sub>H<sub>2</sub>F<sub>4</sub>, iC<sub>4</sub>H<sub>10</sub>, and SF<sub>6</sub> gases. The chambers are operating in an avalanche mode; an avalanche of electrons inside the gas volume is triggered by the passage of a muon and picked up by external metallic strips between the gaps. In spite of the modest spatial resolution of the RPCs (about 0.8–1.4 cm [64]), they provide an excellent time resolution of  $\approx 2$  ns for the identification of the bunch crossing to which measured muons are associated.

### 3.2.7 Trigger and Data Acquisition

The LHC machine provides 40 million pp collisions each second. They are dominated by QCD processes of large cross sections, which are mostly outside the scope of the CMS physics program. Since it is not possible to process all those data due to limited computing resource, the CMS experiment adopts a trigger system to select only interesting physics events from the high rate of collisions. The CMS trigger system features a two-level trigger architecture; the hardware-based Level-1 (L1) trigger and the software-based High-Level Trigger (HLT).

The L1 trigger is a hardware-based system with a fixed latency of  $4\ \mu\text{s}$ , implemented in the front-end electronics inside the CMS detector itself or inside the neighboring service cavern. It largely consists of the calorimeter trigger, the muon trigger, and the global trigger. The calorimeter trigger has two trigger layers: Layer-1 receives, calibrates, and sorts the local energy deposits so called trigger primitives, which are sent to the trigger by the ECAL and HCAL; Layer-2 uses these calibrated trigger primitives to reconstruct and calibrate the physics objects such as electrons,  $\tau$  leptons, jets, and energy sums. The muon trigger includes three muon track finders that reconstruct muons in the barrel, overlap, and endcap regions of the detector, then send them to the global muon trigger for final muon selection. The global trigger finally collects muons and calorimeter objects from the global muon trigger and the Layer-2 calorimeter trigger, and executes every algorithm in the menu in parallel for the final trigger decision. In this way, the L1 trigger reduces the event rate from 40 MHz to 100 kHz.

The HLT is implemented in software that are executed in a farm of commercial computing processors. The HLT tests each event accepted by the L1 trigger against a set of high-level trigger paths. Each trigger path is a se-

quence of reconstruction and selection steps of increasing complexity. The filtering process uses the full granularity data from the CMS detector, and the selection is based on a reduced sequence of the full offline event reconstruction algorithms. The HLT starts with the L1 information, and then improves the reconstruction and filtering process by exploiting also the tracker information. However, to reduce the CPU time, the detector read-out and reconstruction are restricted to narrow regions around the L1 or higher-level candidates. The most challenging aspect of the CMS HLT is to maximize the efficiency while keeping the CPU time acceptable. As a result, the HLT further reduces the event rate to about 1 kHz.

Events accepted by the HLT are transferred to the CMS offline computing infrastructure, which consists of computer farms linked with high-speed networks, with the bulk of the computing resource located in computing centers around the globe. The computing resources are divided into Tiers according to function and expected reliability. The Tier-0 center at CERN performs the prompt reconstruction of the data and distributes it to several Tier-1 centers for storage, where late-stage reconstruction with improved calibrations can take place. Data analysis and MC simulation happens primarily at Tier-2 centers, which are associated to Tier-1 sites and divide the resources between the CMS collaboration and the local physics community.

### **3.3 Event Reconstruction**

The raw detector signals collected by the CMS detectors are transferred to computing facilities and processed to create physics objects that are being used as the basic input on all the CMS data analyses. A global event reconstruction starts with the reconstruction of individual stable particles including electrons, photons, muons, charged hadrons and neutral hadrons. These are

subsequently combined to reconstruct more complex objects such as semileptonic  $\tau$  decays, jets, and missing transverse momentum. The information of reconstructed particles is combined to reconstruct high-level physics objects such as  $\tau$  lepton decays, jets, and neutrinos.

### 3.3.1 Particle-Flow Reconstruction

The CMS detector is based on the concept of cylindrical detection layers surrounding the beam axis, as illustrated in Fig. 3.7. Each detector layer measures an individual signature that is left by a final-state particle from the interaction point. A global event description based on this concept can be significantly improved by correlating and combining information from all detector layers (tracks and calorimeter clusters) to identify and reconstruct each final-state particle. This approach called particle-flow (PF) reconstruction [65] has been used for CMS event reconstruction. An individual physics object reconstruction in the PF reconstruction can be summarized as follows:

- Charged hadrons are identified by a link between a track and one or more calorimeter clusters, and by the absence of tracks in the muon detector system.
- Photons and neutral hadrons are identified by ECAL and HCAL clusters without any linked tracks.
- Electrons are identified by a track and an ECAL cluster, with a momentum-to-energy ratio compatible with unity, and not connected to an HCAL cluster.
- Muons are identified by a link between a track in the inner tracker and a track in the muon detector system.

These basic objects (called PF candidates) are combined to reconstruct complex objects such as jets, semileptonic  $\tau$  lepton decays, and neutrinos in a form of missing transverse momentum  $p_T^{\text{miss}}$ . The following sections describe the reconstruction of physics objects in detail.

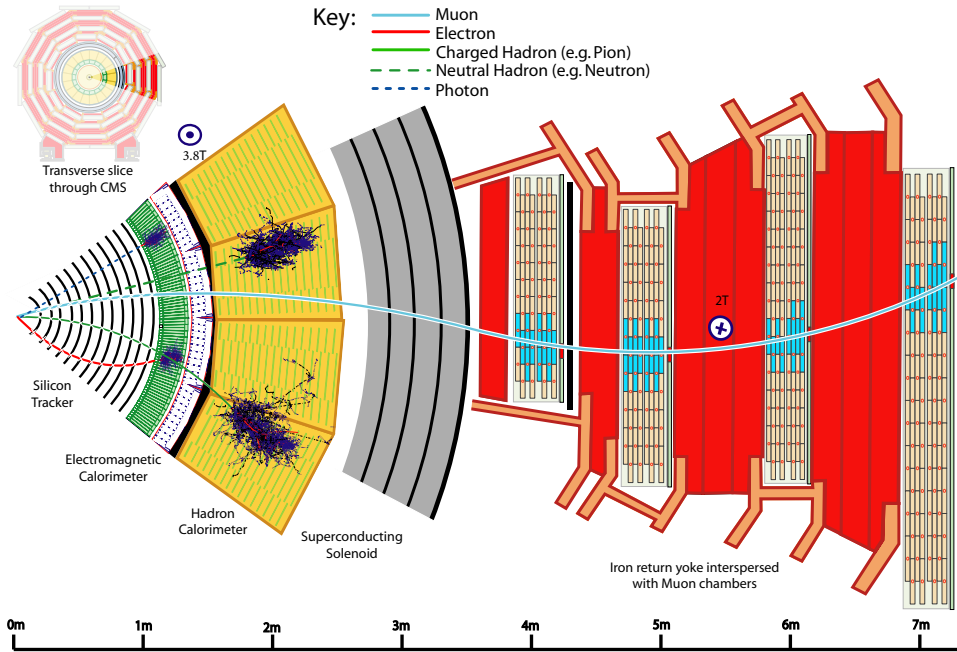


Figure 3.7: A sketch of the specific particle interactions in a transverse slice of the CMS detector, from the beam interaction region to the muon detector. The muon and the charged pion are positively charged, and the electron is negatively charged.

### 3.3.2 Muon Reconstruction

Muons are reconstructed by dedicated algorithms based on a Kalman filter method, which are independent of the PF tracking algorithms used for other charged particles. There are three muon reconstruction algorithms that exploit

the subdetectors information in different ways [64]:

- Standalone muons rely solely on the information from the muon subdetectors. Patterns in the DT, CSC, and RPC detectors are combined and fitted into a standalone muon track.
- Tracker muons are reconstructed from hits in the inner tracking detectors. Each track with  $p_T > 0.5$  GeV and a total momentum larger than 2.5 GeV is extrapolated to the muon subsystems, where the presence of at least one muon segment at a compatible position is required.
- Global muons combine the information from both detectors, by propagating inner tracks and standalone muon tracks to a common surface and verifying their compatibility. The combined collection of hits is fitted together to a global muon track. Because of the size of muon spectrometers, their inclusion in a global fit improves the  $p_T$  resolution for muons of  $p_T = 200$  GeV.

The outstanding performance of the tracking and the muon detector systems allows highly efficient muon reconstruction. About 99% of muons are reconstructed either as tracker and global muons, and those sharing the same inner track are linked as a single muon object. Standalone muons are rarely used due to its worse momentum resolution and a high rate of cosmic muon contamination.

Muon momentum and charge assignments are processed only by the tracker information for muons of  $p_T < 200$  GeV as the measurement from the muon detectors is degraded by multiple scattering effects. In the  $p_T$  range above 200 GeV, the global track is used instead, if the tracker-only measurement and the charge-to-momentum ratio agree with each other within two standard deviations. The muon  $p_T$  resolution ranges between 1 to 6%, depending on

the muon  $\eta$ , for muons with  $p_T < 100$  GeV, and is better than 10% for barrel muons of  $p_T = 1$  TeV.

### 3.3.3 Electron and Photon Reconstruction

Electron and photon reconstruction is primarily based on the measurement from the ECAL, in which electrons and photons deposit nearly all their energy. The tracker information is also combined with the ECAL information for electron reconstruction. Before reaching the ECAL, an electron or a photon may interact with a large amount of material in the tracker, resulting in bremsstrahlung photons and photon conversions into  $e^-e^+$  pairs. Thus, the ECAL may detect an electron or a photon not as a single entity but a set of multiple electrons and photons. The energy of the original electron or photon is recovered by a dedicated clustering algorithm to combine the energy deposits from the individual particles into a single object. In addition, the trajectory of an electron can be altered by the emission of bremsstrahlung photons. An electron track is built by a dedicated tracking algorithm using Gaussian Sum Filtering to account for the bremsstrahlung effect and is referred to as a GSF track [66]. Electron and photon reconstruction is fully integrated into the PF framework, using the same basic building blocks (tracks and clusters) as other particles. The reconstruction steps are summarized as below:

1. Clusters are built by collecting cells with energy above a threshold. A seed cluster is selected as the one containing most of the energy deposited in any considered region, with a minimum transverse energy of  $E_{T_{seed}} > E_{T_{seed}}^{min}$ .
2. In order to account for bremsstrahlung radiations and photon conversions, superclusters are formed of ECAL clusters within a geometric

window around the seeding cluster. The window depends on the  $p_T$  and  $\eta$  of the seeding cluster.

3. Trajectory seeds in the pixel detector are matched with both the supercluster position and the trajectory of an electron. The matched ones are used to seed the GSF tracking step.
4. Simultaneously with the above steps, general tracks are tested if they are compatible with electron trajectories. If so, they are used to seed the GSF tracking step.
5. A dedicated algorithm is applied to identify the general tracks originating from conversions.
6. All the output elements from the previous steps are imported into the PF algorithm to link the elements into blocks of particles.
7. The blocks are resolved into electron and photon objects. The final list of linked ECAL clusters for each candidate is promoted to a refined supercluster.
8. Electron or photon objects are reconstructed from the refined superclusters based on loose preselection requirements. Passers are all labeled as photons. In addition, if one has an associated GSF track, the object is labeled as an electron. The output collection is known as the unbiased  $e/\gamma$  collection and is popularly used as starting point by CMS analyses.
9. The  $e/\gamma$  objects are accepted as either an electron or an isolated photon in the PF framework if they pass a tighter selection. If it fails both selection criteria, the basic elements associated with it are released to form neutral hadrons, charged hadrons and non-isolated photons.

### 3.3.4 Hadron Reconstruction

Hadron reconstruction is initiated after muons, electrons, and isolated photons are all reconstructed and removed from the pool of the PF blocks. The ECAL and HCAL clusters that has no associated tracks can seed photons and neutral hadrons. All these ECAL and HCAL clusters within the tracker acceptance ( $|\eta| < 2.5$ ) are turned into photons and neutral hadrons, respectively. The priority given to photons for the ECAL clusters is based on the observation that, on average, photons carry 25% of the jet energy, while only 3% of the jet energy is left in the ECAL by neutral hadrons. However, it is not able to distinguish between charged and neutral hadrons outside the tracker acceptance, which leave in total 25% of the jet energy in the ECAL. The priority given to photons is therefore no longer valid. For this reason, ECAL clusters that are associated with a given HCAL cluster are considered to originate from the same hadron shower, while ECAL clusters with no linked HCAL clusters are identified as photons.

The energy of those photons and hadrons is calibrated. Each of the remaining HCAL clusters of the PF block is linked to one or several tracks (not linked to any other HCAL cluster) and these tracks may in turn be linked to some of the remaining ECAL clusters (each linked to only one of the tracks). The calibrated calorimetric energy is determined from the energy of the HCAL cluster and the total energy of the ECAL clusters, under the single charged-hadron hypothesis. The true energy, needed to determine the calibration coefficients, is estimated to be either the sum of the momenta of the tracks, or the sum of the raw ECAL and HCAL energies, whichever is larger. The sum of the track momenta is then compared to the calibrated calorimetric energy in order to determine the particle content, as described below.

If the calibrated calorimetric energy is in excess of the sum of the track

momenta by an amount larger than the expected calorimetric energy resolution for hadrons, the excess may be interpreted as the presence of photons and neutral hadrons. Specifically, if the excess is smaller than the total ECAL energy and larger than 500 MeV, it is identified as a photon with an energy corresponding to this excess after recalibration under the photon hypothesis. Otherwise, the recalibrated ECAL energy still gives rise to a photon, and the remaining part of the excess, if larger than 1 GeV, is identified as a neutral hadron. Each track gives rise to a charged hadron, the momentum and energy of which are directly taken from the corresponding track momentum, under the charged-pion mass hypothesis.

If the calibrated calorimetric energy is compatible with the sum of the track momenta, no neutral particle is identified. The charged-hadron momenta are redefined by a  $\chi^2$  fit of the measurements in the tracker and the calorimeters, which reduces to a weighted average if only one track is linked to the HCAL cluster. This combination is particularly relevant when the track parameters are measured with degraded resolutions, e.g. at very high energies or at large pseudorapidities. It ensures a smooth transition between the low-energy regime, dominated by the tracker measurements, and the high-energy regime, dominated by the calorimetric measurements. The resulting energy resolution is always better than that of the calorimetric energy measurement, even at the highest energies.

### 3.3.5 Jet Reconstruction

Jets are reconstructed by clustering the PF candidates, which are identified as the hadronization products, with the anti- $k_T$  algorithm [67]. The algorithm iteratively combines PF candidates that are close to each other according to

metrics,

$$d_{ij} = \min(k_{ti}^{-2}, k_{tj}^{-2}) \frac{\Delta_{ij}^2}{R^2}, \quad (3.7)$$

$$d_{iB} = k_{ti}^{-2}, \quad (3.8)$$

where  $k_{ti}$  and  $k_{tj}$  are the transverse momenta of the  $i$ - and  $j$ -th entities (PF candidates or pseudojets in reconstruction), respectively, and  $\Delta_{ij}^2 = (y_i - y_j)^2 + (\phi_i - \phi_j)^2$ . The size of the jet cone is determined by the distance parameter  $R$  at which the algorithm is operated. Both the values  $R = 0.4$  and  $R = 0.8$  are used in CMS. If the smallest distance is of  $d_{ij}$ -type, the entities  $i$  and  $j$  are combined into a new single entity, while if it is of  $d_{iB}$ -type, the  $i$  entity is considered as a jet and removed from the list of entities. The procedure continues until the entity list is empty. As a result, the anti- $k_T$  algorithm produces jets with a conical shape, clustered around the hardest particles and with boundaries resilient with respect to soft radiation.

The jet four momentum is computed as the vector sum of the clustered PF candidates four momenta, and a set of corrections are applied to calibrate the jet response using the information of generated particles in a simulation. These corrections of the jet energy scale take into account the contribution from pileup in the event, nonlinearities in the detector response to hadrons, and residual differences between the data and the simulation used for the method.

### 3.3.6 Semileptonic $\tau$ Lepton Decay Reconstruction

With a mean lifetime of about  $2.9 \times 10^{-13}$  sec, tau leptons decay within a few mm from their production point for the typical Lorentz boosts at the LHC. While fully leptonic decays to an electron or a muon in association with neutrinos are reconstructed from the respective object algorithms detailed above, semileptonic decays to hadrons ( $\tau_h$ ) and a neutrino result in a small

and collimated hadron jet that requires a specific reconstruction algorithm. The decay can occur through an intermediate  $\rho(770)$  or  $a_1(1260)$  resonance, and result in different multiplicities of charged and neutral hadrons, usually pions. Decays containing one and three charged hadrons are generally referred to as one- and three-prong decays, respectively.

The  $\tau_h$  reconstruction algorithm is required to determine the  $\tau$  decay mode, identify PF candidates associated to both charged hadrons and photons from neutral hadron decays, and regroup them together to estimate the  $\tau_h$  kinematic properties. The hadrons plus strips (HPS) algorithm [68] is designed to perform these tasks using the PF candidates previously reconstructed. The HPS reconstruction is initiated by PF jets that are formed as detailed in Section 3.3.5. The algorithm analyses the PF candidates composing each jet to verify their compatibility with a  $\tau_h$  object. The contribution from neutral pions in  $\pi^0 \rightarrow \gamma\gamma$  can appear either directly as photon PF candidates, or as electron candidates clustered inside the jet, due to the large photon conversion probability. Photon and electron PF candidates of  $p_T > 0.5$  GeV are thus clustered into “strips” with an iterative procedure. Electron and photon candidates within a clustering region around the strip are added to the strip itself, which position is recomputed as a  $p_T$ -weighted average. The strip creation ends when no candidates are found within the clustering region.

The strips and the charged hadrons in the jet are combined together to reconstruct any of these decay modes:

- $h^\pm$ , a single charged hadron with no strips
- $h^\pm\pi^0$ , a single charged hadron with one strip
- $h^\pm\pi^0\pi^0$ , a single charged hadron with two strips
- $h^\pm h^\mp h^\pm$ , three charged hadrons

Quality and invariant mass criteria are applied onto all the valid decay mode hypotheses to verify their compatibility with a  $\tau$  decay. The selections depend on the decay mode considered and on the  $e/\gamma$  candidates clustered into the strip. In case multiple decay mode hypotheses are satisfied, the one with the largest  $p_T$  is retained, resulting in an unique association of a  $\tau_h$  candidate to a jet.

### 3.3.7 Missing Transverse Momentum Reconstruction

The presence of undetected final state particles such as neutrinos can be indirectly inferred from the imbalance of the total transverse momentum vector sum. The  $p_T^{\text{miss}}$  vector is reconstructed with the PF algorithm as the negative of the vectorial sum of the transverse momenta of the PF candidates reconstructed in the event. As inefficiencies of the tracking algorithm, minimal thresholds in the calorimeter energy estimation, and nonlinearities of the energy response of the calorimeters for hadronic particles can introduce a bias in the  $p_T^{\text{miss}}$  determination, a correction is applied by propagating to the  $p_T^{\text{miss}}$  sum the jet energy corrections introduced in Section 3.3.5. In particular, the corrected  $p_T^{\text{miss}}$  vector is given by

$$p_T^{\text{miss,corr}} = p_T^{\text{miss}} - \sum_{jets} (p_T^{\text{corr}} - p_T), \quad (3.9)$$

taking into account the difference between the initial jet  $p_T$  and its corrected value  $p_T^{\text{corr}}$ . If a muon is found within the jet cone, its four-momentum is subtracted from the jet momentum when computing the correction and then added back into the  $p_T^{\text{miss}}$  sum.

# Chapter 4

## Data and Simulated Samples

### 4.1 Data

The data used for the resonant and nonresonant signal analyses correspond to an integrated luminosity of  $35.9 \text{ fb}^{-1}$ , recorded by the CMS detector in pp collisions at a center-of-mass energy of 13 TeV in 2016. The high instantaneous luminosity delivered by the LHC results in a large number of pileup interactions. The average number of pileup interactions in the 2016 data set is around 23.

In the resonant signal analysis, the use of isolated-lepton triggers, which are popularly used for leptonic channel analyses in CMS, is avoided in order to prevent a potential lepton isolation inefficiency in heavy resonance signal events. In such events, two leptons from Z boson decays are usually collimated by a very large Lorentz boost, and their isolation cones are thereby overlapped with each other. In the  $ee\gamma$  channel, the selected events are required to pass a double-photon trigger `HLT_DoublePhoton60`. This trigger requires  $p_T >$

60 GeV and  $|\eta| < 2.5$  on both photon candidates. Since the photon trigger requirements do not include any track veto, this trigger is equally efficient in selecting photon and electron candidates. A combination of single-muon triggers,

- HLT\_Mu50
- HLT\_TkMu50

are used in the  $\mu\mu\gamma$  channel. Both triggers require  $p_T > 50$  GeV and  $|\eta| < 2.4$  on a muon candidate.

On the contrary, such a constraint on the use of isolated-lepton triggers is removed in the nonresonant signal analysis as the event topology of the nonresonant signal does not impose a large Lorentz boost on the two leptons in the signal event. Events for the  $ee\gamma$  channel analysis are selected using double-electron triggers,

- HLT\_DoubleEle33\_CaloIdL\_MW
- HLT\_DoubleEle33\_CaloIdL\_GsfTrk\_IdVL

that impose  $p_T < 33$  GeV,  $|\eta| < 2.5$ , and online identification criteria for both electron candidates. The  $\mu\mu\gamma$  channel events are selected using single-muon triggers

- HLT\_IsoMu24
- HLT\_IsoTkMu24

that require muon isolation criteria,  $|\eta| < 2.4$ , and a threshold of 24 GeV on the muon  $p_T$ .

## 4.2 Simulated Samples

Simulated samples used for this thesis are produced in multiple steps to account for physics and various experimental effects. At the first step of simulation, events of the desired hard scattering process are generated using matrix element generators. The remaining part of the physics process including fragmentation and hadronization effects are simulated by a dedicated simulator. The simulated events are finally processed through the full CMS detector simulation and reconstructed by the same algorithms used for data that are explained in Section 3.3. More details about these simulation steps are described in Sections 4.2.1–4.2.5. Signal and background simulated samples are stated in Sections 4.2.6 and 4.2.7, respectively.

### 4.2.1 Parton Distribution Function

Partons inside hadrons can be resolved individually in hard processes such as pp collisions. Such partonic processes are described in terms of a parton distribution function (PDF)  $f_i(x, \mu^2)$ , which represents the probability of parton  $i$  carrying a fraction  $x$  of the proton momentum at an energy scale  $\mu$ . Its dependence on the energy scale  $\mu$  is determined by the DGLAP equations. If PDFs are measured at  $\mu_0$ , then PDFs at any other scales can also be derived from the measurement using the DGLAP equations. This derivation is handled perturbatively to a finite order, like any other quantities in perturbative QCD.

Simulated samples used in this thesis are generated with the NNPDF3.0 [69] PDF set. These PDF sets are based on fits of the theoretical DGLAP functional form to the experimentally-measured values of the PDFs from multiple experiments, examining a variety of processes at a range of different energy scales. The order used in its perturbative calculation is matched to that of the

cross section calculation.

## 4.2.2 Hard Process Generation

A generic hard scattering process of pp evolves as:

$$p + p \rightarrow X + rest. \quad (4.1)$$

The symbol  $X$  denotes a final-state particle or particles from a hard parton-parton collision, which can specify the energy scale of the process. The term *rest* represents the products of the rest part of the scattering process, typically low-energy hadrons originating from soft parton interactions. The total cross section  $\sigma_X$  of such a hard process can be decomposed into computable components through the QCD factorization theorem:

$$\sigma_X = \sum_{i,j} dx_1 dx_2 f_i(x_1, \mu_F^2) f_j(x_2, \mu_F^2) \sigma_{i,j \rightarrow X}, \quad (4.2)$$

where the two indexes  $i$  and  $j$  specify the types of the partons participated in the hard collision, and  $\sigma_{i,j \rightarrow X}$  is the partonic cross section for:

$$i + j \rightarrow X + rest', \quad (4.3)$$

which is calculable to a fixed order in perturbative QCD. The partonic cross section  $\sigma_{i,j \rightarrow X}$  is regulated by the factorization scale  $\mu_F$ . In addition, the running QCD coupling constant  $\alpha_S$ , which is included in the perturbative series of  $\sigma_{i,j \rightarrow X}$ , depends on the renormalization scale  $\mu_R$ . The perturbative expansion of  $\sigma_{i,j \rightarrow X}$ , therefore, depends on both  $\mu_F$  and  $\mu_R$  in a way that they are canceled out and do not appear in the exact formula for  $\sigma_X$ , which is a physically observable quantity. However, the approximate value of the cross section that is perturbatively computed to a fixed order still has nonzero dependence on  $\mu_F$  and  $\mu_R$ . In CMS simulation, both the factorization and the renormalization

scales are chosen equal to the mass of the Z boson  $\approx 91.2$  GeV, which has been used as the standard choice of  $\mu_R$  for  $\alpha_S$  measurements. This choice of  $\mu_F$  and  $\mu_R$  brings theoretical uncertainty in the SM cross sections used in the nonresonant signal search. The procedure to estimate the magnitude of this systematic uncertainty is described in Section 8.

The total cross section  $\sigma_X$  for the process  $p + p \rightarrow X + rest$  is required to be differentiated with respect to kinematic variables of  $X$  in order to simulate kinematic distributions of final-state particles. The differential cross section as the outcome of differentiation may be obtainable for an individual elementary partonic process. Given complexity of the full dynamics of a pp collision convoluted with various detector effects, however, it is virtually impossible to calculate simple analytic or numerical solutions even at the lowest order. Monte Carlo (MC) simulations have been popularly adopted to solve this computational conundrum. In MC simulations, events are randomly generated according to known probability density functions of kinematic variables. The cross section in a given kinematic range is obtained by the product of the total cross section and the fraction of the events that belong to the given range. MC event generators provide MC estimates of hard collisions with initial-state and final-state kinematics sampled from PDFs and the differential partonic cross sections, respectively.

### 4.2.3 Parton Showering and Hadronization

The output of the hard collision,  $X + rest$ , continues to evolve as it exits the interaction point. For example, high-energy quarks and gluons will tend to radiate other quarks and gluons in a cascading process known as a parton shower, dispersing their energy as they do so. The energies of the showering partons begin at the hard interaction energy scale and go down to the

hadronization scale ( $\lesssim 10$  GeV). Above this energy scale,  $\alpha_S$  is less than  $O(1)$ , and so the parton shower process admits a perturbative analysis in the theory of QCD. The statistical behavior of parton showering is governed by Sudakov form factors derived from the DGLAP equations [70].

Below the hadronization scale, the remnant partons will no longer have enough energy to freely split and will finally bind into hadrons in a process called hadronization. This occurs as the value of  $\alpha_S$  associated with a typical parton energy rises above  $O(1)$ , rendering estimates based on perturbative expansions invalid. The bulk of the partons in the colliding protons are not directly involved in the hard parton–parton scatter and are also subject to a nonperturbative energy scale; these contribute softer showers of particles known as the underlying event. These nonperturbative processes are simulated with generator-dependent phenomenological models, tuned to match the hadronic distributions observed in the experiment. For all the simulated samples used in this thesis, both parton showering and hadronization are handled by PYTHIA 8.205 [71], with the CUETP8M1 [72] underlying-event tune.

#### 4.2.4 Pileup Interactions

The simulated contribution from pileup is estimated by overlaying additional “minimum-bias” events, with simulated particle distributions corresponding to the typical pp scattering events most likely to occur in the LHC. These are estimated by taking LHC collision data with no special trigger selections applied. The generation of minimum-bias events is handled by PYTHIA. The simulated pileup distribution is usually not perfectly matched with the data distribution which are affected by variable data-taking conditions. Thus, the simulated events are weighted to match the pileup distribution observed in the data.

### 4.2.5 Detector Simulation

The output of the preceding steps is a collection of several thousand stable or semistable particles that continue to propagate outward and interact with the detector. They are taken as input to the detector simulation step.

The CMS full detector simulation is based on GEANT4 [73], a toolkit for simulating the passage of particles through matter. It includes a complete range of functionality including tracking, geometry, physics models and hits. The physics processes offered cover a comprehensive range, including electromagnetic, hadronic and optical processes, a large set of long-lived particles, materials and elements. It has been designed and constructed to expose the physics models utilized, to handle complex geometries, and to enable its easy adaptation for optimal use in different sets of applications.

Special effort has been made to validate the physics models of GEANT4 for CMS, using an elaborate set of measurements in dedicated test beam setups. The single particle response in the prototype CMS calorimeters has been measured in these experiments using electron and hadron beams over a large range of energy. Measurements of the single particle response from collision data are also used in testing the predictions of GEANT4.

The CMS-specific requirements on the simulation can be summarized as follows:

- The requirements for simulating the CMS tracker are the following:
  - a high degree of accuracy in the description of active and passive components;
  - correct, navigable Monte Carlo truth information;
  - a very precise treatment of hard electron bremsstrahlung

The tracker geometry has been very carefully built describing each component in great detail. Each of these components is reviewed with full information from integration centers and then verified by weighing individual components prior to testing the simulation against collision data. Special care is taken in the choice of the physics model of GEANT4 for  $\delta$ -ray production and electron bremsstrahlung. The simulation results have been extensively validated in terms of signal simulation, tracking,  $dE/dx$ , etc.

- Simulation of the ECAL requires an accurate description of geometry and material budget and a good and complete implementation of the electromagnetic physics process. The geometry of the ECAL is provided with possible independent alignment of modules, super-crystals, wafers etc. The updated distributions of support, cooling, readout are again tested by making specific measurements and finally with collision data. Precise electron and photon identification and the energy measurement require a good understanding of the transverse shower profile (containment, calibrations) as well as longitudinal shower profile (leakage). The simulation has been validated extensively with test beam and collision data for energy measurement and transverse shower profiles.
- Simulation of the HCAL requires faithful description of timings, noise as well as energy response as a function of energy. The simulation utilizes shower libraries, noise libraries to overcome some of the limitations (performance, description of different types of noises). The HCAL community made several comparisons for single particle measurements between test beam data (2002–2007) and MC, with different HCAL modules, preceded by real ECAL super-module or prototype, to beams of hadrons,

electrons and muons over large energy range. The studies on energy resolution and linearity, e/h ratio, and shower profile are instrumental in validating GEANT4 hadronic physics models. Some of these measurements are repeated using isolated charged hadrons in the collision data. The momenta of these particles are well measured by the tracker. To ensure that there is no contamination due to other nearby particles, suitable isolation criteria are applied.

- For the muon system, the geometry description in simulation is verified using the Cosmic data collected during the various cosmic runs (MTCC, CRAFT, etc.) and finally from the collision data. Muon physics in GEANT4 is extensively tested and validated in the energy range 10 GeV–10 TeV. An improved description of  $\mu$  bremsstrahlung,  $\mu$ -nuclear effects and a better description of multiple scattering (in agreement of data) have been introduced in recent versions of GEANT4. These new descriptions are validated with earlier simulation and with collision data.

#### 4.2.6 Signal Samples

To model the detector acceptance and event selection efficiency of signal events, simulated signal samples are generated at leading order (LO) in perturbative QCD using PYTHIA.

$Z\gamma$  resonance signal samples are generated with masses ranging from 0.3 to 4.0 TeV. Two resonance width assumptions were used in the simulation: one, termed “narrow”, has its width ( $\Gamma_X$ ) set to 0.014% of the resonance mass ( $m_X$ ), and the second, referred to as “broad”, has  $\Gamma_X/m_X = 5.6\%$ . The first choice corresponds to a resonance with a natural width much smaller than the detector resolution. The second choice facilitates a direct comparison with the previous CMS publications [25, 32]. We assume no interference between signal

and the SM nonresonant  $Z\gamma$  production.

Excited lepton signal samples are generated with masses ranging from 0.25 to 5.0 TeV. The signal samples are generated at the compositeness scale  $\Lambda = 10$  TeV, but are also used for different compositeness scale interpretations since this parameter has a negligible impact on the kinematic distributions of final-state particles. A mass-dependent  $K$  factor for next-to-leading-order (NLO) corrections is applied [74].

#### 4.2.7 Background Samples

Major SM background processes such as  $DY+\gamma$  and  $t\bar{t}+\gamma$  are generated at NLO using the MADGRAPH5\_aMC@NLO 2.3.3 generator [75], while WW, WZ, and ZZ backgrounds are generated at LO with PYTHIA. The cross section for WW production is calculated at next-to-next-to-leading order [76] and the cross sections for WZ and ZZ production are computed at NLO [77]. In the resonant signal search, simulated background events do not enter the analysis directly, as the backgrounds are obtained from fits to data, but are used to assess the accuracy of the background model and to optimize event selection.

# Chapter 5

## Event Selection

### 5.1 Electron and Photon Selection

CMS implements different strategies to identify prompt and isolated electrons and photons and discriminate them from background sources. Possible background sources for electrons range from photon conversions, jets misidentified as electrons, or electrons from semileptonic decays of b and c quarks. For photons, the most important background originates from jets fragmenting mainly into a light neutral meson  $\pi^0$  or  $\eta$ , which decay with large branching fractions to  $\gamma\gamma$ . For the energy range of pp collisions at the LHC,  $\pi^0$  and  $\eta$  are highly boosted such that the two photons from the decay propagate nearly collinear and appear as a single photon on the calorimeter.

#### 5.1.1 Isolation Criteria

The use of isolation energy sums, which consist of the sum of reconstructed energy in a cone around the reconstructed object, is one of the most reliable ways for background rejection of electrons and photons. An isolation cone is

set in terms of  $\Delta R$  with respect to the reconstructed object. A small veto region is defined inside the isolation cone so as to guarantee that the energy of the particle itself is not included in its isolation sum. The energy from the veto region is removed from the isolation sum.

Photon and electron isolation is measured exploiting the information provided by the PF event reconstruction. The isolation variables are calculated by summing the transverse momenta of charged hadrons ( $I_{ch}$ ), photons ( $I_\gamma$ ), and neutral hadrons ( $I_n$ ), inside the isolation cone of  $\Delta R = 0.3$  with respect to the position of the electron or photon.

The isolation variables need to be corrected to remove the pileup contribution. The pileup contribution is estimated by  $\rho \times A_{eff}$ , where  $\rho$  is the median of the transverse energy density per unit area in the event, and  $A_{eff}$  is the area of the isolation region weighted by a factor that takes into account the dependence of the pileup transverse energy density on the object  $\eta$ .

### 5.1.2 Shower Shape Criteria

The shape of the energy deposit on the ECAL can be exploited to reject misidentified jets with high electromagnetic content. Although the two photons from hadrons decays cannot be clearly distinguished, such objects nevertheless have wider shower profiles on average than a single photon or electron incident upon the ECAL. This distinction is in particular manifest along the  $\eta$  axis of the cluster, as the discrimination based on the  $\phi$  profile of the shower is diminished by the effect of the magnetic field. The following two shape variables are used for photon and electron identification.

- Hadronic over electromagnetic energy ratio ( $H/E$ ): the ratio between the HCAL energy deposit within a cone of  $\Delta R = 0.15$  and the photon or electron candidate energy. The  $H$  of a real electromagnetic object can

mainly originate from three sources: HCAL noise, pileup and leakage of electrons or photons through the inter-modular gaps. The first two sources dominate for low energy electrons and photons. The last term is the main contributor for high energy electrons. To account for both low and high energy regions,  $H/E$  is parameterized as  $H < X \cdot Y \cdot \rho + Z \cdot E$  where  $X$  and  $Y$  denote the contributions from the noise and pileup, respectively, and  $Z$  is a coefficient for high energy electrons and photons.

- $\sigma_{i\eta i\eta}$ : the second moment of the log-weighted distribution of crystal energies along the  $\eta$  axis, which is evaluated in the  $5 \times 5$  matrix around the most energetic crystal in the supercluster and rescaled to units of crystal size. The distribution of this variable should be narrow for a single photon or electron shower, and broad for two-photon showers that come from a neutral meson decay.

### 5.1.3 Electron Selection

On top of isolation criteria and shower shape criteria, tracker-related variables are additionally exploited for electron identification. One of such variables is  $|1/E - 1/p|$ , where  $E$  is the supercluster energy, and  $p$  is the track momentum at the point of closest approach to the vertex. This variable compares the measurements obtained from the ECAL and the tracker, which are compatible with each other for electrons. In a similar vein, there are two discriminant variables to ensure the smallness of the angular difference between the track and the cluster:  $|\Delta\eta_{seed}| = |\eta_{seed} - \eta_{track}|$ , where  $\eta_{seed}$  denotes the seed cluster position in  $\eta$  and  $\eta_{track}$  is the track  $\eta$  extrapolated from the innermost track position, and  $|\Delta\phi_{in}| = |\phi_{SC} - \phi_{track}|$ , which uses the supercluster energy-weighted position in  $\phi$  instead of the seed cluster  $\phi$ .

### 5.1.4 Photon Selection

Photon candidates are required to pass photon identification criteria based on a multivariate analysis using a BDT implemented in the TMVA framework [78]. The BDT score based on multiple input variables serves as a single discriminant variable. Isolation and shower-shape variables that are described in the previous sections are used as the input to the BDT. Besides, there are three more variables used to enforce the separation between signal and background photons: the median energy per unit area  $\rho$  and the  $\eta$  and uncorrected energy of the supercluster corresponding to the candidate photon. A veto based on the tracker information is applied in order to reject electrons.

## 5.2 Muon Selection

A hadron may be misidentified as a prompt muon if the hadron decays in flight, or if hadron shower remnants penetrate through the calorimeters and reach the muon system (punch-through), or if there is a random matching between a hadron track in the inner tracker and a segment or standalone-muon in the muon system. The following variables are used to identify prompt muons of good reconstruction quality:

- The minimum number requirement of muon-chamber hits is required to suppress hadronic punch-through events and muons from decays in flight.
- The minimum number of muon stations that have muon segments is set in order to reject punch-through events and accidental track-to-segment matches. Also it makes selection consistent with online muon identification, which requires segments in at least two muon stations to obtain a meaningful estimate of the muon  $p_T$ .

- The smallness of the  $p_T$  relative error of the muon best track guarantees the quality of muon  $p_T$  reconstruction.
- A cut on the transverse impact parameter  $d_{xy}$  is exploited for the rejection of cosmic muons and muons from decays in flight.
- The maximum longitudinal distance  $d_z$  condition is set to further suppress cosmic muons, muons from decays in flight and tracks from pileup.
- A cut on the number of pixel hits can further suppress muons from decays in flight.
- The number of tracker layers with hits is related to a good  $p_T$  measurement, for which some minimal number of measurement points in the tracker is needed. It can be also used to suppresses muons from decays in flight.

To distinguish between prompt muons and those from weak decays within jets, the isolation of a muon is evaluated relative to its  $p_T$  by summing up the energy in a geometrical cone, surrounding the muon. One strategy sums reconstructed tracks (track based isolation), while another uses charged hadrons and neutral particles coming from PF (PF isolation). The tracker-based isolation criteria is used for both analyses described in this thesis.

### 5.3 Resonant Signal Selection

In the resonant signal analysis, additional treatments are applied to lepton isolation in order to ensure high lepton identification efficiency even in the topologies where a Z boson has a high Lorentz boost, as expected for Z bosons produced in a decay of a heavy resonance. For an electron, the isolation cone

size  $\Delta R$  depends on its  $p_T$ :

$$\Delta R = \begin{cases} 0.2, & \text{for } p_T \leq 50 \text{ GeV}, \\ \frac{10 \text{ GeV}}{p_T}, & \text{for } 50 < p_T \leq 200 \text{ GeV, and} \\ 0.05, & \text{for } p_T > 200 \text{ GeV.} \end{cases} \quad (5.1)$$

The varying isolation cone radius in Eq. (5.1) takes into account the aperture of b hadron decays as a function of their  $p_T$ , and reduces the inefficiency from accidental overlap of electrons from Z boson decays and jets. In the case of two spatially close muons in the event, with overlapping isolation cones, both muons are excluded from each isolation sum.

Events are required to have two same-flavor leptons (electrons or muons) and a photon. Additionally, leptons in the  $\mu\mu\gamma$  channel are required to have opposite electric charge. This requirement is not used in the  $ee\gamma$  channel due to a nonnegligible probability to misreconstruct the charge of an electron candidate because of an energetic bremsstrahlung. The leading electron (muon) is required to have  $p_T > 65$  (52) GeV and  $|\eta| < 2.5$  (2.4). The subleading lepton is required to have  $p_T > 10$  GeV and to be found in the same pseudorapidity range as the leading lepton. The photon in the  $ee\gamma$  ( $\mu\mu\gamma$ ) channel is required to satisfy  $p_T > 65$  (40) GeV and  $|\eta| < 2.5$ . Electrons and photons in the ECAL barrel-endcap transition region ( $1.44 < |\eta| < 1.57$ ) are excluded from the analysis. In the  $ee\gamma$  channel, the  $p_T$  thresholds on the electrons and photons in the ECAL endcap region are increased to 70 GeV, in order to ensure a fully efficient trigger. Photons are required to be separated from lepton candidates by  $\Delta R > 0.4$ , to reduce the background from final-state radiation in  $Z \rightarrow \ell\ell$  events. The invariant mass of the dilepton system is required to be  $50 < m_{\ell\ell} < 130$  GeV. The minimum dilepton mass requirement suppresses contributions from  $pp \rightarrow \gamma\gamma^*$  events, where an internal conversion of a photon

produces a lepton pair. Finally, we require the ratio of the photon  $p_T$  to  $m_{Z\gamma}$  to be greater than 0.27. This requirement suppresses backgrounds due to jets misidentified as photons, without significant loss in the signal efficiency and without introducing a bias in the  $m_{Z\gamma}$  spectrum. We search for resonances in the  $m_{Z\gamma}$  spectrum above 300 (250) GeV in the  $ee\gamma$  ( $\mu\mu\gamma$ ) channel.

## 5.4 Nonresonant Signal Selection

In the nonresonant signal analysis, events are required to have two same-flavor leptons and a photon. The two leptons are not required to be of opposite-sign charge because this would result in a signal efficiency loss of a few % at high lepton  $p_T$ , especially for the  $ee\gamma$  channel [79], whereas the background arising from events with same-sign dileptons is minimal. Electrons and photons are required to have  $p_T > 35$  GeV and to be within the region  $|\eta| < 2.5$ , with those in the ECAL barrel-endcap transition region being excluded from the analysis. Muons must have  $p_T > 35$  GeV and be within  $|\eta| < 2.4$ . The selected leptons must be separated from the photon by  $\Delta R > 0.7$ . In addition, the invariant mass of the two leptons  $m_{\ell\ell}$  is required to be larger than 116 GeV in order to suppress the dominant background contribution from Z boson production (Z boson veto criteria).

# Chapter 6

## Background Modeling

### 6.1 Background for the Resonant Signal Search

#### 6.1.1 Background Distribution in $m_{Z\gamma}$

Simulations indicate that 80–90% of the background remaining after the full event selection is from SM Z boson production accompanied by initial-state photon radiation, with the remainder mostly from Z +jets events, with a jet misreconstructed as a photon. The background  $m_{Z\gamma}$  distributions fall steeply and smoothly with increasing mass.

The background is measured directly in data, through unbinned maximum-likelihood fits to the observed  $m_{Z\gamma}$  distributions, performed separately in each channel. The background in each channel is parametrized with an empirical function. Different families of functions inspired by the ones used in searches for beyond-the-SM phenomena in the dijet, multijet, diphoton, and VV channels at hadron colliders are evaluated in the signal region using simulation:

- ‘dijet’:  $\frac{dN}{dm_{Z\gamma}}(m_{Z\gamma}) = P_0 m_{Z\gamma}^{p_n(\ln m_{Z\gamma})}$

- ‘expow’:  $\frac{dN}{dm_{Z\gamma}}(m_{Z\gamma}) = P_0 e^{p_n(m_{Z\gamma})} m_{Z\gamma}^b$
- ‘invpow’:  $\frac{dN}{dm_{Z\gamma}}(m_{Z\gamma}) = P_0 (1 + p_n(m_{Z\gamma}))^a$
- ‘invpowlin’:  $\frac{dN}{dm_{Z\gamma}}(m_{Z\gamma}) = P_0 (1 + am_{Z\gamma})^{b+p_n(m_{Z\gamma})}$
- ‘moddijet’:  $\frac{dN}{dm_{Z\gamma}}(m_{Z\gamma}) = P_0 m_{Z\gamma}^{a+b \log m_{Z\gamma}} (1 - p_n(m_{Z\gamma}))^c$
- ‘pow’:  $\frac{dN}{dm_{Z\gamma}}(m_{Z\gamma}) = P_0 (p_n(m_{Z\gamma}))^a$
- ‘sumexp’:  $\frac{dN}{dm_{Z\gamma}}(m_{Z\gamma}) = P_0 \sum_{i=0}^n c_i e^{a_i m_{Z\gamma}}$

where  $p_n$  is the  $n$ -th other polynomial. The choice of the order within a family of fitting functions for the background distribution is made independently in each channel using the Fisher  $F$ -test [80], which balances the quality of the fit against the number of parameters. The results of the Fisher  $F$ -test are shown in Table 6.1.

Table 6.1: Results of the Fisher  $F$ -test

Functional family	Best order ( $n$ )
‘dijet’	1
‘expow’	3
‘invpow’	1
‘invpowlin’	1
‘moddijet’	1
‘pow’	1
‘sumexp’	3

The choice among the families of functions is optimized based on the results of the bias test described below. The first-order ‘dijet’ function [81] was chosen

for both the  $ee\gamma$  and  $\mu\mu\gamma$  channels:

$$\frac{dN}{dm_{Z\gamma}}(m_{Z\gamma}) = P_0 m_{Z\gamma}^{P_1 + P_2(\ln m_{Z\gamma})}, \quad (6.1)$$

The observed  $m_{Z\gamma}$  invariant mass spectra in data are shown in Fig. 6.1 for the  $ee\gamma$  (left) and  $\mu\mu\gamma$  (right) channels. The results of the fits and their uncertainties at 68% confidence level (CL) are shown by the lines and the shaded bands, respectively.

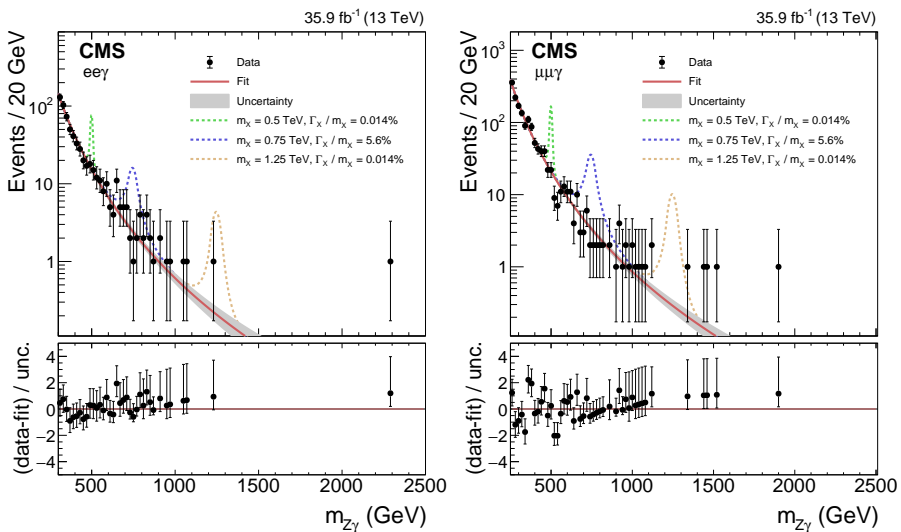


Figure 6.1: Observed  $m_{Z\gamma}$  invariant mass spectra in the  $ee\gamma$  (left) and  $\mu\mu\gamma$  (right) channels. The best fits to the background-only hypotheses are represented by the red lines, with their 68% CL uncertainty bands given by the gray shadings. Several narrow and broad signal benchmarks with arbitrary normalization are shown on top of the background prediction with the dashed lines. The lower panels show the difference between the data and the fits, divided by the uncertainty, which includes the statistical uncertainties in the data and the fit. For bins with a small number of entries, the error bars correspond to the Garwood confidence intervals [82].

### 6.1.2 Bias Estimation

The absence of significant bias in the fit to background is verified by generating a large number of pseudo-experiments using the simulated background shapes, fitting them with different background models, and measuring the difference between the input and fitted background yields in various  $m_{Z\gamma}$  windows within the entire search range. A pull variable is defined in each window by the difference between the input and fitted yields, divided by the combined statistical uncertainties in the data and the fit. Tested median pull distributions are shown in Fig. 6.2.

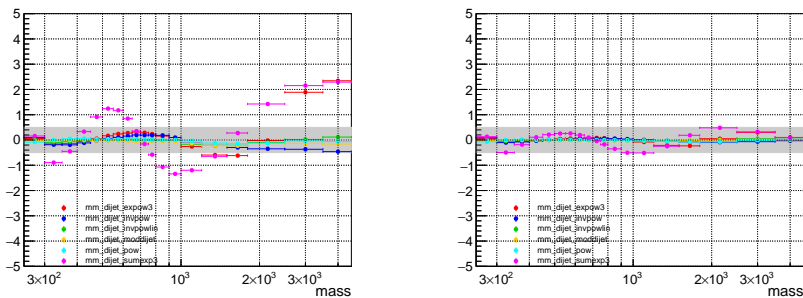


Figure 6.2: Median pull distributions before (left) and after (right) introducing the additional uncertainty.

If the absolute value of the median in the pull distribution is found to be  $>0.5$ , an additional uncertainty is assigned to the background parametrization. A modified pull distribution is then constructed, increasing the statistical uncertainty by an extra term, denoted as the bias term. The bias term is parametrized as a smooth function of  $m_{Z\gamma}$  and tuned to make the absolute value of the median of the modified pull distribution to be  $<0.5$  in all mass windows.

This additional uncertainty is included in the likelihood function by adding

to the background model a component with a distribution that is the same as the signal, but a normalization coefficient distributed as a Gaussian of mean zero, and a width equal to the integral of the bias term over the signal mass window, defined as the full width at half maximum. The inclusion of this additional component takes into account the possible mismodeling of the background shape. The bias term corresponds to  $\approx 0.3$  events/GeV at  $m_{Z\gamma} = 400$  GeV and smoothly falls to  $\approx 2 \times 10^{-4}$  events/GeV around  $m_{Z\gamma} = 2$  TeV.

## 6.2 Background for the Nonresonant Signal Search

### 6.2.1 Major Backgrounds

The major backgrounds in the nonresonant analysis originate from SM processes with final states consisting of two prompt leptons and a prompt photon or a jet misidentified as a photon. The expected fraction of background events that have a jet misidentified as a lepton is less than 1% for both channels [83], therefore this background source is not considered in the analysis. Backgrounds associated with a prompt photon are estimated using simulation, while the yield of those associated with a jet is derived from the data.

The dominant background arises from Drell–Yan process accompanied by a prompt photon ( $DY+\gamma$ ), which has a signature similar to the signal. Within the detector acceptance, Z boson production dominates the process, and its contribution is efficiently suppressed by applying the Z boson veto criteria described in Section 5.4. The fraction of  $DY+\gamma$  events after the event selection is approximately 70% of the background. Another prompt photon background comes from top quark pair production in association with a photon ( $t\bar{t}+\gamma$ ). These events form approximately 10% of the background. In addition, triboson processes such as  $WW\gamma$ ,  $WZ\gamma$ , and  $ZZ\gamma$  ( $VV\gamma$ ) also give rise to 5% of the background. The prompt photon background processes are all estimated using

MC simulation.

The other major background contribution consists of events with two prompt leptons and a photon that originates from a jet, hereafter referred to as the jet background. The estimation of this background is derived from data in a control region composed of events with two leptons and a photon passing all the kinematic requirements and lepton identification criteria defined in the event selection but failing the photon identification. The events in the control region, scaled by a weight factor derived from the misidentification rate of photon candidates from jets, provide the jet background prediction in the signal region.

### 6.2.2 Misidentified Photon Background Estimation

The misidentification rate is measured using data in a sideband ( $50 < m_{\ell\ell} < 116$  GeV) of the dilepton mass distribution in the signal region ( $m_{\ell\ell} > 116$  GeV). The photon identification is not required for events in the sideband, thereby the data in the sideband are enriched with Z boson events associated with a photon originating from a jet. To remove prompt photon contamination in the data, the distribution of the MVA variable used for the photon identification is employed, fitting the MVA variable distribution of the data events with template distributions for prompt photons and photons originating from jets. The MVA distribution of simulated prompt photon background events in the sideband is used as the template distribution for prompt photons. The template for photons originating from jets is obtained from a data sample enriched with W+jets events, where the W boson decays leptonically and a jet supplies a photon candidate. Events in the sample are required to have a muon of  $p_T > 35$  GeV,  $p_T^{\text{miss}} > 35$  GeV, transverse mass  $\sqrt{2p_T^{\text{miss}}p_T^\mu[1 - \cos \Delta\phi(\vec{p}_T^{\text{miss}}, \vec{p}_T^\mu)]}$  between 50 and 110 GeV, and a photon candidate.

The misidentification rate is evaluated in several photon  $p_T$  bins separately for the barrel and endcaps of ECAL. The measured misidentification rate ranges from 2 (3)% at  $p_T = 35$  GeV to 0.2 (0.4)% at  $p_T = 1$  TeV in the barrel (endcaps), as shown in Fig. 6.3. In the signal region, the estimated fraction of events arising from background with a jet misidentified as a photon is in the range 5–15%, depending on the photon  $p_T$ , as shown in Fig. 6.4.

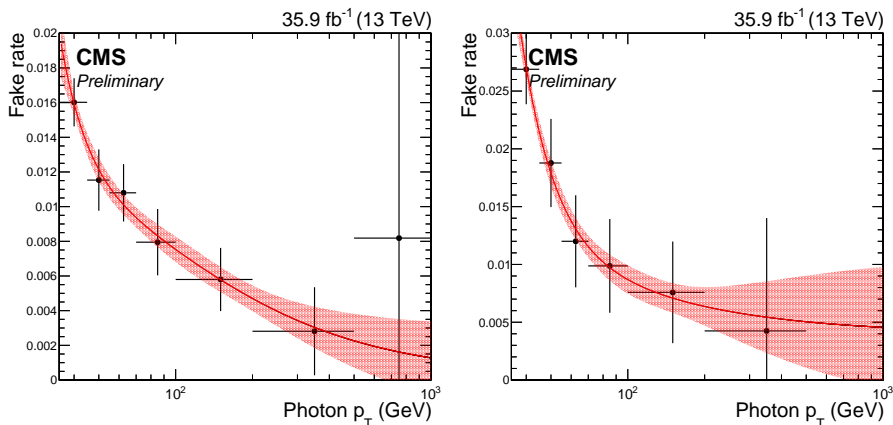


Figure 6.3: The misidentification rate as a function of photon  $p_T$  in the barrel (left) and endcap (right) regions. The error bars denote statistical uncertainties of bin-by-bin measurement and the error bands denote  $1\sigma$  bands of fitting uncertainties. A polynomial function of photon  $p_T$  (red line) is fitted to each histogram and the value is obtained by the value of the fitted function at a given photon  $p_T$ .

The kinematic distributions of the parent jets of the misidentified photons in the control region and those of the signal region are not identical in the same photon  $p_T$  range, owing to  $H/E$  and isolation requirements in the MVA identification. Consequently, the  $p_T$  distributions of leptons, which are correlated with the recoil of the jet in the same event, are different in the signal region and the control region. Therefore, an appropriate correction must be

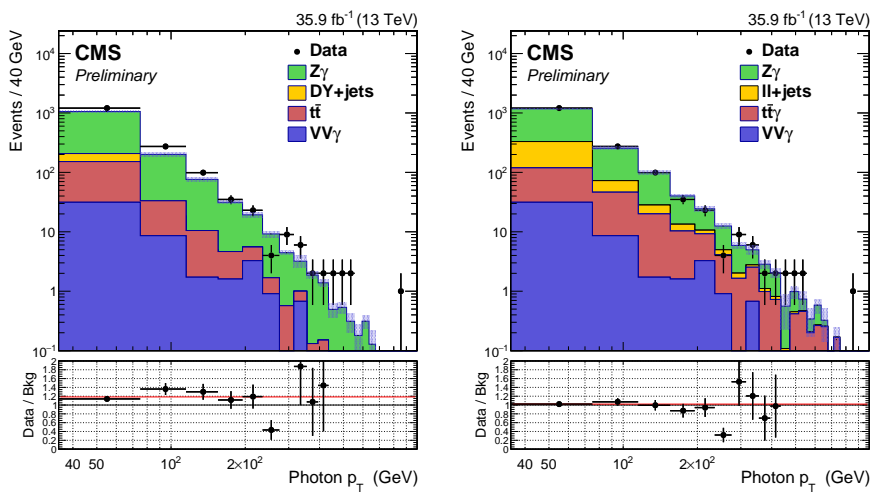


Figure 6.4: Photon  $p_T$  distributions of the data events and background predictions in the signal region. The background prediction in the left plot is purely based on simulation whereas the jet estimate from data is used for the right plot.

applied to the estimate of the lepton  $p_T$  distribution obtained by scaling the control region by a weight factor based on the misidentification rate.

Using the  $p_T$  of the dilepton pair as a proxy of the jet recoil, the dilepton  $p_T$  distribution of the jet background estimate is reweighted to match the correct shape of the dilepton  $p_T$  distribution of the jet background events in the signal region. The shape is directly taken from data in the signal region, removing prompt photon contamination using simulated events. The reweighting is done for separate photon  $p_T$  bins used for the misidentification rate measurement, in order to retain the yield and the photon  $p_T$  spectrum obtained from the previous step.

To validate the estimation procedures, closure tests are performed by applying the same method to derive background on simulated events, and the observed discrepancies are taken as estimates of the associated systematic uncertainties. After the correction, the lepton kinematic distributions from the total background prediction including the corrected jet background obtained from control samples in data are in good agreement with the distributions in data, as shown in Fig. 6.5 and Fig. 6.6.

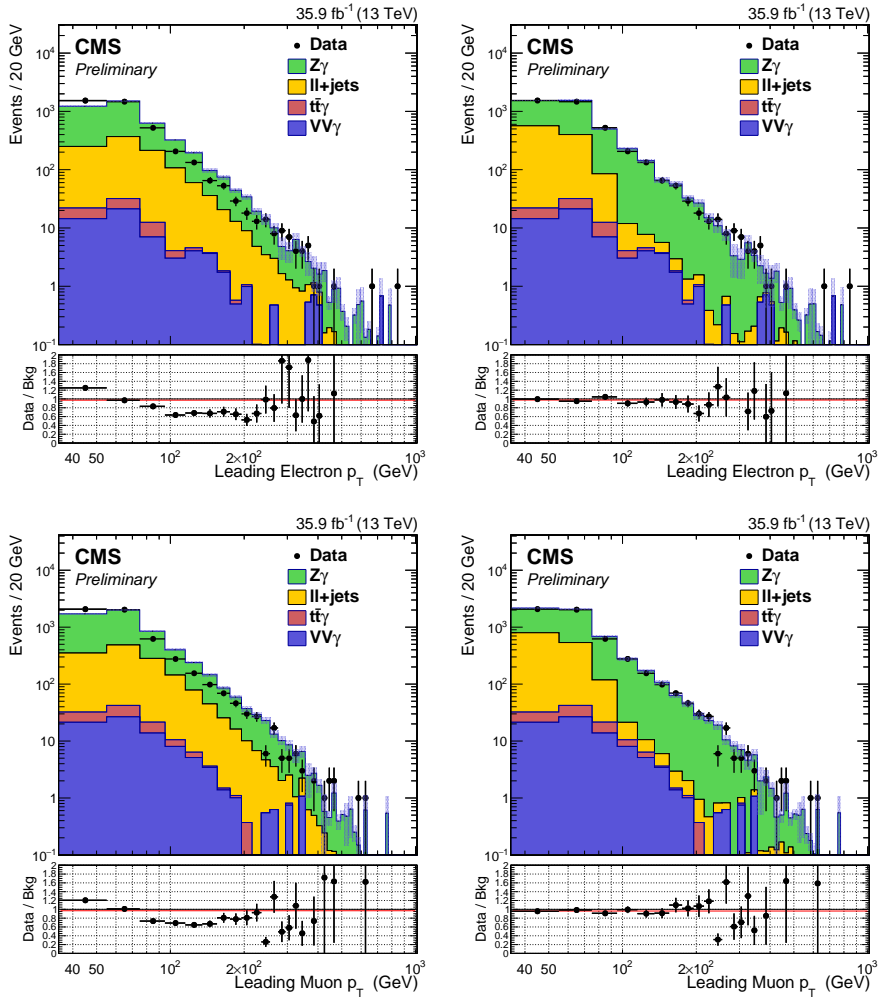


Figure 6.5: The  $p_T$  distributions of leading electrons (upper) and leading muons (lower), using the jet background estimates from data before (left) and after (right) dilepton  $p_T$  reweighting.

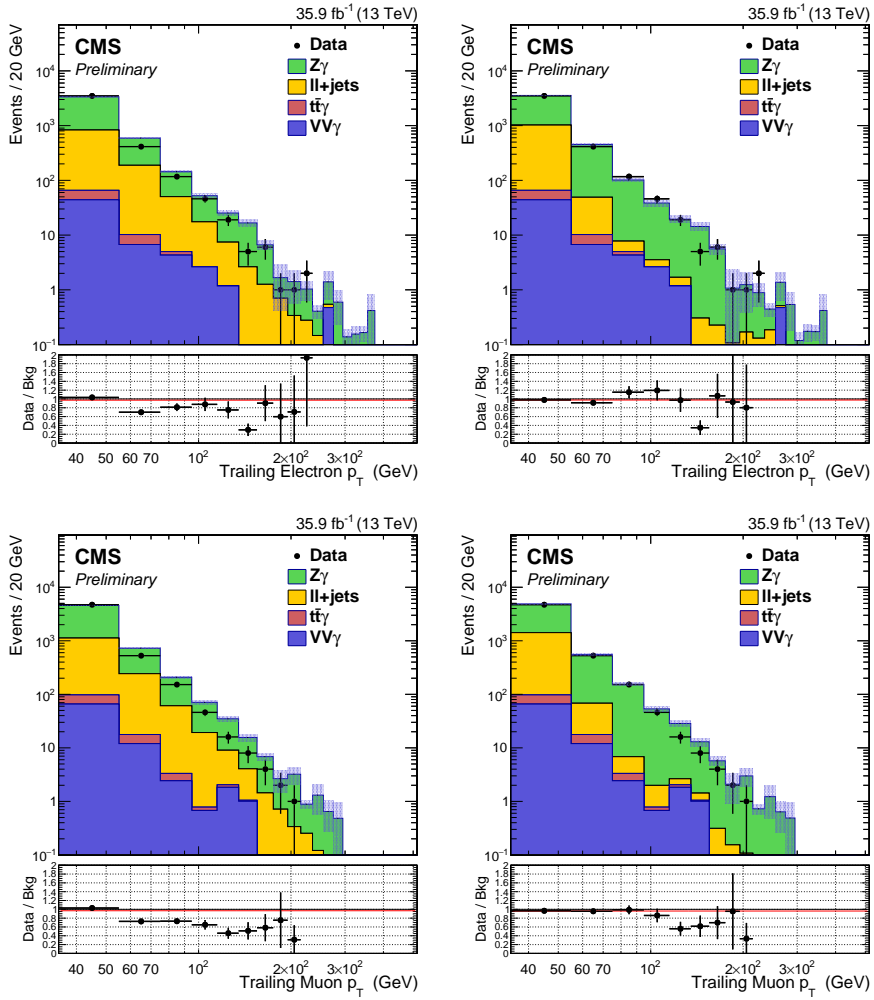


Figure 6.6: The  $p_T$  distributions of subleading electrons (upper) and subleading muons (lower), using the jet background estimates from data before (left) and after (right) dilepton  $p_T$  reweighting.

# Chapter 7

## Signal Modeling

### 7.1 Resonant Signal

#### 7.1.1 Signal Distribution in $m_{Z\gamma}$

The signal distribution in  $m_{Z\gamma}$  is obtained from the generated events that pass the full selection. The signal shape is parametrized with a Gaussian core and two power-law tails, namely an extended form of the Crystal Ball (CB) function [84]. We find this functional form to provide an adequate description for both narrow and broad signals in the entire mass range used in the analysis. To derive the signal shapes for the intermediate mass values where simulation points are not available, a linear morphing [85] of the shapes obtained from the simulation is used. The fits to the simulation are shown in Figs. 7.1–7.6. The typical mass resolution for narrow-width signal events is 1% for the  $ee\gamma$  channel, 1–2% for the  $\mu\mu\gamma$  channel, depending on the mass of the resonance.

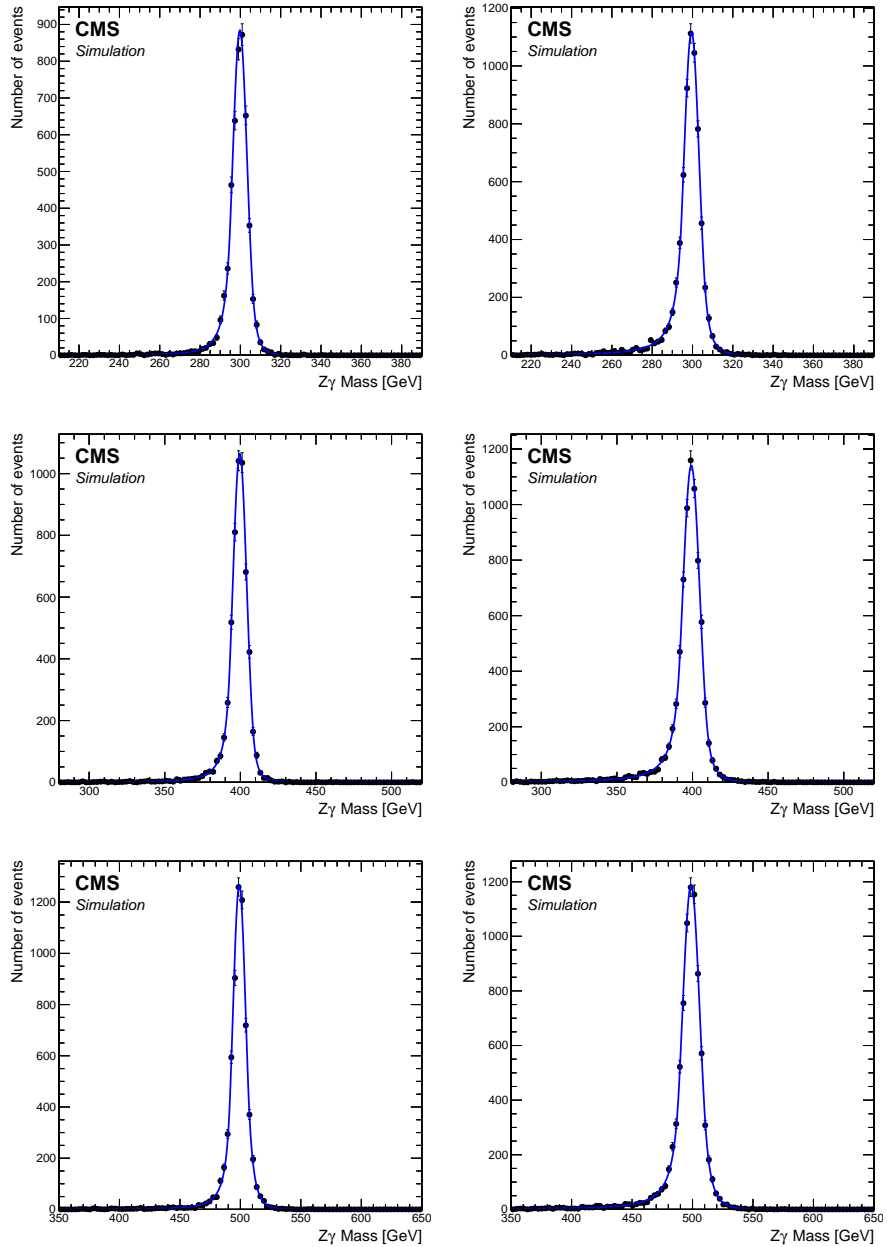


Figure 7.1: The CB fits to the signal simulation for the  $ee\gamma$  (left column) and  $\mu\mu\gamma$  (right column) channels for narrow resonances of mass 300 (upper row), 400 (middle row), and 500 GeV (lower row).

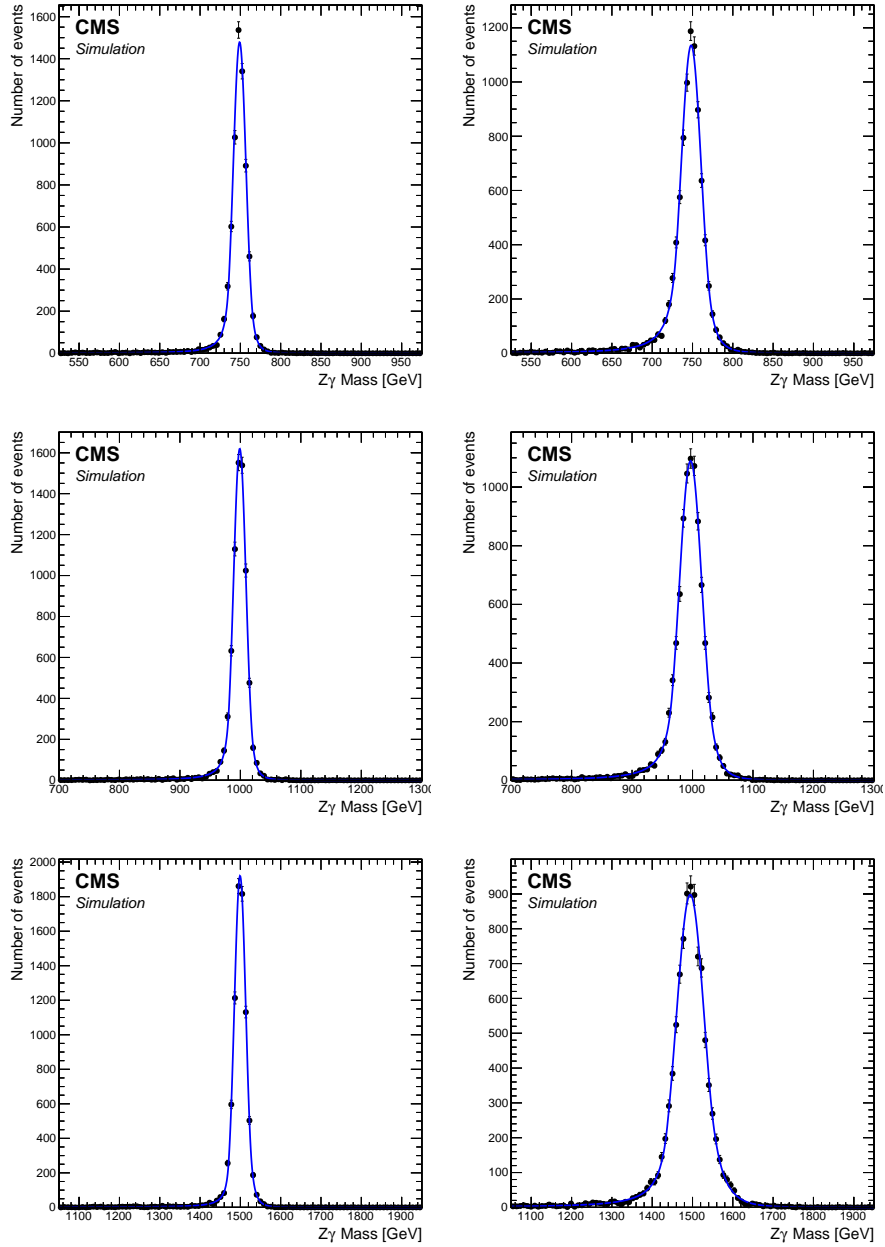


Figure 7.2: The CB fits to the signal simulation for the  $ee\gamma$  (left column) and  $\mu\mu\gamma$  (right column) channels for narrow resonances of mass 750 (upper row), 1000 (middle row), and 1500 GeV (lower row).

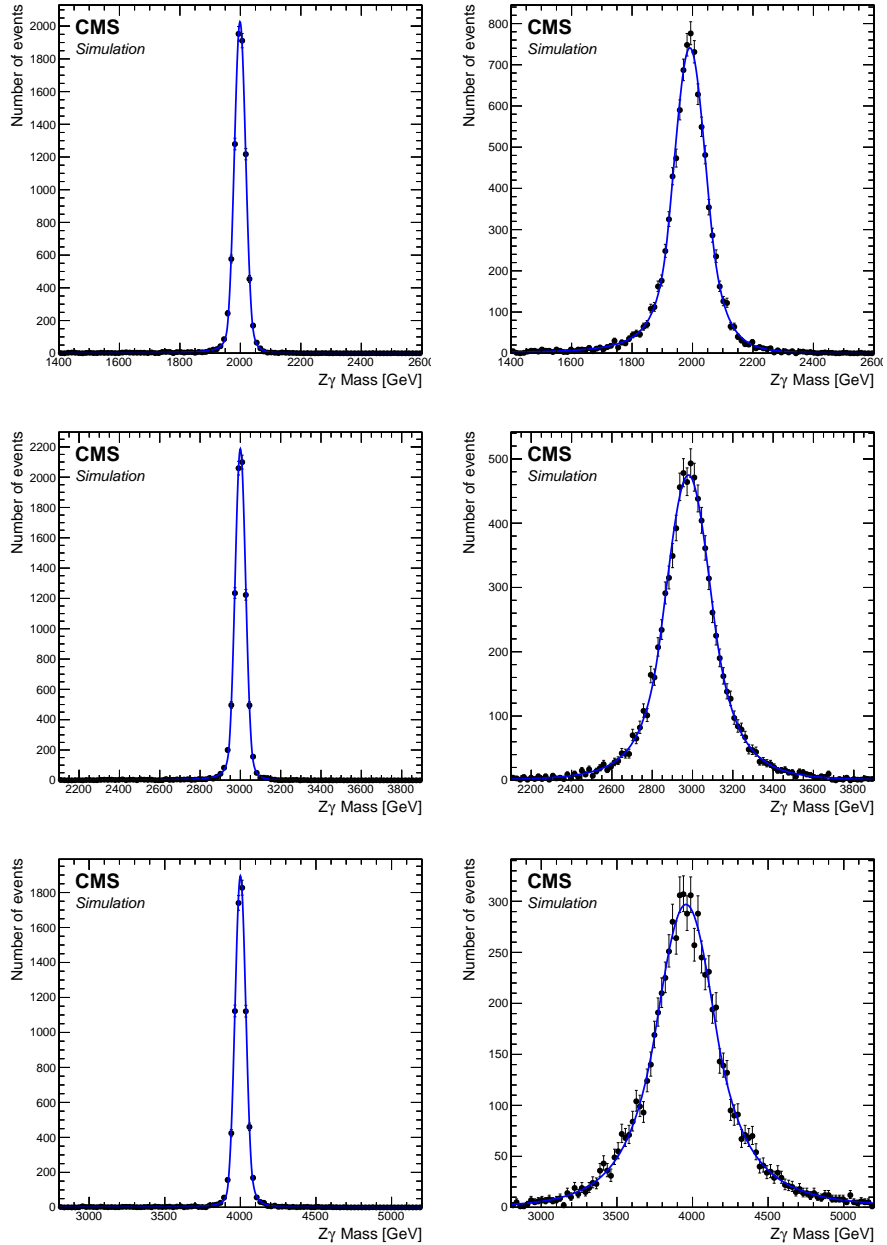


Figure 7.3: The CB fits to the signal simulation for the  $ee\gamma$  (left column) and  $\mu\mu\gamma$  (right column) channels for narrow resonances of mass 2000 (upper row), 3000 (middle row), and 4000 GeV (lower row).

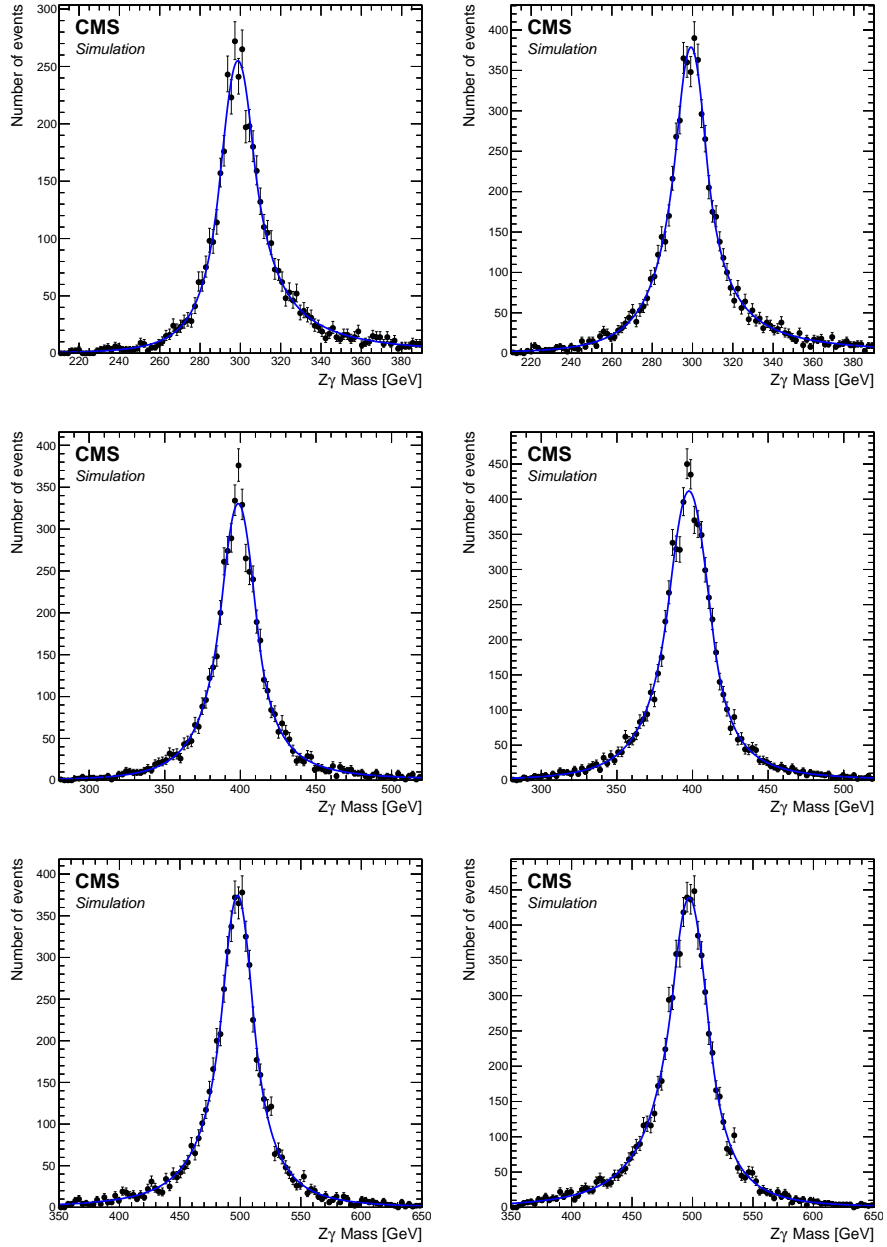


Figure 7.4: The CB fits to the signal simulation for the  $ee\gamma$  (left column) and  $\mu\mu\gamma$  (right column) channels for broad resonances of mass 300 (upper row), 400 (middle row), and 500 GeV (lower row).

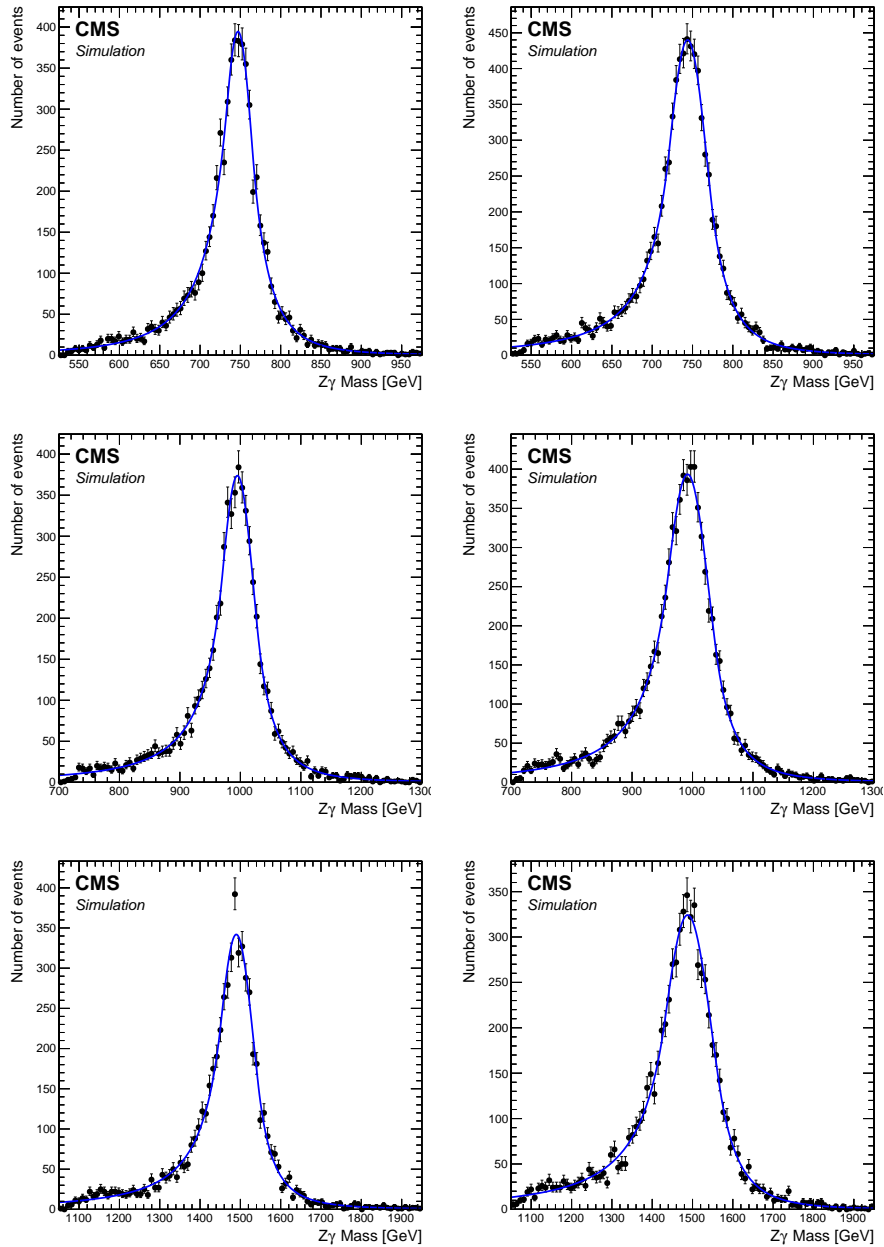


Figure 7.5: The CB fits to the signal simulation for the  $ee\gamma$  (left column) and  $\mu\mu\gamma$  (right column) channels for broad resonances of mass 750 (upper row), 1000 (middle row), and 1500 GeV (lower row).

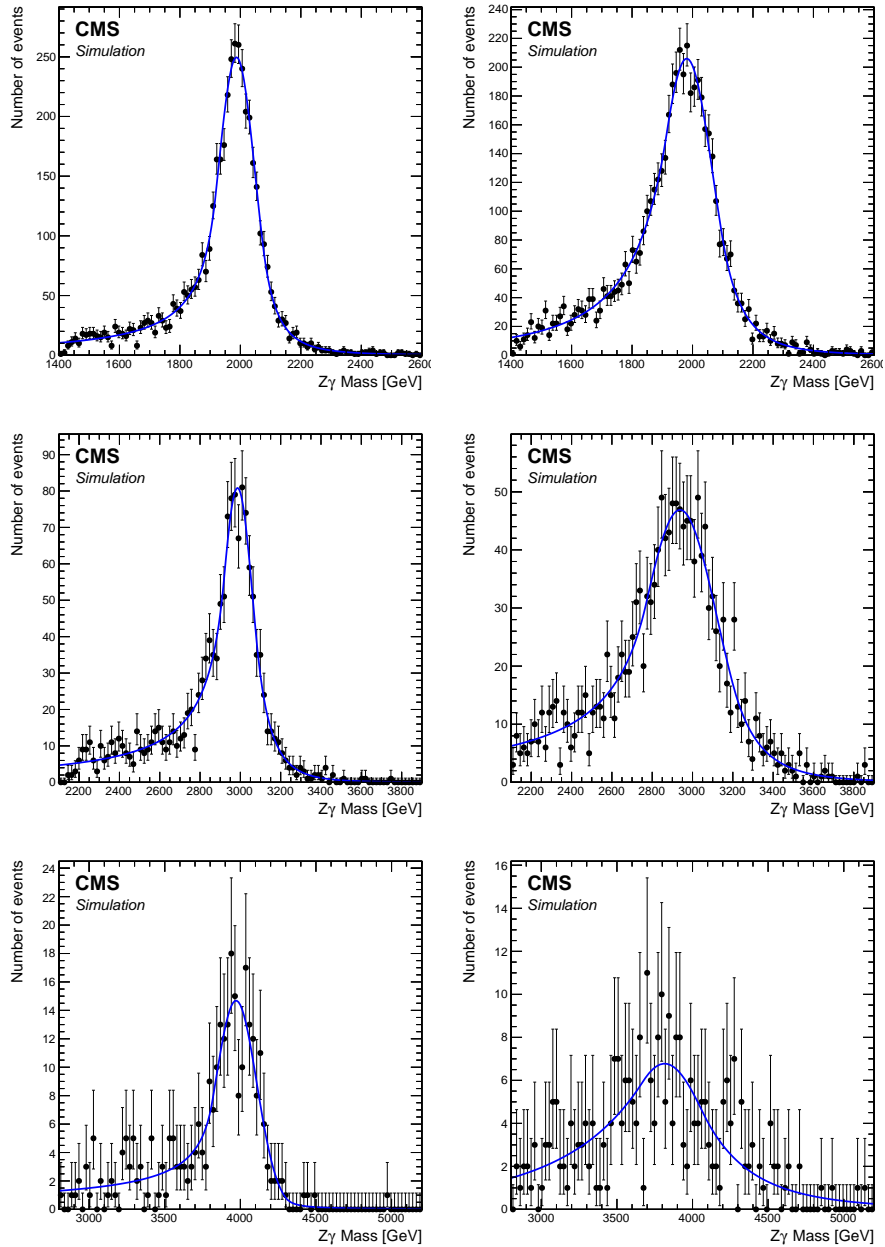


Figure 7.6: The CB fits to the signal simulation for the  $ee\gamma$  (left column) and  $\mu\mu\gamma$  (right column) channels for broad resonances of mass 2000 (upper row), 3000 (middle row), and 4000 GeV (lower row).

### 7.1.2 Signal Selection Efficiency and Detector Acceptance

The product of signal acceptance and efficiency ( $A \epsilon_{\text{sig}}$ ) is shown in Fig. 7.7. Narrow resonance  $A \epsilon_{\text{sig}}$  in the  $ee\gamma$  ( $\mu\mu\gamma$ ) channel rises from about 27 (42)% at  $m_{Z\gamma} = 0.35$  TeV to about 46 (55)% at  $m_{Z\gamma} = 2$  TeV, and remains steady until 4 TeV. For a broad resonance  $A \epsilon_{\text{sig}}$  is similar to the narrow-resonance case up to 2 TeV. At large resonance masses ( $>2$  TeV), however, the effect of rapidly falling PDFs introduces a lower tail in the signal mass distribution. The exact characteristics of this tail are quite sensitive to the resonant line shape. We therefore truncate the mass distribution of the resonance to correspond to the core of the line shape, defined as a window centered on the maximum of the CB function with a width given by  $\pm 5$  times the CB function parameter  $\sigma$ , describing the standard deviation of its Gaussian core. The tails outside this window are conservatively discarded in the signal acceptance calculations and when fitting the data. As a result,  $A \epsilon_{\text{sig}}$  falls to 2% at 4 TeV for the  $ee\gamma$  and  $\mu\mu\gamma$  events.

## 7.2 Nonresonant Signal

### 7.2.1 Search Window in $m_{\ell\gamma}^{\text{min}}-m_{\ell\gamma}^{\text{max}}$

The production of an excited lepton involves two SM leptons in the final state, one from the excited lepton decay and another from CI, and therefore there are two possible pairings of a lepton with the photon. The corresponding two invariant masses are referred to as  $m_{\ell\gamma}^{\text{min}}$  and  $m_{\ell\gamma}^{\text{max}}$ . The  $m_{\ell\gamma}^{\text{min}}$  and  $m_{\ell\gamma}^{\text{max}}$  distributions of observed events along with the background prediction in the signal region are shown in Fig. 7.8.

A search window is set in the two-dimensional distribution of  $m_{\ell\gamma}^{\text{max}}$  versus  $m_{\ell\gamma}^{\text{min}}$ . For  $\ell^*$  events, either  $m_{\ell\gamma}^{\text{min}}$  or  $m_{\ell\gamma}^{\text{max}}$  corresponds to the reconstructed

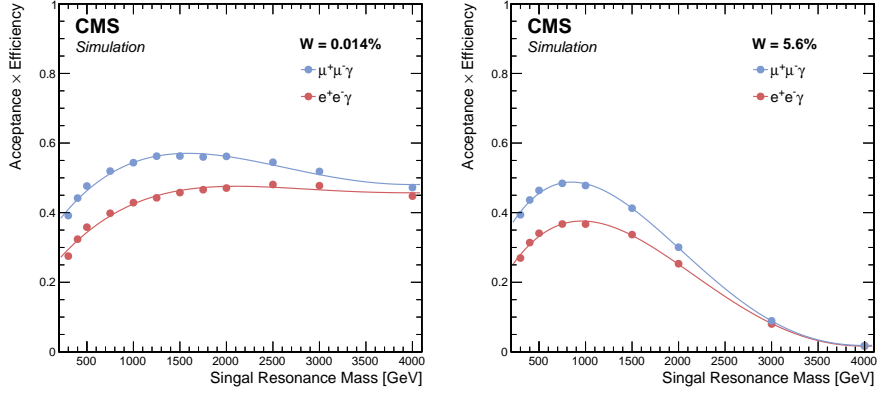


Figure 7.7: The product of signal acceptance and efficiency as a function of the generated resonance mass for the  $ee\gamma$  (red) and  $\mu\mu\gamma$  (blue) channels, for narrow (left) and broad (right) resonances. Each marker denotes the value measured from the simulated signal sample at a given mass point, and the lines represent polynomial fits to the measured values.

invariant mass of  $\ell^*$ . Therefore, the mass resonance of the signal is concentrated in the shape of a reflected “L” as shown in Fig. 7.9. On the other hand, background events have no such correlation in  $m_{\ell\gamma}^{\min}$  and  $m_{\ell\gamma}^{\max}$  in the low mass region below 1 TeV. The distribution of the dominant  $DY+\gamma$  background is shown in Fig. 7.10. This clear distinction between signal and background events in the distribution of  $m_{\ell\gamma}^{\max}$  versus  $m_{\ell\gamma}^{\min}$  is used to define L-shaped search windows enhancing the discrimination between signal and background.

For low signal masses,  $m_{\ell^*} \leq 1$  TeV, setting an L-shaped search window significantly improves a discrimination against the background with only a small loss in the signal acceptance. Therefore, the search window for  $m_{\ell^*} \leq 1$  TeV is set to be a narrow L-shape centered at  $m_{\ell^*}$ , consisting of lower and upper thresholds of  $m_{\ell\gamma}^{\min}$  and  $m_{\ell\gamma}^{\max}$  as shown in Fig. 7.9. The thresholds are optimized for the best expected exclusion limit, which also provides the optimal

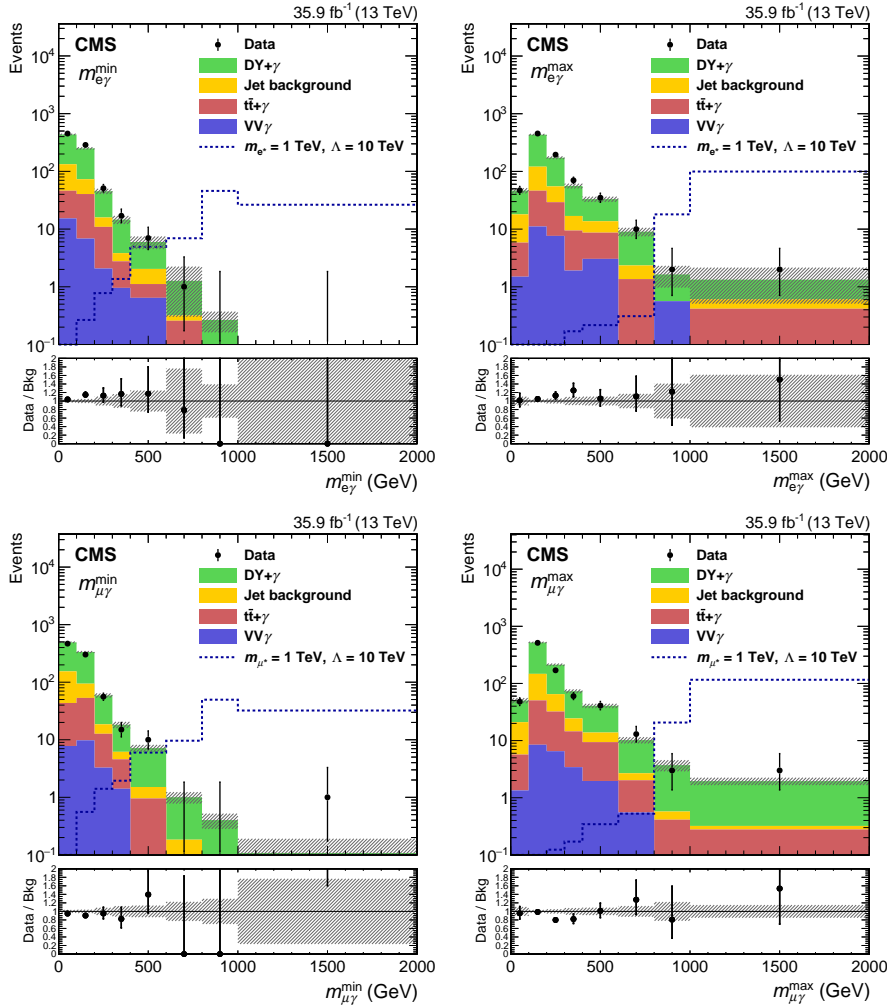


Figure 7.8: The distributions of  $m_{\ell\gamma}^{\min}$  (left column) and  $m_{\ell\gamma}^{\max}$  (right column) in the  $ee\gamma$  channel (upper row) and the  $\mu\mu\gamma$  channel (lower row). The points with error bars denote the data and the stacked histograms show the predictions for each of the backgrounds. The uncertainty bands of the SM prediction includes only statistical uncertainties. Signal events for  $m_{\ell^*} = 1 \text{ TeV}$  at  $\Lambda = 10 \text{ TeV}$  are also shown as dotted lines. The last bin of each distribution includes overflow events.

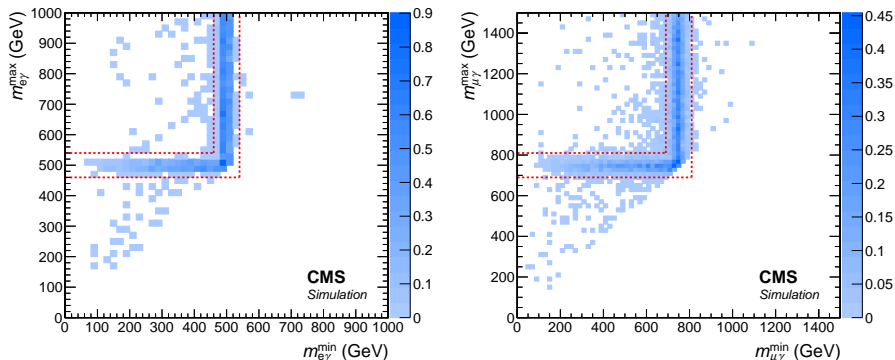


Figure 7.9: The two-dimensional distributions of  $m_{\ell\gamma}^{\max}$  versus  $m_{\ell\gamma}^{\min}$  of excited electrons with a mass of 500 GeV (left) and of excited muons with a mass of 750 GeV (right), after the event selection, normalized to the expected signal cross section at  $\Lambda = 10$  TeV. The red dashed lines denote the boundary of the L-shaped search window.

discovery potential. The impact of the energy scale and resolution uncertainties on the signal acceptance is taken into account for the optimization. The optimized thresholds have values that are within  $\pm 8\%$  of the simulated mass for  $e^*$ , and within ranges that vary from  $\pm 4.5\%$  to  $\pm 8\%$  of the simulated mass for  $\mu^*$ .

The search windows defined for  $m_{\ell^*} > 1$  TeV, where the background contribution is expected to be negligible, only impose the lower  $m_{\ell\gamma}^{\max}$  threshold of 1 TeV, thereby maximizing the signal acceptance.

### 7.2.2 Signal Selection Efficiency and Detector Acceptance

The product of signal acceptance and efficiency has been measured from the simulated signal samples, and ranges from 30 to 49% and from 33 to 59% for excited electrons and muons, respectively. To determine  $A \epsilon_{\text{sig}}$  for mass points other than those of the simulated samples, a polynomial fit to the dependence

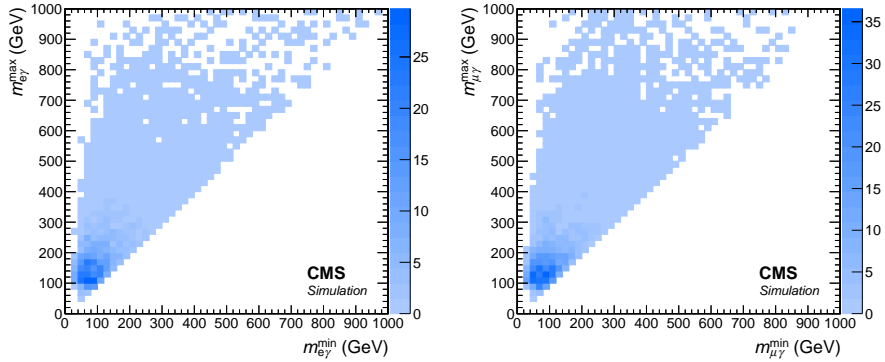


Figure 7.10: The two-dimensional distributions of  $m_{\ell\gamma}^{\max}$  versus  $m_{\ell\gamma}^{\min}$  of  $DY+\gamma$  background events in the  $ee\gamma$  (left) and  $\mu\mu\gamma$  (right) channels, after the event selection, normalized to the cross section for  $DY+\gamma$  production.

on  $m_{\ell^*}$  is used for interpolation, as shown in Fig. 7.11.

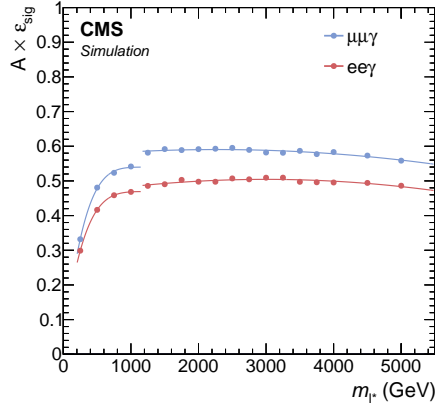


Figure 7.11: The product of signal acceptance and efficiency as a function of the generated excited lepton mass for the  $ee\gamma$  (lower) and  $\mu\mu\gamma$  (upper) channels. Each marker denotes the value measured from the simulated signal sample at a given mass point, and the lines represent polynomial fits to the measured values.

# Chapter 8

## Systematic Uncertainties

### 8.1 Systematic Uncertainties for the Resonant Signal Search

The statistical uncertainty in the fits of the background function to data is taken for the background uncertainty in all channels. The following systematic uncertainties in the signal are defined below, and summarized in Table 8.1:

- Integrated luminosity: the uncertainty in the CMS integrated luminosity is based on cluster counting in the silicon pixel detector and amounts to 2.5% [86].
- Pileup: the uncertainty due to the pileup description in the signal simulation, evaluated by changing the total inelastic cross section governing the average multiplicity of pileup interactions by  $\pm 5\%$  [87], translates to a 1.0% uncertainty in the signal acceptance in all channels.
- Trigger: the uncertainty due to the trigger efficiency differences in data and simulation in the  $\ell\ell\gamma$  analysis is estimated with dedicated studies

with leptons from Z boson decays and amounts to 1.0(3.5)% for the  $ee\gamma$  ( $\mu\mu\gamma$ ) channel.

- Lepton efficiency: the systematic uncertainty due to the differences in the lepton identification efficiency in data and simulation is evaluated with  $Z \rightarrow ee$  ( $\mu\mu$ ) events and amounts to 2.5(2.0)% in the  $ee\gamma$  ( $\mu\mu\gamma$ ) channel.
- Photon efficiency: the systematic uncertainty due to the differences in the photon identification efficiency between data and simulation is evaluated with  $Z \rightarrow ee$  events in which the electrons are used as proxies for photons, and amounts to 1.5% [88, 89].
- PDFs: a 1.0–3.5% uncertainty in the signal efficiency that takes into account the variation in the kinematic acceptance of the analysis is estimated using replicas of the NNPDF3.0 set, following the PDF4LHC prescription [90]. The uncertainty in the signal cross section due to the PDF choice is not considered.
- Electron and photon energy scale and resolution: the electron and photon energy scale is known with 0.1–5.0% precision, depending on the energy. This uncertainty is based on the accuracy of the energy scale at the Z boson peak and its extrapolation to higher masses, and translates into a 0.2–4.6 (0.1–2.3)% correlated uncertainty in the  $m_{Z\gamma}$  scale in the  $ee\gamma$  ( $\mu\mu\gamma$ ) channel. The uncertainty in the electron and photon energy resolution based on the Gaussian smearing evaluated at the Z boson peak translates to a 10 (5)% uncertainty in the  $m_{Z\gamma}$  resolution in the  $ee\gamma$  ( $\mu\mu\gamma$ ) channel.

- Muon momentum scale and resolution: the muon momentum scale is measured with 0.1–5.0% precision up to  $p_T = 200$  GeV, with an additional 0.1–6.0% uncertainty at higher values, resulting in a 0.1–4.6% uncertainty in the  $m_{Z\gamma}$  mass scale in the  $\mu\mu\gamma$  channel. A 10% uncertainty in the  $m_{Z\gamma}$  resolution in the  $\mu\mu\gamma$  channel is conservatively assigned to account for the uncertainty in the muon momentum resolution.

Table 8.1: Summary of the systematic uncertainties in the signal yield (upper part of the table) or shape (lower part of the table). A dash indicates that the uncertainty does not apply.

Source	$ee\gamma$ channel (%)	$\mu\mu\gamma$ channel (%)
Integrated luminosity	2.5	2.5
Pileup	1	1
Trigger	1	3.5
Lepton efficiency	2.5	2
Photon efficiency	1.5	1.5
PDFs	1–3.5	1–3.5
$e/\gamma$ energy scale	0.2–4.6	0.1–2.3
$e/\gamma$ energy resolution	10	5
Muon momentum scale	—	0.1–4.6
Muon momentum resolution	—	10

## 8.2 Systematic Uncertainties for the Nonresonant Signal Search

The systematic uncertainties in the signal and the background yields are summarized in Table 8.2. The statistical uncertainties in the data and the simu-

lated samples used for the background estimation are dominant. These uncertainties are expected to be reduced in future by producing simulated samples enriched with high  $p_T$  photons. The statistical uncertainties in the simulated signal samples used to measure  $A\epsilon_{\text{sig}}$  are negligible and therefore not considered in the analysis. The values of the systematic uncertainties for the jet background estimate coming from control samples in data are also large compared to other systematic uncertainties, but their impact on the sensitivity of the search is small since the jet background makes up only 5–15% of the total background.

Table 8.2: Summary of the systematic uncertainties (in %) in the signal yield, the prompt photon background prediction, and the jet background prediction.

Source	ee $\gamma$ channel (%)			$\mu\mu\gamma$ channel (%)		
	Signal	Prompt $\gamma$ bkg	Jet bkg	Signal	Prompt $\gamma$ bkg	Jet bkg
Integrated luminosity	2.5	2.5	—	2.5	2.5	—
Pileup	1	1	—	1	1	—
Trigger	1	1	—	2	2	—
Lepton efficiency	2.5	2.5	—	2	2	—
Photon efficiency	1.5	1.5	—	1.5	1.5	—
PDF & scales	2	10	—	2	10	—
e/ $\gamma$ energy scale & resolution	2	2	—	2.5	2.5	—
$\mu$ momentum scale & resolution	—	—	—	2	2	—
Jet bkg estimate	—	—	54–90	—	—	54–90
Sample size	—	8–44	5–47	—	10–25	6–58

The integrated luminosity has been measured with a precision of 2.5% [86]. The effect of pileup modeling on the selection efficiency is measured to be less than a percent over all mass points, and a 1% uncertainty is assigned for it. Systematic uncertainties in the signal selection efficiency include uncertainties arising from the trigger selection, lepton identification [64] and photon identification [88, 89]. Various sources of potential biases in the selection efficiency

measurements are considered to determine such uncertainties.

Systematic uncertainties in the signal acceptance and background cross sections due to the PDF choice have been estimated by following the PDF4LHC prescription [90]. Renormalization and factorization scale uncertainties are evaluated by varying the scales up and down by a factor of 2, both simultaneously and independently. The maximum change observed among the corresponding variations in the signal and the background yields is taken as an estimate of the associated systematic uncertainty. Uncertainties of 2 and 10% are assigned for the PDF and scale uncertainties in the signal acceptance and the background yields, respectively.

Uncertainties in the  $e/\gamma$  energy scale and resolution, and muon momentum scale and resolution translate into uncertainties in the signal acceptance. The effect on the signal acceptance is evaluated by shifting and smearing the  $p_T$  of each object by  $\pm 1$  standard deviation. Although the fraction of energy affected by the  $e/\gamma$  energy scale and resolution uncertainties is larger for  $ee\gamma$  events than for  $\mu\mu\gamma$  events, because the mass window is narrower and the mass resolution is worse, the impact on the acceptance is measured to be stronger in the latter case.

For the jet background estimate, the following uncertainties are taken into account: statistical uncertainties in the jet-to-photon misidentification rate measurement (8–72%), systematic uncertainties in the template distributions used for the misidentification rate measurement (20%), and systematic uncertainties based on the discrepancies observed in the closure tests for the jet background determination procedure performed on simulated samples (50%). The total systematic uncertainty in the jet background prediction is evaluated by summing these uncertainties in quadrature and amounts to 54%, increasing to 90% for masses above 1 TeV.

# Chapter 9

## Results

All the analysis procedures are carried out as described in the previous chapters. Events of interest are selected from the data and simulated samples described in Chapter 4, according to the criteria discussed in Chapter 5. Among the selected events, the SM background contribution is examined in Chapter 6. The background prediction is then compared to the data, extracting the signal as modeled in Chapter 7. Exclusion limits are calculated in order to quantify the agreement of expectation and observation, incorporating systematic uncertainties listed in Chapter 8. As with all modern data analyses, the results of the analyses presented in this thesis heavily rely on statistical tools and interpretation. Therefore, statistical background and methods used for the results are explained first in Section 9.1. The results of the resonant signal search and of the nonresonant signal search are finally presented in Sections 9.2 and 9.3, respectively.

## 9.1 Statistical Interpretation

### 9.1.1 Likelihood and Nuisance Parameters

The likelihood of a simple counting experiment that observes  $n$  events with the expectation of  $b$  events follows the Poisson distribution:

$$\mathcal{L}(n|b) = \prod_{i=1}^N \frac{e^{-b} b^n}{n!}. \quad (9.1)$$

If events are counted in  $N$  independent bins of some observable  $x$ , the full likelihood is given by the product of the likelihoods of the individual bins

$$\mathcal{L}(\vec{n}|\vec{b}) = \prod_{i=1}^N \frac{e^{-b_i} b_i^{n_i}}{n_i!}, \quad (9.2)$$

where  $n_i$  and  $b_i$  are the numbers of observed events and of expected events in the  $i$ -th bin. If the distribution of events is described by a probability distribution function (pdf)  $f_b(x)$  instead of a histogram, the likelihood of total  $n$  observed events and  $b$  expected events is given by

$$\mathcal{L}(\vec{x}|b, f_b(x)) = n^{-1} \prod_{i=1}^N b f_b(x_i) e^{-b}. \quad (9.3)$$

Hereinafter only the binned case will be discussed for simplicity.

A systematic uncertainty is implemented as a nuisance parameter, which is not of interest in the analysis but has to be determined for the statistical interpretation. Given  $L$  nuisance parameters  $\theta_j$  and their inferred default values  $\tilde{\theta}_j$  with the Bayesian probability  $p(\tilde{\theta}|\theta)$ , the likelihood is given by

$$\mathcal{L}(\vec{n}|\vec{b}) = \prod_{i=1}^N \frac{e^{-b_i} b_i^{n_i}}{n_i!} \prod_{j=1}^L p(\tilde{\theta}_j|\theta_j). \quad (9.4)$$

According to Bayes' theorem,  $p(\tilde{\theta}|\theta)$  can be replaced by the frequentist probability  $\rho(\tilde{\theta}|\theta)$ . In general, most systematic uncertainties can be described by a

Gaussian distribution:

$$\rho(\tilde{\theta}|\theta) = \frac{1}{\sqrt{2\pi}\sigma} \exp\left(-\frac{(\theta - \tilde{\theta})^2}{2\sigma^2}\right). \quad (9.5)$$

However, it may not be suitable for positively defined observables. Log-normal pdfs are preferred in such cases:

$$\rho(\tilde{\theta}|\theta) = \frac{1}{\sqrt{2\pi \ln(\kappa)}} \exp\left(-\frac{(\ln(\theta/\tilde{\theta}))^2}{2(\ln(\kappa))^2}\right) \frac{1}{\theta}. \quad (9.6)$$

For a small relative uncertainty  $\epsilon$ , a log-normal pdf with  $\kappa = 1 + \epsilon$  is a good approximation of a Gaussian pdf with  $\epsilon$ . However, they diverge for large uncertainties, as illustrated in Fig. 9.1 (left). Gamma distributions, illustrated in Fig. 9.1 (right), are used for describing statistical fluctuations in limited numbers of events. If the event rate  $n$  in the signal region is extrapolated from  $N$  events in the control region or in MC samples with a transfer factor  $\alpha$ , the corresponding gamma distribution is given by

$$\rho(n) = \frac{1}{\alpha} \frac{(n/\alpha)^N}{N!} \exp(-n/\alpha). \quad (9.7)$$

### 9.1.2 Maximum Likelihood Fit

A maximum likelihood fit is a statistical method to estimate parameters by maximizing a likelihood, i.e., finding the parameter values at which the observation is most probable. In particle physics analyses, two scenarios on signal strength  $\mu$  are commonly considered:

- Background-only fit: in the absence of signal,  $\mu = 0$ , the nuisance parameters  $\vec{\theta}$  are scanned to maximize the likelihood  $\mathcal{L}(\vec{n}|\vec{b}, \vec{\theta})$ .
- Signal+background fit: both the nuisance parameters and the signal strength  $\mu$  of the expected signal distribution  $\vec{s}$  are varied to maximize the likelihood  $\mathcal{L}(\vec{n}|\mu\vec{s} + \vec{b}, \vec{\theta})$ .

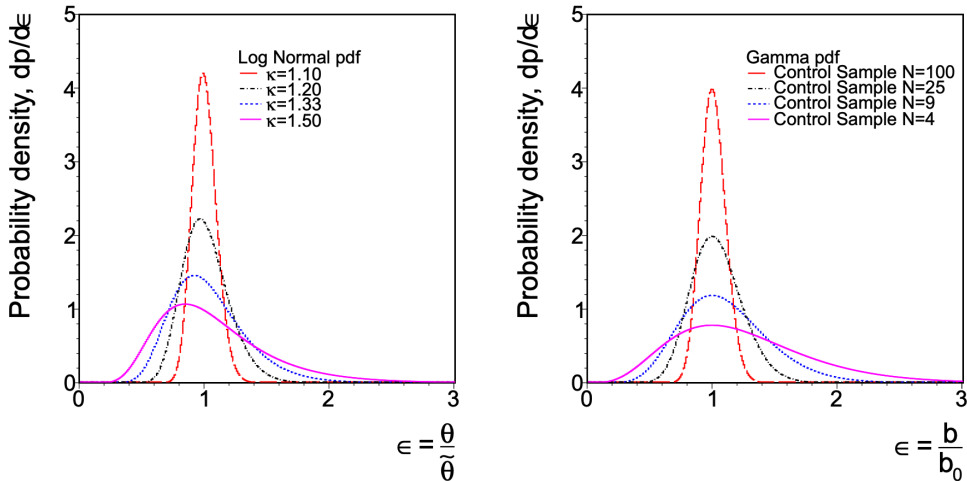


Figure 9.1: The left plot shows log-normal distributions with  $\kappa = 1.10, 1.20, 1.33$  and  $1.50$ . The right plots illustrates gamma distributions with the number of events in a control sample  $B = 100, 25, 9$  and  $4$  [91].

The difference between the pre-fit and post-fit values of a nuisance parameter is called a pull. Significantly large pull values could be signs of inconsistency in the background or signal modeling. In general, maximum likelihood fits can be performed for any number of parameters of interest (freely floating) and nuisance parameters (constrained).

### 9.1.3 Exclusion Limits

In the case where the observed data is consistent with the background prediction, one can still provide a quantitative measure of the signal strength in terms of an upper limits. The  $CL_s$  method [92, 93] is popularly used in CMS for that purpose. This method usually exploits a profile likelihood ratio  $q_\mu$  as a test statistics:

$$q_\mu = -2 \ln \frac{\mathcal{L}(\vec{n} | \mu \vec{s} + \vec{b}, \hat{\theta}_\mu)}{\mathcal{L}(\vec{n} | \hat{\mu} \vec{s} + \vec{b}, \hat{\theta})}, \quad (9.8)$$

with the condition  $0 \leq \hat{\mu} \leq \mu$ . The symbols  $\hat{\mu}$  and  $\hat{\vec{\theta}}$  denote the best fit values of  $\mu$  and  $\vec{\theta}$ , respectively, while  $\hat{\vec{\theta}}_\mu$  is the best fit value of  $\vec{\theta}$  for a fixed value of  $\mu$ . The constraint on  $\hat{\mu}$ ,  $0 \leq \hat{\mu} \leq \mu$ , is required in order to ensure a positive signal rate and one-sided confidence intervals.

The observed value of the test statistics  $q_\mu^{obs}$  can be calculated from Eq. 9.8. The nuisance parameters  $\theta_0^{obs}$  and  $\theta_\mu^{obs}$  in the background-only ( $\mu = 0$ ) and signal+background ( $\mu > 0$ ) hypotheses, respectively, can easily be determined via maximum likelihood fits to the observed data. However, it is difficult to analytically obtain the pdf of the test statistics  $f(q_\mu | \vec{b}, \hat{\vec{\theta}}_0^{obs})$  and  $f(q_\mu | \mu \vec{s} + \vec{b}, \hat{\vec{\theta}}_\mu^{obs})$ . They are usually estimated using MC simulations instead. The probability to have the observed or less compatible results is given by

$$p_{\mu s+b} = P(q_\mu \geq q_\mu^{obs} | \text{signal+background}) = \int_{q_\mu^{obs}}^{\text{inf}} f(q_\mu | \mu \vec{s} + \vec{b}, \hat{\vec{\theta}}_\mu^{obs}) dq_\mu, \quad (9.9)$$

for the signal+background hypothesis, and

$$1 - p_b = P(q_\mu \geq q_\mu^{obs} | \text{background-only}) = \int_{q_\mu^{obs}}^{\text{inf}} f(q_\mu | \vec{b}, \hat{\vec{\theta}}_0^{obs}) dq_\mu, \quad (9.10)$$

for the background-only hypothesis. The  $\text{CL}_s$  is defined as the ratio of both probabilities

$$\text{CL}_s(\mu) = \frac{p_{\mu s+b}}{1 - p_b}. \quad (9.11)$$

Example test statistic distributions for the background-only and signal+background hypotheses are illustrated in Fig. 9.2. The 95% confidence level upper limit on  $\mu$  is determined as the value of  $\mu$  that yields  $\text{CL}_s(\mu) = 0.05$ .

The use of  $\text{CL}_s$  instead of the conventional probability  $p_{\mu s+b}$  can remedy the extreme cases where both the expected numbers of signal and background events are so small that both the background-only and signal+background hypotheses are compatible with the observed data, or where a large deficit is present in data, resulting in a negative signal strength. Also, by definition,  $\text{CL}_s$

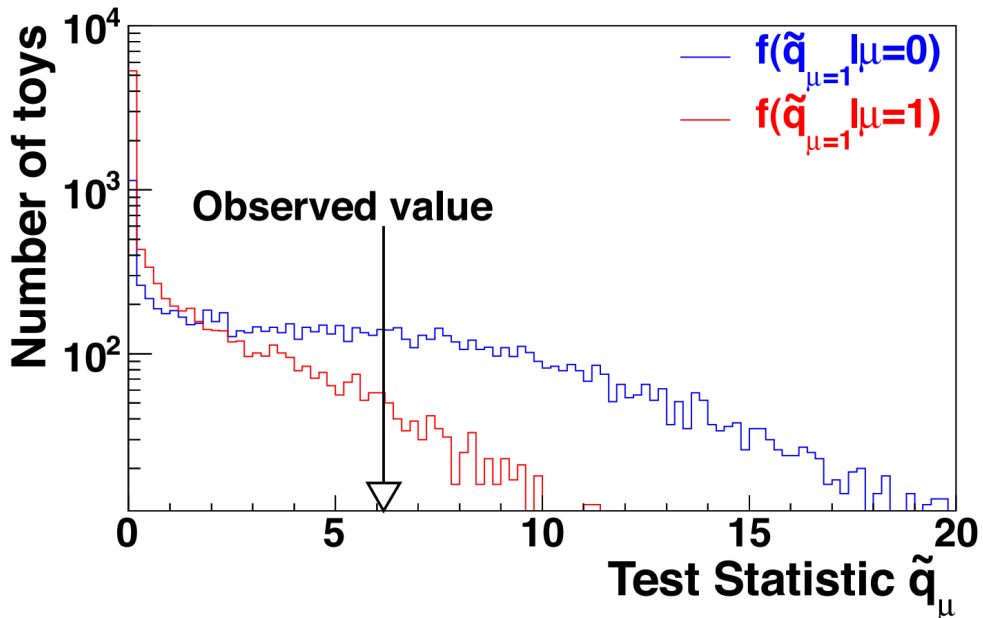


Figure 9.2: Test statistic distributions for ensembles of pseudo-data generated for signal+background and background-only hypotheses. [91].

provides conservative limits with respect to classical frequentist limits based on  $p_{\mu s+b}$ .

The expected limits can be obtained from MC simulations. A cumulative distribution function is built with pseudo-datasets, from which the median (50% quantile),  $\pm 1\sigma$  (16% and 84% quantiles) bands, and  $\pm 2\sigma$  (2.5% and 97.5% quantiles) bands can be extracted, as illustrated in Fig. 9.3.

Generating thousands of pseudo-datasets often costs a huge amount of time and computing resources. We can exploit asymptotic limits as an approximation of  $CL_s$  limits if the expected number of events is large enough [94]. Using the asymptotic formulae, a large set of simulated pseudo-datasets can be replaced by a single representative dataset called an Asimov dataset. The

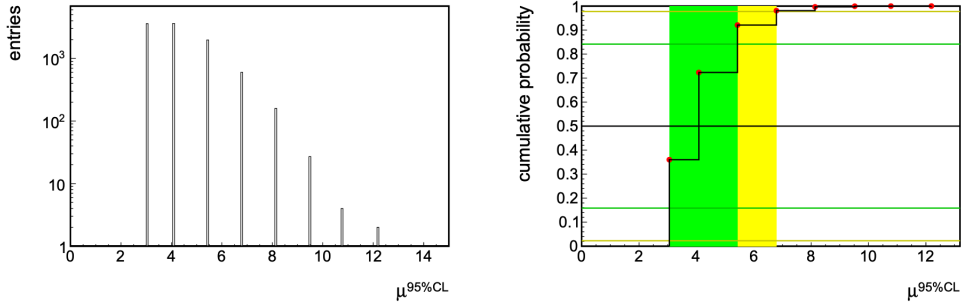


Figure 9.3: (Left) An example of differential distribution of possible limits on  $\mu$  for the background-only hypothesis ( $s = 1$ ,  $b = 1$ , no systematic errors). (Right) Cumulative probability distribution of the plot on the left with 2.5%, 16%, 50%, 84%, and 97.5% quantiles (horizontal lines) defining the median expected limit as well as the  $\pm 1\sigma$  (68%) and  $\pm 2\sigma$  (95%) bands for the expected value of  $\mu$  for the background-only hypothesis [91].

parameters of a non-central  $\chi^2$  distribution, which precisely imitates the test statistic distribution using MC simulations, can be extracted from the Asimov dataset, as illustrated in Fig. 9.4. The median expected limit and the uncertainty bands can also be evaluated using the asymptotic formulae.

#### 9.1.4 Significance

If a considerable excess over the background prediction is observed in data, we can try to exclude the background-only hypothesis thereby claiming the discovery of the signal. It requires to evaluate the probability of background fluctuation that generates an excess equal to or larger than the observed one. This p-value can be obtained using the profile likelihood ratio

$$q_\mu = -2 \ln \frac{\mathcal{L}(\vec{n} | \mu \vec{s} + \vec{b}, \hat{\theta}_\mu)}{\mathcal{L}(\vec{n} | \hat{\mu} \vec{s} + \vec{b}, \hat{\theta})}, \quad (9.12)$$

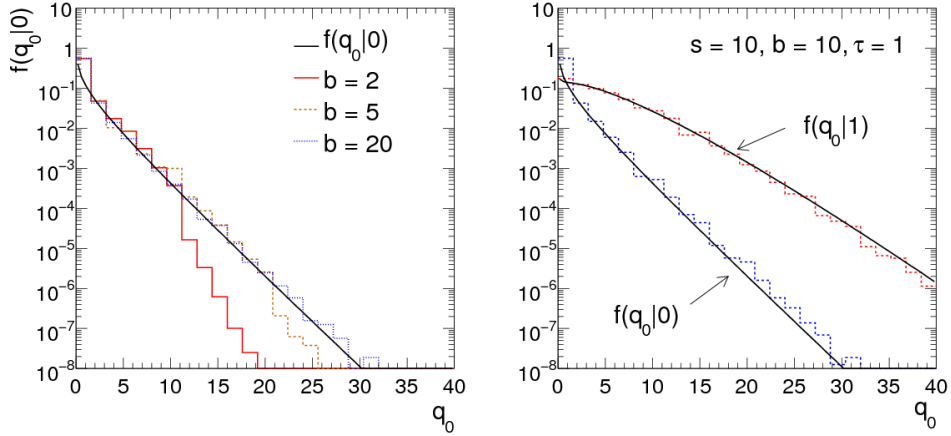


Figure 9.4: (Left) The pdf of  $q_0$  at  $\mu = 0$  for the counting experiment. The solid curve is from the asymptotic formulae and the histograms are from Monte Carlo using different expected number of events  $b = 2, 5, 20$ . (Right) The distributions at  $\mu = 0$  and 1 from both the asymptotic formulae and Monte Carlo simulation based on  $s = 10, b = 10$ , and a scale factor for the number of background events  $\tau = 1$  [94].

with  $\hat{\mu} \geq 0$  so that only excesses of events are interpreted. The distribution  $f(q_0|\vec{b}, \hat{\theta}_0^{obs})$  can be obtained using MC simulations, and the p-value corresponding to the observed value  $q_{obs}$  is given by

$$p_0 = P(q_0 \geq q_0^{obs}) = \int_{q_0^{obs}}^{\infty} f(q_0|\vec{b}, \hat{\theta}_0^{obs}) dq_0. \quad (9.13)$$

The p-value  $p_0$  is often converted into a number of standard deviations corresponding to a Gaussian distribution, so called the significance  $Z_0$ :

$$p_0 = \int_{Z_0}^{\infty} \frac{1}{\sqrt{2\pi}} \exp\left(-\frac{x^2}{2}\right) dx = \frac{1}{2} \left[ 1 - \text{erf}\left(\frac{Z_0}{\sqrt{2}}\right) \right]. \quad (9.14)$$

By convention, one claims the observation of the signal if the significance is at least  $3\sigma$  and the discovery of the signal if the significance is at least  $5\sigma$ .

The mass of a signal is often unknown in new physics searches. It leads to a broad search range with respect to the detector resolution. Searching for a narrow peak over a broad mass range is practically equivalent to the repetition of independent measurement of the signal multiple times. Thus, the actual chance of background fluctuation in such cases is larger than  $p_0$  that is evaluated for a single observation. This phenomenon is called the look-elsewhere effect [95]. The local significance based on  $p_0$  must be corrected into a global significance with consideration for the look-elsewhere effect. Using pseudo-datasets, the global p-value can be obtained by

$$p_0^{global} = N_{Z_0}/N, \quad (9.15)$$

where  $N$  is the number of total pseudo-datasets, and  $N_{Z_0}$  is the number of pseudo-datasets with the observed significance larger than  $Z_0$ .

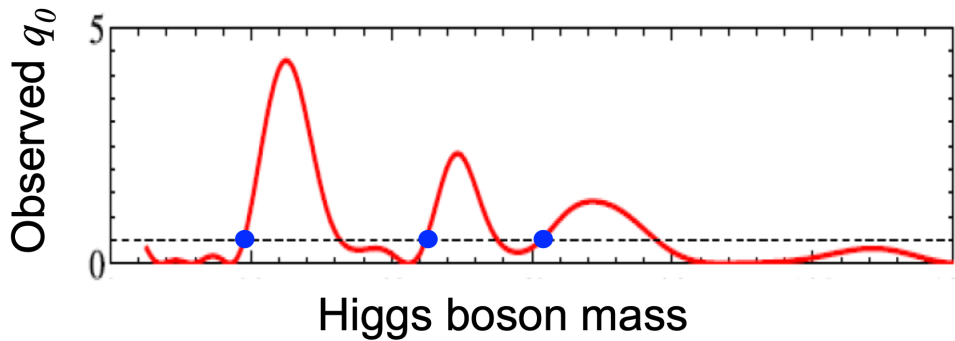


Figure 9.5: An illustration of a hypothetical scan of the test statistic  $q_0$  vs  $m_H$  for some data. Up-crossings for a given threshold value  $u$  are shown with blue points [91].

## 9.2 Results of the Resonant Signal Search

The observation is consistent with the SM prediction in both channels. Upper limits are set on the production cross section of heavy spin-0 resonances using the modified frequentist  $CL_s$  method [92, 93] with the asymptotic approximation [94], in the mass range between 0.35 (0.30) and 4.0 TeV in the  $ee\gamma$  ( $\mu\mu\gamma$ ) channel. More details about the statistical methods are described in Section 9.1. It is known that the asymptotic approximation may result in lower cross section limits than the exact computation in the region where the expected number of events is small. The difference is measured to be at most 4% in the mass range below 1 TeV and 30% for masses around 3 TeV.

The 95% CL upper limits on the product of signal cross section and branching fraction to the  $\ell\ell\gamma$  final state,  $\sigma(X \rightarrow Z\gamma)\mathcal{B}(Z \rightarrow \ell\ell\gamma)$ , are shown in Fig. 9.6. The observed and the median expected limits are shown with the solid and the dashed black lines, respectively. The 68 and 95% CL ranges are denoted by the green and yellow bands, respectively. The largest deviation between the observation and the expectation is observed at the mass of approximately 350 GeV in the  $\mu\mu\gamma$  channel, corresponding to a local (global) significance of approximately 3.0 (2.1) standard deviations for a narrow resonance. Figure 9.7 shows the limits on  $\sigma(X \rightarrow Z\gamma)$  obtained by the combination of both channels with consideration for the leptonic branching fraction of the Z boson decays [96]. The increase with a mass above approximately 3 TeV in the broad resonance interpretation is caused by a significantly large low-mass tail distribution extending outside the truncation window, as discussed in Section 7.1.

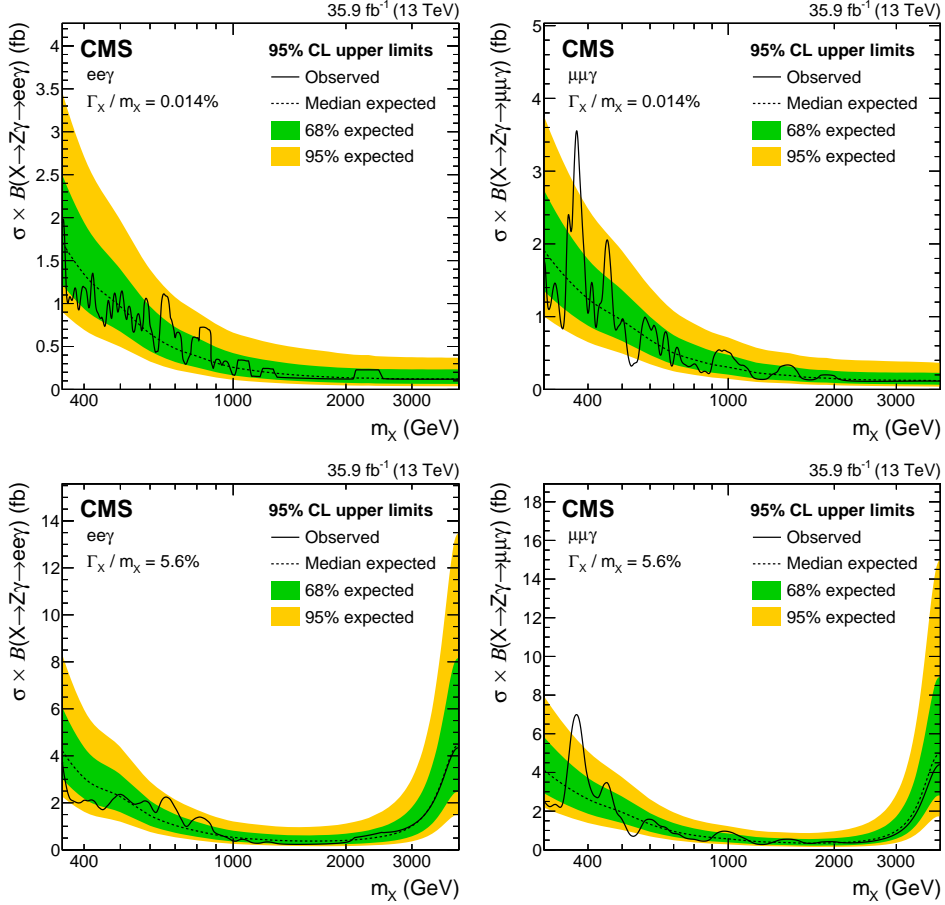


Figure 9.6: Observed (solid) and expected (dashed) 95% CL upper limits on  $\sigma(X \rightarrow Z\gamma) \mathcal{B}(Z \rightarrow \ell\ell\gamma)$ , as a function of signal mass  $m_X$  for the  $ee\gamma$  (left column) and  $\mu\mu\gamma$  (right column) channels, and for narrow (upper row) and broad (lower row) spin-0 resonances. The green and yellow shaded bands correspond to respective 68 and 95% CL ranges in the expected limits for the background-only hypothesis.

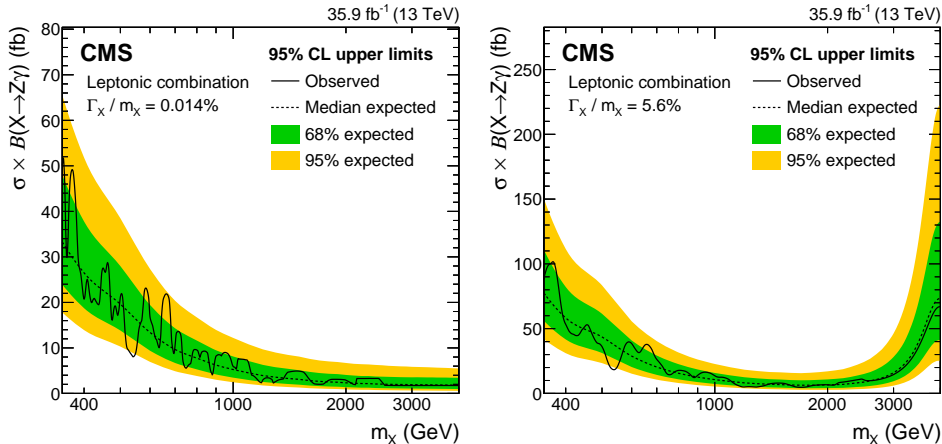


Figure 9.7: Observed (solid) and expected (dashed) 95% CL upper limits on  $\sigma(X \rightarrow Z\gamma)$  as a function of signal mass  $m_X$ , together with the 68% (green) and 95% (yellow) CL ranges of the expected limit for the background-only hypothesis, for the combination of the  $ee\gamma$  and  $\mu\mu\gamma$  channels for (left) narrow and (right) broad spin-0 resonances.

### 9.3 Results of the Nonresonant Signal Search

The data are consistent with the background-only expectations within the uncertainties, as summarized in Tables 9.1 and 9.2. Upper limits are set on the production cross sections of excited electrons and excited muons, as a function of the excited lepton mass in the range between 0.25 and 5.0 TeV, using a single-bin counting method [91]. The limits on the production cross sections are also converted to the corresponding lower limits on the compositeness scale  $\Lambda$ . The modified frequentist  $CL_s$  method [92, 93] with a likelihood ratio as a test statistic is used for setting limits, as described in Section 9.1.

The 95% CL upper limits on the product of the signal cross section and branching fraction to  $ll\gamma$  final states,  $\sigma \mathcal{B}(\ell^* \rightarrow \ell\gamma)$ , are shown in Fig. 9.8. The observed limits are represented by the solid black lines, while the median

Table 9.1: The observed yield and the SM prediction in the search window of the given  $m_{\ell^*}$  in the  $ee\gamma$  channel. The symbols  $N_{\text{data}}$ ,  $N_{\text{prompt}}$ , and  $N_{\text{jet}}$  represent the number of events in data, the prompt photon background prediction, and the jet background estimate, respectively, together with statistical and systematical uncertainties.

$m_{e^*}$ (GeV)	Window (GeV)	$N_{\text{data}}$	$N_{\text{prompt}}$	$N_{\text{jet}}$	$A \epsilon_{\text{sig}}$
250	230–270	84	$74.4 \pm 6.8 \pm 8.0$	$12.5 \pm 0.7 \pm 6.9$	0.30
275	253–297	80	$50.9 \pm 6.0 \pm 5.4$	$10.0 \pm 0.6 \pm 5.5$	0.32
300	276–324	68	$44.7 \pm 5.5 \pm 4.8$	$7.6 \pm 0.5 \pm 4.2$	0.33
330	304–356	51	$40.4 \pm 4.7 \pm 4.3$	$5.9 \pm 0.5 \pm 3.3$	0.35
360	331–389	39	$28.1 \pm 3.8 \pm 3.0$	$4.0 \pm 0.4 \pm 2.2$	0.36
400	368–432	27	$19.4 \pm 3.0 \pm 2.1$	$3.3 \pm 0.3 \pm 1.8$	0.38
450	414–486	17	$15.8 \pm 2.5 \pm 1.7$	$2.8 \pm 0.4 \pm 1.6$	0.40
500	460–540	16	$12.3 \pm 1.9 \pm 1.3$	$2.3 \pm 0.3 \pm 1.3$	0.42
550	506–594	15	$8.2 \pm 1.7 \pm 0.9$	$1.6 \pm 0.2 \pm 0.9$	0.43
600	552–648	10	$7.6 \pm 1.8 \pm 0.8$	$1.2 \pm 0.2 \pm 0.7$	0.44
650	598–702	6	$4.9 \pm 1.3 \pm 0.5$	$0.8 \pm 0.2 \pm 0.5$	0.45
700	644–756	9	$3.6 \pm 1.4 \pm 0.4$	$0.5 \pm 0.1 \pm 0.3$	0.45
750	690–810	5	$3.4 \pm 1.3 \pm 0.4$	$0.3 \pm 0.1 \pm 0.2$	0.46
800	736–864	1	$2.9 \pm 1.1 \pm 0.3$	$0.3 \pm 0.1 \pm 0.2$	0.46
900	828–972	1	$1.5 \pm 0.6 \pm 0.2$	$0.1 \pm 0.1 \pm 0.1$	0.47
1000	920–1080	1	$0.8 \pm 0.8 \pm 0.1$	$0.1 \pm 0.1 \pm 0.1$	0.47
> 1000	$\geq 1058$	1	$1.4 \pm 0.5 \pm 0.2$	$0.1 \pm 0.1 \pm 0.1$	0.49

Table 9.2: The observed yield and the SM prediction in the search window of the given  $m_{\ell^*}$  in the  $\mu\mu\gamma$  channel. The symbols  $N_{\text{data}}$ ,  $N_{\text{prompt}}$ , and  $N_{\text{jet}}$  represent the number of events in data, the prompt photon background prediction, and the jet background estimate, respectively, together with statistical and systematical uncertainties.

$m_{\mu^*}$ (GeV)	Window (GeV)	$N_{\text{data}}$	$N_{\text{prompt}}$	$N_{\text{jet}}$	$A \epsilon_{\text{sig}}$
250	238–262	41	$43.8 \pm 4.9 \pm 4.9$	$8.7 \pm 0.6 \pm 4.8$	0.33
275	261–289	38	$42.8 \pm 5.0 \pm 4.8$	$6.8 \pm 0.5 \pm 3.8$	0.35
300	284–316	47	$35.4 \pm 4.6 \pm 4.0$	$6.5 \pm 0.6 \pm 3.6$	0.37
330	312–348	23	$33.1 \pm 3.9 \pm 3.7$	$5.1 \pm 0.5 \pm 2.8$	0.39
360	340–380	24	$25.8 \pm 3.0 \pm 2.9$	$3.7 \pm 0.4 \pm 2.0$	0.41
400	376–424	26	$22.8 \pm 3.0 \pm 2.6$	$2.2 \pm 0.3 \pm 1.2$	0.44
450	422–478	17	$15.1 \pm 2.3 \pm 1.7$	$1.8 \pm 0.3 \pm 1.0$	0.46
500	467–533	14	$9.8 \pm 1.6 \pm 1.1$	$1.8 \pm 0.3 \pm 1.0$	0.48
550	512–588	11	$10.8 \pm 1.8 \pm 1.2$	$1.0 \pm 0.2 \pm 0.5$	0.49
600	556–644	8	$5.8 \pm 1.2 \pm 0.7$	$0.7 \pm 0.2 \pm 0.4$	0.51
650	600–700	10	$6.8 \pm 1.1 \pm 0.8$	$0.6 \pm 0.1 \pm 0.3$	0.52
700	644–756	5	$5.8 \pm 1.0 \pm 0.7$	$0.4 \pm 0.1 \pm 0.2$	0.52
750	690–810	6	$5.1 \pm 1.0 \pm 0.6$	$0.3 \pm 0.1 \pm 0.2$	0.53
800	736–864	3	$4.5 \pm 1.0 \pm 0.5$	$0.2 \pm 0.1 \pm 0.1$	0.53
900	828–972	2	$3.1 \pm 0.8 \pm 0.4$	$0.1 \pm 0.1 \pm 0.1$	0.54
1000	920–1080	0	$1.1 \pm 0.3 \pm 0.1$	$0.1 \pm 0.0 \pm 0.1$	0.54
> 1000	$\geq 1058$	3	$1.5 \pm 0.3 \pm 0.2$	$0.0 \pm 0.0 \pm 0.0$	0.59

expected limits are denoted by the dashed black lines. The green and yellow bands denote the 68 and 95% CL ranges, respectively. The observed limits on the signal cross section are given as a function of  $m_{\ell^*}$ , ranging from 3.7 to 0.2 fb, and show consistency with the median expected limits. The fluctuations that appear in the median expected limits and the uncertainty bands for  $m_{\ell^*} < 1$  TeV originate from the statistical fluctuations in the number of selected simulated events. The theoretical cross sections with the NLO QCD corrections are denoted by the dashed lines.

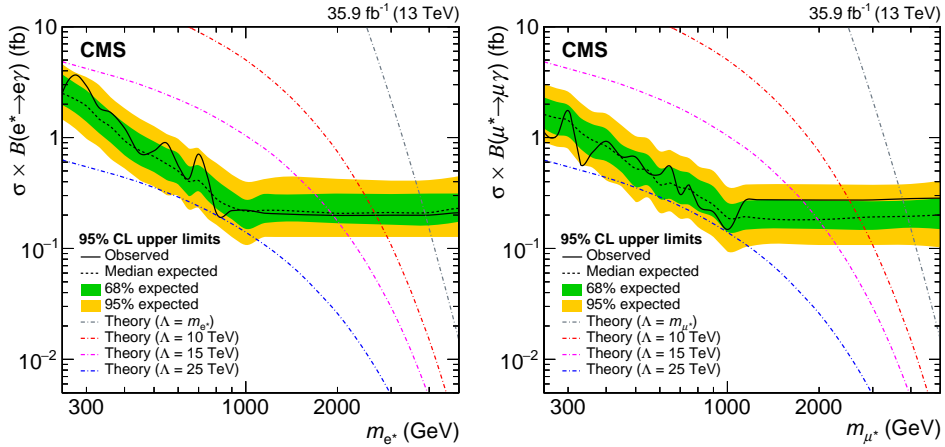


Figure 9.8: Observed (solid) and expected (dashed) 95% CL upper limits on the product of the production cross section and branching fraction as a function of signal mass  $m_{\ell^*}$ , together with the 68% (green, inner) and 95% (yellow, outer) quantiles of the expected limit, for  $e^*$  (left) and  $\mu^*$  (right).

Exclusions on the parameters of interest in this analysis,  $m_{\ell^*}$  and  $\Lambda$ , are set by comparison between the upper limits on  $\sigma \mathcal{B}(\ell^* \rightarrow \ell \gamma)$  and the theoretical cross sections. The exclusion on  $m_{\ell^*}$  is given as a function of  $\Lambda$  because both the excited lepton mass and the compositeness scale are free parameters in the reference model. The limit under the assumption of  $\Lambda = m_{\ell^*}$  is selected

as a representative exclusion limit. For excited electrons (muons), the region of  $m_{\ell^*} < 3.9$  (3.8) TeV is excluded by the observation in the case of  $\Lambda = m_{\ell^*}$ . The  $\Lambda$  value at which the theoretical cross section equals the limit on the cross section is interpreted as the lower limit on  $\Lambda$  for each  $m_{\ell^*}$  hypothesis. The exclusion on  $\Lambda$  varies from 15 to 25 TeV for  $m_{\ell^*}$  between 0.25 and 1.0 TeV, and decreases as  $m_{\ell^*}$  increases up to  $\approx 4$  TeV in the range  $m_{\ell^*} > 1.0$  TeV, as shown in Figure 9.9. The most stringent observed limit on  $\Lambda$  is set for  $m_{\ell^*}$  between 0.5 and 1.0 TeV, which excludes  $\Lambda < 25$  TeV for both  $e^*$  and  $\mu^*$ . The representative values of exclusion limits are summarized in Table 9.3.

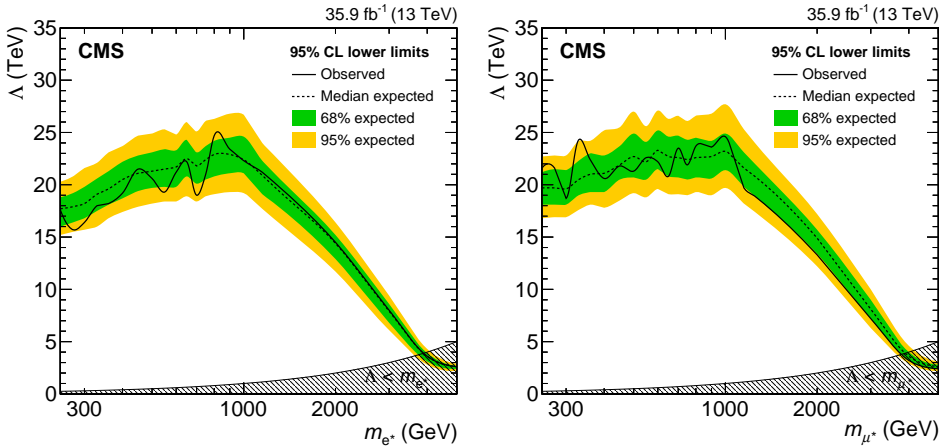


Figure 9.9: Observed (solid) and expected (dashed) 95% CL lower limits on the compositeness scale as a function of signal mass  $m_{\ell^*}$ , together with the 68% (green, inner) and 95% (yellow, outer) quantiles of the expected limit, for  $e^*$  (left) and  $\mu^*$  (right).

Table 9.3: Summary of the observed (expected) lower limits on  $m_{\ell^*}$ , assuming  $\Lambda = m_{\ell^*}$ , and the best observed (expected) lower limits on  $\Lambda$  in the mass range 0.5–1.0 TeV.

Channel	Observed (expected) limit on $m_{\ell^*}$ for $m_{\ell^*} = \Lambda$ , TeV	Observed (expected) limit on $\Lambda$ for $m_{\ell^*} \approx 1$ TeV, TeV
$ee\gamma$	3.9 (3.8)	25 (23)
$\mu\mu\gamma$	3.8 (3.9)	25 (23)

# Chapter 10

## Conclusions

The SM is a successful and predictive theory of high-energy physics. Nevertheless, there are open fundamental questions making physicists strongly believe that the SM is not a complete theory of the universe. Among various attempts to answer such questions, some predict new physics leaves its unique signatures in  $ll\gamma$  final states. Physics analyses in  $ll\gamma$  final states can exploit many experimental advantages including the precise reconstruction of final-state particles as well as only a small contamination of nonresonant SM processes. Two representative searches for new physics in  $ll\gamma$  final states are in particular presented in this thesis; a search for  $Z\gamma$  resonances and a search for excited leptons in  $ll\gamma$  final states.

The analyses have been performed on data from pp collisions at the LHC, recorded by the CMS detector. During the Run 2 operation, the LHC machine successfully delivered more than  $160\text{ fb}^{-1}$  of pp collisions at a center-of-mass energy of 13 TeV, which exceeds the previous Run 1 operation in terms of both the amount of data and the collision energy. Those pp collisions, which

are the hardest ever, have been precisely measured and reconstructed by the CMS experiment, providing the best opportunity for new physics searches. The analyses use in particular the data collected in 2016, corresponding to an integrated luminosity of  $35.9 \text{ fb}^{-1}$ .

The two searches largely share their strategies for signal selection in the same final state. However, an important difference between them lies in the signal event topology. Events with a  $Z\gamma$  resonance have two leptons from the leptonic decay of the Z boson and one energetic photon directly from the signal resonance. The resonance mass can be precisely reconstructed as the invariant mass of  $Z\gamma$ , resulting in a clear resonance peak in the  $m_{Z\gamma}$  spectrum. Thus, we have developed a strategy to extract the information of signal and background distributions directly from the data  $m_{Z\gamma}$  spectrum through the unbinned maximum-likelihood fits of the signal and background PDFs. On the other hand, excited lepton events have two leptons not decayed from the same resonance; one lepton is directly produced from CI and the other one is a decay product of the excited lepton. This makes us difficult to identify the reconstructed mass of the excited lepton from the masses of two possible  $\ell\gamma$  combinations,  $m_{\ell\gamma}^{\min}$  and  $m_{\ell\gamma}^{\max}$ . But it also means that either of those two masses must be equal to the reconstructed excited lepton mass. From this fact, we have implemented an L-shaped search window centered at the excited lepton mass on the two-dimensional distribution of  $m_{\ell\gamma}^{\min}$  and  $m_{\ell\gamma}^{\max}$  to count the yields of excited electron and muon signals. Among data events in the search window, prompt photon backgrounds are estimated using simulation while misidentified photon backgrounds are extracted from data.

No evidence for new physics has been observed in any of the searches presented in this thesis. The results of the  $Z\gamma$  resonance search are interpreted in terms of upper limits on the product of the production cross section and

the branching fraction to  $Z\gamma$ . In the excited lepton search, limits are set on the product of the production cross section and the branching fraction to  $\ell\ell\gamma$ , as well as on the parameter space of  $m_{\ell^*}$  and  $\Lambda$ . Excited electrons and muons are excluded for masses below 3.9 and 3.8 TeV, respectively, in the case  $\Lambda = m_{\ell^*}$ . The best observed limit on the compositeness scale is obtained with an excited lepton mass of around 1.0 TeV, excluding values below 25 TeV for both excited electrons and muons.

Despite no new physics observation in this thesis, there is no need to be disappointed as the LHC has just opened up a new horizon of the TeV scale physics. The remaining Run 2 data, the data that will be collected in the future Run 3 operation, and the subsequent operations of the HL-LHC will provide the best chance to answer many open questions on the SM. We do not know what these data will reveal us, and whether the SM will continue to resist to experimental tests or if clear signs of new physics will appear. From the near future of the LHC Run 3 operation to the end of HL-LHC operations, searches for  $Z\gamma$  resonances and excited leptons will continue to be one of the main paths to the exploration of new physics at the TeV scale.

# Bibliography

- [1] Estia Eichten and Kenneth Lane. “Low-scale technicolor at the Tevatron and LHC”. In: *Phys. Lett. B* 669 (2008), p. 235. DOI: 10.1016/j.physletb.2008.09.047. arXiv: 0706.2339 [hep-ph].
- [2] Ayres Freitas and Pedro Schwaller. “Multi-photon signals from composite models at LHC”. In: *JHEP* 01 (2011), p. 022. DOI: 10.1007/JHEP01(2011)022. arXiv: 1010.2528 [hep-ph].
- [3] Riccardo Barbieri and Riccardo Torre. “Signals of single particle production at the earliest LHC”. In: *Phys. Lett. B* 695 (2011), p. 259. DOI: 10.1016/j.physletb.2010.11.037. arXiv: 1008.5302 [hep-ph].
- [4] Ian Low, Joseph Lykken, and Gabe Shaughnessy. “Singlet scalars as Higgs imposters at the Large Hadron Collider”. In: *Phys. Rev. D* 84 (2011), p. 035027. DOI: 10.1103/PhysRevD.84.035027. arXiv: 1105.4587 [hep-ph].
- [5] H. Davoudiasl, J. L. Hewett, and T. G. Rizzo. “Experimental probes of localized gravity: On and off the wall”. In: *Phys. Rev. D* 63 (2001), p. 075004. DOI: 10.1103/PhysRevD.63.075004. arXiv: hep-ph/0006041 [hep-ph].

- [6] Benjamin C. Allanach, Jordan P. Skittrall, and K. Sridhar. “Z boson decay to photon plus Kaluza-Klein graviton in large extra dimensions”. In: *JHEP* 11 (2007), p. 089. DOI: 10.1088/1126-6708/2007/11/089. arXiv: 0705.1953 [hep-ph].
- [7] Georges Aad et al. “Observation of a new particle in the search for the Standard Model Higgs boson with the ATLAS detector at the LHC”. In: *Phys. Lett. B* 716 (2012), p. 1. DOI: 10.1016/j.physletb.2012.08.020. arXiv: 1207.7214 [hep-ex].
- [8] Serguei Chatrchyan et al. “Observation of a new boson at a mass of 125 GeV with the CMS experiment at the LHC”. In: *Phys. Lett. B* 716 (2012), p. 30. DOI: 10.1016/j.physletb.2012.08.021. arXiv: 1207.7235 [hep-ex].
- [9] Serguei Chatrchyan et al. “Observation of a new boson with mass near 125 GeV in pp collisions at  $\sqrt{s} = 7$  and 8 TeV”. In: *JHEP* 06 (2013), p. 081. DOI: 10.1007/JHEP06(2013)081. arXiv: 1303.4571 [hep-ex].
- [10] L. D. Landau. “On the angular momentum of a system of two photons”. In: *Dokl. Akad. Nauk Ser. Fiz.* 60 (1948), p. 207. DOI: 10.1016/B978-0-08-010586-4.50070-5.
- [11] Chen-Ning Yang. “Selection rules for the dematerialization of a particle into two photons”. In: *Phys. Rev.* 77 (1950), p. 242. DOI: 10.1103/PhysRev.77.242.
- [12] O. W. Greenberg and C. A. Nelson. “Composite Models of Leptons”. In: *Phys. Rev. D* 10 (1974), p. 2567. DOI: 10.1103/PhysRevD.10.2567.
- [13] Jogesh C. Pati, Abdus Salam, and J. A. Strathdee. “Are quarks composite?” In: *Phys. Lett. B* 59 (1975), p. 265. DOI: 10.1016/0370-2693(75)90042-8.

- [14] O. W. Greenberg and Joseph Sucher. “A quantum structure dynamic model of quarks, leptons, weak vector bosons, and Higgs mesons”. In: *Phys. Lett. B* 99 (1981), p. 339. DOI: 10.1016/0370-2693(81)90113-1.
- [15] H. Terazawa et al. “Observable effects of the possible substructure of leptons and quarks”. In: *Phys. Lett. B* 112 (1982), p. 387. DOI: 10.1016/0370-2693(82)91075-9.
- [16] M. Abolins et al. “Testing the Compositeness of Quarks and Leptons”. In: *Elementary Particles and Future Facilities (Snowmass 1982)*. eConf C8206282. 1982, p. 274. URL: <http://inspirehep.net/record/185862/files/C8206282-pg274.PDF>.
- [17] E. Eichten, Kenneth D. Lane, and Michael E. Peskin. “New Tests for Quark and Lepton Substructure”. In: *Phys. Rev. Lett.* 50 (1983), p. 811. DOI: 10.1103/PhysRevLett.50.811.
- [18] H. Harari. “Composite models for quarks and leptons”. In: *Phys. Rept.* 104 (1984), p. 159. DOI: 10.1016/0370-1573(84)90207-2.
- [19] U. Baur, M. Spira, and P. M. Zerwas. “Excited quark and lepton production at hadron colliders”. In: *Phys. Rev. D* 42 (1990), p. 815. DOI: 10.1103/PhysRevD.42.815.
- [20] Satyaki Bhattacharya et al. “Search for excited quarks in  $q\bar{q} \rightarrow \gamma\gamma$  at the CERN LHC”. In: *Phys. Rev. D* 76 (2007), p. 115017. DOI: 10.1103/PhysRevD.76.115017. arXiv: 0705.3472 [hep-ph].
- [21] Satyaki Bhattacharya et al. “Quark Excitations Through the Prism of Direct Photon Plus Jet at the LHC”. In: *Phys. Rev. D* 80 (2009), p. 015014. DOI: 10.1103/PhysRevD.80.015014. arXiv: 0901.3927 [hep-ph].

- [22] Albert M Sirunyan et al. “Search for  $Z\gamma$  resonances using leptonic and hadronic final states in proton-proton collisions at  $\sqrt{s} = 13$  TeV”. In: *JHEP* 09 (2018), p. 148. DOI: 10.1007/JHEP09(2018)148. arXiv: 1712.03143 [hep-ex].
- [23] Albert M Sirunyan et al. “Search for excited leptons in  $\ell\ell\gamma$  final states in proton-proton collisions at  $\sqrt{s} = 13$  TeV”. In: *JHEP* 04 (2019), p. 015. DOI: 10.1007/JHEP04(2019)015. arXiv: 1811.03052 [hep-ex].
- [24] Morad Aaboud et al. “Search for heavy resonances decaying to a Z boson and a photon in pp collisions at  $\sqrt{s} = 13$  TeV with the ATLAS detector”. In: *Phys. Lett. B* 764 (2017), p. 11. DOI: 10.1016/j.physletb.2016.11.005. arXiv: 1607.06363 [hep-ex].
- [25] Albert M Sirunyan et al. “Search for high-mass  $Z\gamma$  resonances in proton-proton collisions at  $\sqrt{s} = 8$  and 13 TeV using jet substructure techniques”. In: *Phys. Lett. B* 772 (2017), p. 363. DOI: 10.1016/j.physletb.2017.06.062. arXiv: 1612.09516 [hep-ex].
- [26] P. Achard et al. “Search for anomalous couplings in the Higgs sector at LEP”. In: *Phys. Lett. B* 589 (2004), p. 89. DOI: 10.1016/j.physletb.2004.03.048. arXiv: hep-ex/0403037 [hep-ex].
- [27] V. M. Abazov et al. “Search for particles decaying into a Z boson and a photon in  $p\bar{p}$  collisions at  $\sqrt{s} = 1.96$  TeV”. In: *Phys. Lett. B* 641 (2006), p. 415. DOI: 10.1016/j.physletb.2006.08.079. arXiv: hep-ex/0605064 [hep-ex].
- [28] V. M. Abazov et al. “Search for a scalar or vector particle decaying into  $Z\gamma$  in  $p\bar{p}$  collisions at  $\sqrt{s} = 1.96$  TeV”. In: *Phys. Lett. B* 671 (2009), p. 349. DOI: 10.1016/j.physletb.2008.12.009. arXiv: 0806.0611 [hep-ex].

- [29] Georges Aad et al. “Measurements of  $W\gamma$  and  $Z\gamma$  production in pp collisions at  $\sqrt{s} = 7$  TeV with the ATLAS detector at the LHC”. In: *Phys. Rev. D* 87 (2013), p. 112003. DOI: 10.1103/PhysRevD.87.112003. arXiv: 1302.1283 [hep-ex].
- [30] Georges Aad et al. “Search for new resonances in  $W\gamma$  and  $Z\gamma$  final states in pp collisions at  $\sqrt{s} = 8$  TeV with the ATLAS detector”. In: *Phys. Lett. B* 738 (2014), p. 428. DOI: 10.1016/j.physletb.2014.10.002. arXiv: 1407.8150 [hep-ex].
- [31] Morad Aaboud et al. “Searches for the  $Z\gamma$  decay mode of the Higgs boson and for new high-mass resonances in  $pp$  collisions at  $\sqrt{s} = 13$  TeV with the ATLAS detector”. In: *JHEP* 10 (2017), p. 112. DOI: 10.1007/JHEP10(2017)112. arXiv: 1708.00212 [hep-ex].
- [32] Vardan Khachatryan et al. “Search for high-mass  $Z\gamma$  resonances in  $e^+e^-\gamma$  and  $\mu^+\mu^-\gamma$  final states in proton-proton collisions at  $\sqrt{s} = 8$  and 13 TeV”. In: *JHEP* 01 (2017), p. 076. DOI: 10.1007/JHEP01(2017)076. arXiv: 1610.02960 [hep-ex].
- [33] Serguei Chatrchyan et al. “Search for a Higgs boson decaying into a  $Z$  and a photon in pp collisions at  $\sqrt{s} = 7$  and 8 TeV”. In: *Phys. Lett. B* 726 (2013), p. 587. DOI: 10.1016/j.physletb.2013.09.057. arXiv: 1307.5515 [hep-ex].
- [34] Georges Aad et al. “Search for Higgs boson decays to a photon and a  $Z$  boson in pp collisions at  $\sqrt{s} = 7$  and 8 TeV with the ATLAS detector”. In: *Phys. Lett. B* 732 (2014), p. 8. DOI: 10.1016/j.physletb.2014.03.015. arXiv: 1402.3051 [hep-ex].

- [35] S. Chatrchyan et al. “Search for excited leptons in pp collisions at  $\sqrt{s} = 7$  TeV”. In: *Phys. Lett. B* 720 (2013), p. 309. DOI: 10.1016/j.physletb.2013.02.031. arXiv: 1210.2422 [hep-ex].
- [36] Vardan Khachatryan et al. “Search for excited leptons in proton-proton collisions at  $\sqrt{s} = 8$  TeV”. In: *JHEP* 03 (2016), p. 125. DOI: 10.1007.arXiv: 1511.01407 [hep-ex].
- [37] Albert M Sirunyan et al. “Search for an excited lepton that decays via a contact interaction to a lepton and two jets in proton-proton collisions at  $\sqrt{s} = 13$  TeV”. In: *JHEP* 05 (2020), p. 052. DOI: 10.1007/JHEP05(2020)052. arXiv: 2001.04521 [hep-ex].
- [38] D. Buskulic et al. “Search for excited leptons at 130–140 GeV”. In: *Phys. Lett. B* 385 (1996), p. 445. DOI: 10.1016/0370-2693(96)00961-6.
- [39] P. Abreu et al. “Search for composite and exotic fermions at LEP 2”. In: *Eur. Phys. J. C* 8 (1999), p. 41. DOI: 10.1007/s100529901074. arXiv: hep-ex/9811005.
- [40] G. Abbiendi et al. “Search for unstable heavy and excited leptons at LEP 2”. In: *Eur. Phys. J. C* 14 (2000), p. 73. DOI: 10.1007/s100520050734. arXiv: hep-ex/0001056.
- [41] P. Achard et al. “Search for excited leptons at LEP”. In: *Phys. Lett. B* 568 (2003), p. 23. DOI: 10.1016/j.physletb.2003.05.004. arXiv: hep-ex/0306016.
- [42] F. D. Aaron et al. “Search for excited electrons in ep collisions at HERA”. In: *Phys. Lett. B* 666 (2008), p. 131. DOI: 10.1016/j.physletb.2008.07.014. arXiv: 0805.4530.

- [43] D. Acosta et al. “Search for excited and exotic electrons in the  $e\gamma$  decay channel in  $p\bar{p}$  collisions at  $\sqrt{s} = 1.96$  TeV”. In: *Phys. Rev. Lett.* 94 (2005), p. 101802. DOI: 10.1103/PhysRevLett.94.101802. arXiv: hep-ex/0410013.
- [44] A. Abulencia et al. “Search for excited and exotic muons in the  $\mu\gamma$  decay channel in  $p\bar{p}$  collisions at  $\sqrt{s} = 1.96$  TeV”. In: *Phys. Rev. Lett.* 97 (2006), p. 191802. DOI: 10.1103/PhysRevLett.97.191802. arXiv: hep-ex/0606043.
- [45] V. M. Abazov et al. “Search for excited muons in  $p\bar{p}$  collisions at  $\sqrt{s} = 1.96$  TeV”. In: *Phys. Rev. D* 73 (2006), p. 111102. DOI: 10.1103/PhysRevD.73.111102. arXiv: hep-ex/0604040.
- [46] V. M. Abazov et al. “Search for excited electrons in  $p\bar{p}$  collisions at  $\sqrt{s} = 1.96$  TeV”. In: *Phys. Rev. D* 77 (2008), p. 091102. DOI: 10.1103/PhysRevD.77.091102. arXiv: 0801.0877.
- [47] Georges Aad et al. “Search for excited leptons in proton-proton collisions at  $\sqrt{s} = 7$  TeV with the ATLAS detector”. In: *Phys. Rev. D* 85 (2012), p. 072003. DOI: 10.1103/PhysRevD.85.072003. arXiv: 1201.3293 [hep-ex].
- [48] G. Aad et al. “Search for excited electrons and muons in  $\sqrt{s} = 8$  TeV proton-proton collisions with the ATLAS detector”. In: *New J. Phys.* 15 (2013), p. 093011. DOI: 10.1088/1367-2630/15/9/093011. arXiv: 1308.1364 [hep-ph].
- [49] G. Aad et al. “A search for an excited muon decaying to a muon and two jets in pp collisions at  $\sqrt{s} = 8$  TeV with the ATLAS detector”. In: *New J. Phys.* 18 (2016), p. 073021. DOI: 10.1088/1367-2630/18/7/073021. arXiv: 1601.05627 [hep-ph].

- [50] Morad Aaboud et al. “Search for excited electrons singly produced in proton–proton collisions at  $\sqrt{s} = 13$  TeV with the ATLAS experiment at the LHC”. In: *Eur. Phys. J. C* 79.9 (2019), p. 803. DOI: 10.1140/epjc/s10052-019-7295-1. arXiv: 1906.03204 [hep-ex].
- [51] D. Hanneke, S. Fogwell Hoogerheide, and G. Gabrielse. “Cavity control of a single-electron quantum cyclotron: Measuring the electron magnetic moment”. In: *Phys. Rev. A* 83 (5 May 2011), p. 052122. DOI: 10.1103/PhysRevA.83.052122.
- [52] C. S. Wu et al. “Experimental Test of Parity Conservation in Beta Decay”. In: *Phys. Rev.* 105 (4 Feb. 1957), pp. 1413–1415. DOI: 10.1103/PhysRev.105.1413.
- [53] M. Goldhaber, L. Grodzins, and A. W. Sunyar. “Helicity of Neutrinos”. In: *Phys. Rev.* 109 (3 Feb. 1958), pp. 1015–1017. DOI: 10.1103/PhysRev.109.1015.
- [54] R. P. Feynman and M. Gell-Mann. “Theory of the Fermi Interaction”. In: *Phys. Rev.* 109 (1 Jan. 1958), pp. 193–198. DOI: 10.1103/PhysRev.109.193.
- [55] T. Fazzini et al. “Electron Decay of the Pion”. In: *Phys. Rev. Lett.* 1 (7 Oct. 1958), pp. 247–249. DOI: 10.1103/PhysRevLett.1.247.
- [56] Steven Weinberg. “A Model of Leptons”. In: *Phys. Rev. Lett.* 19 (21 Nov. 1967), pp. 1264–1266. DOI: 10.1103/PhysRevLett.19.1264.
- [57] G. 'tHooft. “Renormalization of massless Yang-Mills fields”. In: *Nuclear Physics B* 33.1 (1971), pp. 173–199. ISSN: 0550-3213. DOI: [https://doi.org/10.1016/0550-3213\(71\)90395-6](https://doi.org/10.1016/0550-3213(71)90395-6).

- [58] S. L. Glashow, J. Iliopoulos, and L. Maiani. “Weak Interactions with Lepton-Hadron Symmetry”. In: *Phys. Rev. D* 2 (7 Oct. 1970), pp. 1285–1292. DOI: 10.1103/PhysRevD.2.1285.
- [59] S. Biondini et al. “Perturbative unitarity bounds for effective composite models”. In: *Phys. Lett. B* 795 (2019). [Erratum: Phys.Lett.B 799, 134990 (2019)], pp. 644–649. DOI: 10.1016/j.physletb.2019.06.042. arXiv: 1903.12285 [hep-ph].
- [60] S. Chatrchyan et al. “The CMS Experiment at the CERN LHC”. In: *JINST* 3 (2008), S08004. DOI: 10.1088/1748-0221/3/08/S08004.
- [61] A. Benaglia. “The CMS ECAL performance with examples”. In: *JINST* 9 (2014). Ed. by Pietro Govoni et al., p. C02008. DOI: 10.1088/1748-0221/9/02/C02008.
- [62] P. Adzic et al. “Energy resolution of the barrel of the CMS electromagnetic calorimeter”. In: *JINST* 2 (2007), P04004. DOI: 10.1088/1748-0221/2/04/P04004.
- [63] S Chatrchyan et al. “Performance of CMS Hadron Calorimeter Timing and Synchronization using Test Beam, Cosmic Ray, and LHC Beam Data”. In: *JINST* 5 (2010), T03013. DOI: 10.1088/1748-0221/5/03/T03013. arXiv: 0911.4877 [physics.ins-det].
- [64] A. M. Sirunyan et al. “Performance of the CMS muon detector and muon reconstruction with proton-proton collisions at  $\sqrt{s} = 13$  TeV”. In: *JINST* 13 (2018), P06015. DOI: 10.1088/1748-0221/13/06/P06015. arXiv: 1804.04528 [hep-ex].
- [65] A. M. Sirunyan et al. “Particle-flow reconstruction and global event description with the CMS detector”. In: *JINST* 12 (2017), P10003. DOI: 10.1088/1748-0221/12/10/P10003. arXiv: 1706.04965 [physics.ins-det].

- [66] W Adam et al. “Reconstruction of electrons with the Gaussian-sum filter in the CMS tracker at the LHC”. In: *Journal of Physics G: Nuclear and Particle Physics* 31.9 (2005), N9–N20. DOI: 10.1088/0954-3899/31/9/n01.
- [67] Matteo Cacciari, Gavin P. Salam, and Gregory Soyez. “The anti- $k_T$  jet clustering algorithm”. In: *JHEP* 04 (2008), p. 063. DOI: 10.1088/1126-6708/2008/04/063. arXiv: 0802.1189 [hep-ex].
- [68] A.M. Sirunyan et al. “Performance of reconstruction and identification of  $\tau$  leptons decaying to hadrons and  $\nu_\tau$  in pp collisions at  $\sqrt{s} = 13$  TeV”. In: *JINST* 13.10 (2018), P10005. DOI: 10.1088/1748-0221/13/10/P10005. arXiv: 1809.02816 [hep-ex].
- [69] Richard D. Ball et al. “Parton distributions for the LHC Run II”. In: *JHEP* 04 (2015), p. 040. DOI: 10.1007/JHEP04(2015)040. arXiv: 1410.8849 [hep-ph].
- [70] John M. Campbell, J.W. Huston, and W.J. Stirling. “Hard Interactions of Quarks and Gluons: A Primer for LHC Physics”. In: *Rept. Prog. Phys.* 70 (2007), p. 89. DOI: 10.1088/0034-4885/70/1/R02. arXiv: hep-ph/0611148.
- [71] Torbjörn Sjöstrand et al. “An introduction to PYTHIA 8.2”. In: *Comput. Phys. Commun.* 191 (2015), p. 159. DOI: 10.1016/j.cpc.2015.01.024. arXiv: 1410.3012.
- [72] Vardan Khachatryan et al. “Event generator tunes obtained from underlying event and multiparton scattering measurements”. In: *Eur. Phys. J. C* 76 (2016), p. 155. DOI: 10.1140/epjc/s10052-016-3988-x. arXiv: 1512.00815 [hep-ex].

- [73] S. Agostinelli et al. “GEANT4—A simulation toolkit”. In: *Nucl. Instrum. Meth. A* 506 (2003), p. 250. DOI: 10.1016/S0168-9002(03)01368-8.
- [74] Swapan Majhi. “QCD corrections to excited lepton (pair) production at the LHC”. In: *Phys. Rev. D* 88 (2013), p. 074028. DOI: 10.1103/PhysRevD.88.074028. arXiv: 1210.8307 [hep-ph].
- [75] J. Alwall et al. “The automated computation of tree-level and next-to-leading order differential cross sections, and their matching to parton shower simulations”. In: *JHEP* 07 (2014), p. 079. DOI: 10.1007/JHEP07(2014)079. arXiv: 1405.0301 [hep-ph].
- [76] T Gehrmann et al. “ $W^+W^-$  Production at Hadron Colliders in Next-to-Next-to-Leading-Order QCD”. In: *Phys. Rev. Lett.* 113 (2014), p. 212001. DOI: 10.1103/PhysRevLett.113.212001. arXiv: 1408.5243 [hep-ph].
- [77] J. M. Campbell and R. K. Ellis. “MCFM for the Tevatron and the LHC”. In: *Nucl. Phys. Proc. Suppl.* 205 (2010), p. 10. DOI: 10.1016/j.nuclphysbps.2010.08.011. arXiv: 1007.3492 [hep-ph].
- [78] A. Hoecker et al. *TMVA - Toolkit for Multivariate Data Analysis*. 2007. arXiv: physics/0703039 [physics.data-an].
- [79] Serguei Chatrchyan et al. “Search for resonances in the dilepton mass distribution in pp collisions at  $\sqrt{s} = 7$  TeV”. In: *JHEP* 05 (2011), p. 093. DOI: 10.1007/JHEP05(2011)093. arXiv: 1103.0981 [hep-ex].
- [80] R. A. Fisher. “On the interpretation of  $\chi^2$  from contingency tables, and the calculation of  $p$ ”. In: *J. Roy. Stat. Soc.* 85 (1922), p. 87. DOI: 10.2307/2340521.
- [81] Vardan Khachatryan et al. “Search for Resonant Production of High-Mass Photon Pairs in Proton-Proton Collisions at  $\sqrt{s} = 8$  and 13 TeV”.

- In: *Phys. Rev. Lett.* 117 (2016), p. 051802. DOI: 10.1103/PhysRevLett.117.051802. arXiv: 1606.04093 [hep-ex].
- [82] F. Garwood. “Fiducial Limits for the Poisson Distribution”. In: *Biometrika* 28 (1936), p. 437. DOI: 10.1093/biomet/28.3-4.437.
- [83] A. M. Sirunyan et al. “Search for high-mass resonances in dilepton final states in proton-proton collisions at  $\sqrt{s} = 13$  TeV”. In: *JHEP* 06 (2018), p. 120. DOI: 10.1007/JHEP06(2018)120. arXiv: 1803.06292 [hep-ph].
- [84] Mark Joseph Oreglia. “A study of the reactions  $\psi' \rightarrow \gamma\gamma\psi$ ”. SLAC Report SLAC-R-236. PhD thesis. Stanford University, 1980. URL: <http://www.slac.stanford.edu/pubs/slacreports/%20slac-r-236.html>.
- [85] Alexander L. Read. “Linear interpolation of histograms”. In: *Nucl. Instrum. Meth. A* 425 (1999), p. 357. DOI: 10.1016/S0168-9002(98)01347-3.
- [86] CMS Collaboration. *CMS luminosity measurements for the 2016 data-taking period*. CMS Physics Analysis Summary CMS-PAS-LUM-17-001. 2017. URL: <http://cds.cern.ch/record/2257069>.
- [87] M. Aaboud et al. “Measurement of the Inelastic Proton-Proton Cross Section at  $\sqrt{s} = 13$  TeV with the ATLAS Detector at the LHC”. In: *Phys. Rev. Lett.* 117 (2016), p. 182002. DOI: 10.1103/PhysRevLett.117.182002. arXiv: 1606.02625 [hep-ex].
- [88] CMS Collaboration. *Electron and photon performance in CMS with the full 2016 data sample*. CMS Detector Performance Summary CMS-DP-2017-004. 2017. URL: <https://cds.cern.ch/record/2255497>.

- [89] Vardan Khachatryan et al. “Performance of Photon Reconstruction and Identification with the CMS Detector in Proton-Proton Collisions at  $\sqrt{s} = 8 \text{ TeV}$ ”. In: *JINST* 10 (2015), P08010. DOI: 10.1088/1748-0221/10/08/P08010. arXiv: 1502.02702 [physics.ins-det].
- [90] Jon Butterworth et al. “PDF4LHC recommendations for LHC Run II”. In: *J. Phys. G* 43 (2016), p. 023001. DOI: 10.1088/0954-3899/43/2/023001. arXiv: 1510.03865 [hep-ph].
- [91] ATLAS and CMS Collaborations, LHC Higgs Combination Group. *Procedure for the LHC Higgs boson search combination in Summer 2011*. Tech. rep. ATL-PHYS-PUB-2011-11, CMS NOTE 2011/005. 2011. URL: <http://cdsweb.cern.ch/record/1379837>.
- [92] Thomas Junk. “Confidence level computation for combining searches with small statistics”. In: *Nucl. Instrum. Meth. A* 434 (1999), p. 435. DOI: 10.1016/S0168-9002(99)00498-2. arXiv: hep-ex/9902006 [hep-ex].
- [93] A L Read. “Presentation of search results: the  $CL_s$  technique”. In: *J. Phys. G* 28 (2002), p. 2693. DOI: 10.1088/0954-3899/28/10/313.
- [94] Glen Cowan et al. “Asymptotic formulae for likelihood-based tests of new physics”. In: *Eur. Phys. J. C* 71 (2011). [Erratum: doi:10.1140/epjc/s10052-013-2501-z], p. 1554. DOI: 10.1140/epjc/s10052-011-1554-0. arXiv: 1007.1727 [physics.data-an].
- [95] Eilam Gross and Ofer Vitells. “Trial factors for the look elsewhere effect in high energy physics”. In: *Eur. Phys. J. C* 70 (2010), pp. 525–530. DOI: 10.1140/epjc/s10052-010-1470-8. arXiv: 1005.1891 [physics.data-an].

- [96] C. Patrignani et al. “Review of Particle Physics”. In: *Chin. Phys. C* 40 (2016), p. 100001. DOI: 10.1088/1674-1137/40/10/100001.

## 초록

거대강입자가속기에서  $Z\gamma$  공명과 들뜬 전자와 뮤온들이  $ll\gamma$  최종 상태로 생성되는 현상을 각각 탐색했다. 두 탐색에 쓰인 데이터는 질량 중심 에너지 13 TeV 에서의 양성자-양성자 충돌 데이터로써 2016년 CMS 검출기를 통해 수집한  $35.9 \text{ fb}^{-1}$ 에 해당한다. 관측 결과는 두 탐색에서 모두 표준 모형 예측과 잘 일치하였다. 좁은  $Z\gamma$  공명 가설과 넓은 공명 가설 아래 생산단면적과  $Z\gamma$  로 붕괴하는 갈레비의 곱에 대한 상한을 공명 질량 0.35와 4.0 TeV 사이에서 설정하였다. 들뜬 전자와 들뜬 뮤온의 경우 질량이 복합 규모와 같다는 가정 아래 각각 질량 3.9와 3.8 TeV 미만이 배제되었다. 복합 규모에 대한 최선의 관측 하한은 들뜬 전자와 뮤온의 질량이 대략 1.0 TeV 인 경우에 25 TeV 로 주어졌다.

**주요어:** 서울대학교, 고에너지물리학, 졸업논문

**학번:** 2014-21353